Developing a Thermometallurgical Model and Furnace Optimization for Austenitization of Al-Si Coated 22MnB5 Steel in a Roller Hearth Furnace

by

Mohit Verma

A thesis
Presented to the University of Waterloo
In fulfillment of the
Thesis requirement for the degree of
Master of Applied Science
In
Mechanical and Mechatronics Engineering

Waterloo, Ontario, Canada, 2019

Author's Declaration

I hereby declare that I am the sole author of this thesis. This is a true copy of the thesis, including any required final revisions, as accepted by my examiners.

I understand that my thesis may be made electronically available to the public.

Abstract

Lightweighting of vehicles while preserving crash-worthiness, in order to satisfy stringent restrictions imposed by the government on the automotive industry, has become a sought after solution which can be realized via hot-forming die quenching (HFDQ). HFDQ is a process where boron-manganese steel blanks, a grade of ultra-high strength steels with a thin eutectic Al-Si coating, are heated beyond T_{Ac3} to achieve a fully austenitic microstructure, a precursor for martensite. Heat treatment is performed using 30 to 40 meter long roller hearth furnaces, comprised of multiple heating zones, with two key objectives: (1) ensure complete austenitization of blanks and (2) transformation of the Al-Si coating into a protective Al-Si-Fe intermetallic coating. Blank heating rates are controlled by the roller speed and zone set-point temperatures, which are currently set by trial-and-error procedures. Therefore, a thorough understanding of the furnace parameters and the industrial objectives are essential. Patched blanks, with spatially varying thickness, leads to inhomogenous heating, making this relationship elusive.

Previous furnace-based energy models only focused on simulating the sensible energy of the load with no explicit information about the latent energy associated with austenitization. Consequentially, the latent term had been incorporated into the sensible energy term thereby defining an effective specific heat. In order to realize how blank heating rate influences microstructural and Al-Si layer evolution, a model coupling heating and austenite kinetics is necessary. This integrated model serves as means for optimizing the heating process.

In this work a thermometallurgical model is developed, combining a heat transfer submodel with two austenite kinetic submodels, an empirical first-order kinetics model and a constitutive kinetics model, via the latent heat of austenitization. The models simultaneously predict the heating and austenitization curves, for unpatched/patched blanks heated within a roller hearth furnace. Validation studies showed that the first-order kinetics model reliably estimated heating and transformation kinetics compared to the constitutive model.

The validated models are then used to optimize the zone set-point temperatures, roller speed, and cycle length for a 12-zone roller hearth furnace whilst minimizing the cycle time in a deterministic setting. A gradient-based interior point method and hybrid scheme were used to assess the constrained multivariate minimization problem with two alternative austenitization constraints imposed: a soak-time based and explicitly modeled requirement. In both cases, the most savings in cycle time were achieved using the explicitly modeled phase fraction austenite constraint, with reductions of approximately 2 to 3 times from the nominal settings.

Acknowledgements

I would like to begin by thanking my supervisor Professor Kyle James Daun, for entrusting me with such an impactful project. I know that the beginning was rough and tough, in particular the learning curve I had to exceed over a short period of time, but you never gave up on me and looked passed my possibly unintelligible questions to help me become a significantly smarter and ethical engineer. Your enthusiasm for constantly learning, applying concepts and of course radiation heat transfer definitely rubbed off on me! I was able to learn the importance of being humble, hardworking, the game changing aspect research has on practical problems, and of course how vital our decisions are. I look forward to applying these skills, and be as exceptional as you are. One thing I would like to say is that I was very fortunate and blessed to have you as my MASc. supervisor! I hope that I was able to exceed your expectations.

Thank you to Professor Richard Culham, my co-supervisor, for reviewing my conference and journal papers, as well as my thesis. Your constructive comments greatly assisted me with preparation of this thesis.

I would also like to thank Mr. Cyrus Yao at Promatek Research Center, Mr. Parthkumar Patel and Mr. Adam Matos, at Formet Industries, for their technical support and allowing us to perform validation studies with their roller hearth furnace.

I would like to extend a warm gratitude to Mr. Richard Gordon for allowing me to work in his lab space for my experiments, use of the muffle furnace, and providing the necessary PPE; Mr. Eckhard Budziarek and Mr. Yuquan Ding for useful advice; Mr. Neil Griffett for assisting with programing and troubleshooting DAQ issues; and last but not the least the E3 machine shop technicians, in particular, Mr. Rob Kaptein and Mr. Jorge Cruz for their patience and assistance with cutting and welding.

A sincere thank you to all of my fellow lab mates and colleagues for not only providing assistance and creative problem solving techniques, but also for making the two years of my MASc. degree ones I can never forget! To name just a few: Sina Talebi Moghaddam, Natalie Field, Stephen

Robinson-Enebeli, Samuel Grauer, Timothy Sipkens, Nigel Singh, Paul Hadwin, Roger Tsang, Rodrigo Miguel, Cory Yan, Ned Zhou, Matthew Ho, Nick Ho, Kaishsiang Lin, Massimo Di Ciano, and Mark Whitney. A few words:

Sina – You are an amazingly talented researcher and the group's radiation heat transfer specialist. Your work ethics, ability to think on the spot, programming skills, and timely assistance was amazing to experience. Thank you for all the laughter and support you provided! As the group's senior PhD, a lot of the wisdom will surely come from you and I know you will do a phenomenal job!

Stephen – Man …you just started your academic career this term (F'18) but it seems like you have been here as long as me. Thanks for the encouraging words, late night thrills (the firecracker and bubble tea incidents), and introduction to the world of fitness "coach". It is always fun talking with you and seeing your enthusiasm when it comes to conversing with people (known and unknown) as well as when you order food! Can't thank you enough for putting up with me and listening to my problems hours on end…I'll miss ya bud! I know you will do a phenomenal job and remember, "Don't mess up!"

Tim and Sam – Thanks for being patient with me and taking the time to make sure that I understood what you were trying to teach me. The both of you are truly brilliant researchers that will make huge contributions and new set standards in your respective fields, as you already have. I feel that there are not enough words to describe your amazing qualities and until this day, I cannot say how thankful I am to have met you two.

Nigel – We did not work together, but the laughter you brought with your funny near death stories, whenever you dropped by the lab, always lightened the mood!

Paul – First and for most, congratulations on the birth of your daughter! You are a statistical, optimization, and Bayesian wizard. Thank you for giving me the chance to TA for your course, enduring my numerous questions, asking me how things are going, and helping me when I looked like I was stuck.

Roger – The academic life beckoned for you once again, ha-ha. Who knew it would take a loss in arm wrestling to make me hit the gym and seek redemption, so in that respect, thank you. Thanks for the funny stories, sarcastic remarks, and insightful information about your experiences and life!

Rodrigo – I enjoyed hearing about your experiences in Brazil and how they compare to the life here. You are full of persistence, a sign of a great researcher! Thank you for all of your advice when I got stuck (concept wise and coding). In addition, thanks for always coming to lunch with me, a true friend, when no one else wanted to go. It is impressive to see you being able to balance academics with family life!

Cory – You played a vital role in the success of my work; perhaps without your dedication and assistance I would not be here at this stage writing my thesis. Honestly, we had a lot of funny, very stressful, and "what the hell…" type of moments. The questions you asked were a sign of how passionate you are about research, and always forced me to extend my thinking beyond what I knew in order to try to answer them. It was a pleasure to work with you and see you grow over the course of two terms. I hope that I was able to teach you a few things just as you had taught me, and I wish you the very best with your post graduate studies!

Ned – Thanks for being our (Stephen and my) gym buddy, putting up with our ridiculous jokes, childish behavior in the change room, roasting us, and of course giving valuable advice. I also wanted to say thanks for listening to me, guiding me through certain situations and remining me to stop over analyzing things. You'll do a phenomenal job in the future! Just remember to help others with chemistry homework and do not leave people hanging *cough cough* ;-)

Kaihsiang – For someone who always says he is stressed, you always manage to pump out high quality results! You are a compassionate person who truly enjoys research. I know that you miss your home, but always remember that the group is your second family! You are going to go far in life, proven by the fact that you are doing a phenomenal job on a research topic that is different from your Master's. Trust yourself and make sure to laugh, talk, and have fun in the process!

Massimo – Mass, thank you so much for all your help over the course of my degree, from answering my questions, listening to me rant about debugging and experimental issues, sending me useful papers, providing me access to the thermocouple welder, and showing me how to

prepare samples for microscopy. You are a remarkably funny person with a great sense of humor! Our friendship evolved quickly from acquaintance to great friends, all thanks to the hysterically funny conversations we had (which I will keep on file in case I need to use it against you in the future, ha-ha!!). I also wanted to thank you for clearing time in your busy schedule to meet with me and being strict when it was necessary (definitely helped me grow as an individual and as a professional). Congratulations once again in securing a job, can you hook a brotha up too ;-p

Mark – Thank you for helping me out on numerous occasions when access to the thermocouple welder was required; and sharing your insightful experiences about your work and life! It was always amazing and fun to talk to you (especially the story about relieving sore muscles) I wish you the very best with you endeavors.

To the other friends from Waterloo, you know who you are, the lunches, dinners, and parties will forever stay with me; I will dearly miss your companionship. Special shout out to three of my friends for making the degree worth more than what it is: Henry Ma, Victor Qian, and Natun Dasgupta.

At this time, I would like to thank my parents, Rajnish and Neelam Verma, for trusting my judgement about pursuing a Master's degree, supporting me, and ensuring my best interest. Without your love and trust, I would not have made it where I am today! It was because of your constant saying, "learn, learn, and learn", that I am always hungry to improve my knowledge. I want to thank god for helping me find this research position, with arguably one of the best researchers in heat transfer; allowing me to learn life lessons that I could not have learned anywhere else; for giving me the chance to make strong bonds with so many people; and for giving me the chance to make valuable contributions to industry and the academic world.

Wow…this acknowledgement is turning into a thesis itself, so I will end now. In closure, I wanted to say three things that I felt are crucial lessons I learned from this degree:

(1) "Theory catches up to practice." A saying I did not understand until now.
(2) True understanding comes from making mistakes and not always staying on the safe side.
(3) The source of knowledge is experience.

I would like to dedicate this thesis to my friends,

And most importantly my family,

Rajnish, Neelam, and Gourave Verma

Table of Contents

List of Figures

List of Tables

Nomenclature

The symbols in the document are kept consistent, both internally and with the source literature. Below is a list of symbols used in this thesis, categorized in the context in which they appear.

Critical Temperatures

Symbol	Units	Description
T_{Ae1}	°C	Onset of austenitization under equilibrium
T_{Ae3}	°C	Completion of austenitization under equilibrium
T_{Ac1}	°C	Onset of austenitization under non-isothermal heating conditions
T_{Ac3}	°C	Completion of austenitization under non-isothermal heating conditions
M_s	°C	Initiation of martensite transformation
M_f	°C	Completion of martensite transformation

Heat Transfer Parameters

Symbol	Units	Description
Bi	-	Biot Number
h_{rad}	W/(m^2·K)	Linearized heat transfer coefficient
t_{blank}	m	Blank thickness
G_λ	W/(m^2·µm)	Spectral irradiation
$E_{\lambda b}$	W/(m^2·µm)	Spectral emissive black power

Heat Transfer Submodel

Symbol	Units	Description
ρ_{22MnB5}	kg/m^3	Density of 22MnB5
$c_{p,eff}$	J / (kg·K)	Effective specific heat
V_j	m^3	Volume of region *j*
$dT/d\tau$	°C /s	Heating rate
Q_{rad}	W	Radiation heat transfer rate
Q_{conv}	W	Convection heat transfer rate
Q_{cond}	W	Conduction heat transfer rate
T_∞	K	Air temperature
Nu	-	Nusselt number
L_c	m	Characteristic length
A_s	m^2	Wetted surface area

P	m	Blank perimeter
k_{air}	W/(m·K)	Thermal conductivity of air
T_{film}	K	Film temperature
Ra_{Lc}	-	Rayleigh number
g	m/s^2	Gravitational constant
β	K^{-1}	Volumetric expansion coefficient
α_{air}	m^2/s	Thermal diffusivity of air
ν_{air}	m^2/s	Kinematic viscosity of air
U	$W/(m^2 \cdot K)$	Overall heat transfer coefficient
A_j	m^2	Interfacial area
t_{gap}	m	Air gap thickness
k_{22MnB5}	W/(m·K)	Thermal conductivity of 22MnB5
T_b *or* T_{blank} *or* $T(\tau)$	K	Blank temperature
T_{surr}	K	Surrounding temperature
ε_λ	-	Spectral hemispherical emissivity
ε	-	Total hemispherical emissivity
α_λ	-	Spectral hemispherical absorptivity
α	-	Total spectral hemispherical absorptivity
ρ_λ	-	Spectral hemispherical reflectivity
ρ	-	Total spectral hemispherical reflectivity
σ	$W/(m^2 \cdot K^4)$	Stephen-Boltzmann constant

First-Order (F1) Kinetics Submodel

Symbol	Units	Description
n	-	Avrami constant
w	-	Intermediate variable
A	s^{-1}	Pre-exponential factor
E_A	J/mol	Activation energy
R	J/(mol·K)	Ideal gas law constant
f_γ	-	Austenite phase fraction
μ	-	Mean of MVN distribution
Γ	-	Covariance matrix
H_0	HV	Vickers micro-hardness of as-received sample
H_γ	HV	Vickers micro-hardness of quenched sample
H_{TAc3}	HV	Vickers micro-hardness of sampled heated beyond T_{Ac3}

Phenomenological Kinetics Submodel

Symbol	Units	Description
$\dot{N}$	s^{-1}	Nucleation rate
N	-	Number of nuclei formed

$\dot{T}$	K/s	Heating rate
Q_N	J/mol	Activation energy for nucleation of critical sized nuclei
f_p	-	Fraction of pearlite
$\dot{v}$	m^3/s	Volumetric growth rate
Q_v	J/mol	Activation energy for growth
$\dot{f}_v'$	-	Extended volume fraction austenite
$f_{\gamma s}$	-	Saturated volume fraction austenite
$\dot{f}_\gamma$	-	Rate of austenite formation in a real volume
A_1, A, ϕ_A	-	Internal and external influencing factors
B_1, B, ϕ_B	-	Material constants
C_1, C_2, C_3	-	Model fitting constants
m, n, m_0, n_0, ϕ_N	-	Model constants

Thermometallurgical Model

Symbol	Units	Description
Δh_γ	J/kg	Latent heat of austenitization
c_p	J/(kg·K)	Sensible specific heat
$df_{\gamma,j}/d\tau$	s^{-1}	Rate of austenite formation

Newton's Method

Symbol	Units	Description
p_k	-	Search direction
α_k	-	Search length
$\nabla f(x_k)$	-	Gradient of objective function
$\nabla^2 f(x_k)$	-	Hessian of objective function

Trust-region Method

Symbol	Units	Description
Δ	-	Trust-region sphere radius

Interior Point Method

Symbol	Units	Description
$\phi(x)$	-	Barrier function
μ	-	Weighted barrier parameter

Karush-Kuhn-Tucker (KKT) for Gradient Based Method Convergence

Symbol	Units	Description
$\nabla_x \mathcal{L}(x^*, \xi^*)$	-	Gradient of Lagrange function at optimal
x^*	-	Optimal design parameters
ξ^*	-	Lagrange multiplier at optimum for nonlinear constraints

Optimization Model

Symbol	Units	Description
$F(x)$	Problem specific	Objective function
$F(x^*)$	Problem specific	Optimal objective function
$c_{\mathcal{E}}$	-	Equality constrains
$c_{\mathcal{I}}$	-	Inequality constraints
L_b	m	Batch length
$L_{g,min}$	m	Minimum batch gap length
η_{th}	-	Radiant tube thermal efficiency
$\dot{m}_b$	kg/s	Batch (made of up to four blanks) mass flow rate
$\dot{Q}_{loss,i}$	kW	Heat loss through furnace walls
$\dot{Q}_{burner,i}$	kW	Burner capacity

Chapter One
Introduction to Hot Forming Die Quenching

The hot forming die quenching (HFDQ) process and its industrial relevance are explored. A thorough description of Usibor® 1500AS, the most commonly used ultra-high strength steel (UHSS) in HFDQ, is provided. The focus of the HFDQ process is upon the heating stage, realized with roller hearth furnaces, with the objective of fully austenitizing UHSS blanks and transforming the as-received Al-Si coating into an Al-Si-Fe intermetallic layer with desired properties. Issues with current industrial practice have been identified, followed by a detailed review of past furnace based models (heat transfer and austenitization kinetics). The chapter concludes by stating the research objectives and an outline of the thesis structure.

1.1 Hot Forming Die Quenching

HFDQ or "hot stamping" was initially developed by Plannja, a Swedish company specializing in saw blade fabrication (1977). Due to increased demand to satisfy fuel economy and emission regulations, HFDQ was adopted by the automotive industry to make automotive parts (including door beams, A- and B-pillars, front and rear bumpers, and side impact beams, *cf*. **Figure 1**.) from ultra-high strength steels, [1], in order to obtain lighter, and thus more fuel efficient cars without sacrificing crash-performance [2, 3]. UHSS components can realize up to 50% weight savings compared to high strength low alloy (HSLA) steels [4], and each 10% reduction in weight results in an approximately 2-8% improvement in vehicle fuel consumption [5]. Previously, light-weighting was mainly done using HSLA steels and aluminum, however, due to their cost, lack of strength, and limited formability [6, 7] boron-manganese steels have come to prominence in automotive manufacturing.

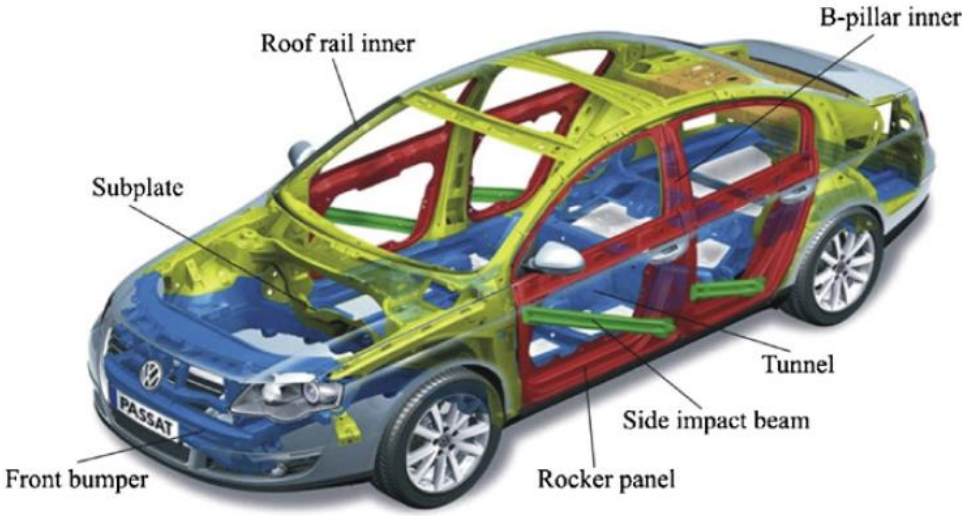

Figure 1: Structural components manufactured using UHSS blanks in hot forming die quenching, for automotive applications [1].

The hot stamping processes can be classified as either direct or indirect, as shown in **Figure 2**. The direct HFDQ process is comprised of three stages: (1) heating of UHSS steel to transform the as-received ferrite-pearlite microstructure into austenite; (2) transfer of heated steel to water-cooled tool/die; and (3) forming and quenching of the steel to produce fully martensitic as-formed part.

The heating stage of HFDQ, is traditionally performed using a continuous roller hearth furnace [8]. The purpose of heating in HFDQ is two-fold; first to convert the as-received ferrite/pearlite microstructure to austenite; and, second, to transform the Al-Si layer into an intermetallic Al-Si-Fe layer. The heating process is non-isothermal [9] where UHSS blanks are thermally soaked at 900°C [1], thus transforming the as-received microstructure consisting of ferrite grains and pearlite bands [10] into austenite (a single phase solid solution of carbon stable at high temperature [11]), as shown in **Figure 3**. Austenitization is the precursor to martensite and makes the steel ductile allowing for forming of complex geometries with minimized forming forces and reduced wear stress between the steel and forming tool [3, 12]. During heating the Al-Si coating reacts with iron from the substrate steel to form a permanent Al-Si-Fe intermetallic layer that prevents decarburization and provides long-term environmental corrosion protection in the final formed automotive component [13, 14, 15].

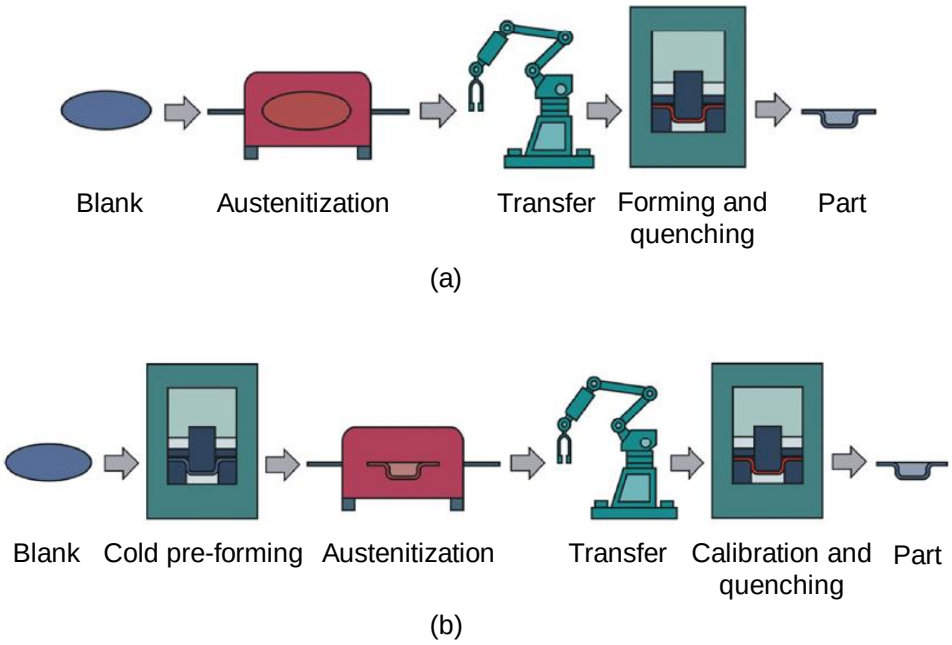

Figure 2: Two variants of hot stamping process employed in industrial practice: (a) direct hot stamping and (b) indirect hot stamping [1].

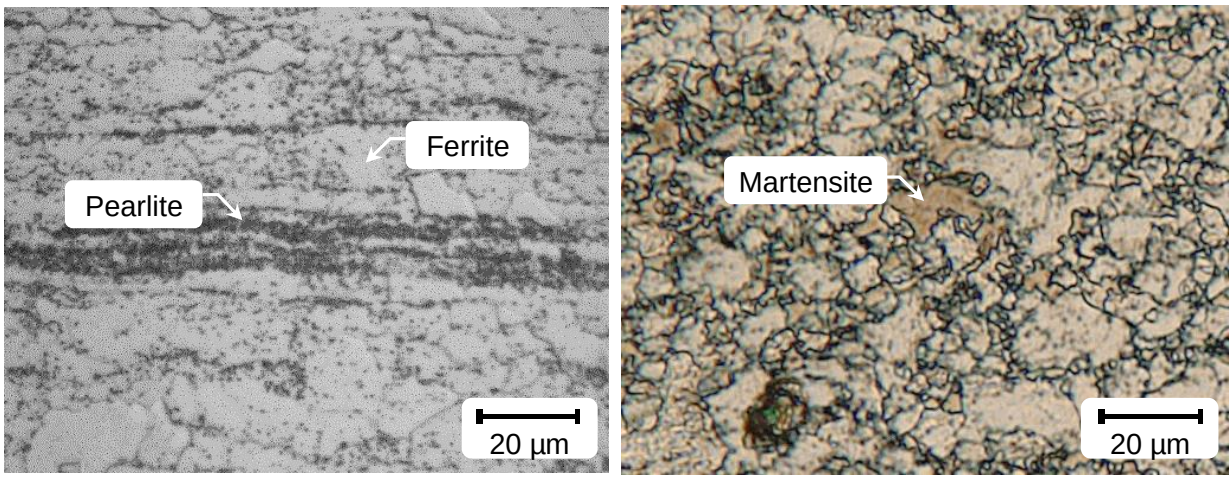

Figure 3: Optical microscopy of the as-received and heated microstructure of Al-Si coated 22MnB5. (a) As-received steel composed of ferrite grains and pearlite bands. Ferrite grains appear bright and pearlite bands appear dark (due to presence of carbon). (b) Micrograph of the steel heated to 900°C, yielding complete austenitization, which is assumed to its entirety to be martensite upon quenching [10].

Upon exiting the furnace, the blanks are immediately moved to cooling dies, via an automated transfer system. Since the exiting blanks are very hot (~950°C), they cool rapidly through radiative exchange and natural convection with the colder surroundings. To prevent unwanted formation of bainite or ferrite in the final microstructure after forming/quenching, transfer must be completed well before the blank temperature falls below T_{Ac3} = 880°C [9, 10].

Forming and quenching are simultaneously achieved using a single-stroke water-cooled tool/die. Prior to quenching, the heated blanks must be formed, as it is most ductile and capable of yielding part geometries of varying complexity [1]. The quenching process converts austenite into martensite, via a diffusionless (or "flash-freeze") transformation [16], achieved using feasible cooling rates [17] between 25-30°C/s [9]. The goal of this procedure is usually to achieve homogeneous mechanical properties in the formed part through uniform cooling, although distributed tailored properties may be desirable for certain applications [18]. Caron et al. [19] explained that the non-uniform die surface temperatures and contact pressure affect the extent of cooling experienced by the blank. Forming/quenching tools are designed with internal cooling channels, to maintain uniform die surface temperatures needed to ensure adequate quenching rates [1].

Indirect hot stamping has one additional step upstream, prior to the austenitization stage, called cold pre-forming, in which blanks are formed into their approximate shapes. This additional step aids in the forming/quenching process as pressing forces and tool wear are minimized. In practice, however, direct hot stamping lines are more often employed due to the cost savings associated with the elimination of the cold pre-forming step. This work focuses on the direct HFDQ process.

Naderi [4] had shown that boron steel grades are the only type of alloys that form a fully martensitic microstructure upon quenching. The hardenability of such steels is greatly influenced by the addition of boron (*eg*. 10 – 50 ppm) [12], which delays austenite decomposition to bainite and ferrite. This consequently reduces the feasible cooling rates required to achieve martensite (*i.e*. shifting the "nose" of the TTT diagram to the right) [12, 17], thus making boron steels desirable for HFDQ operations.

1.1.1 Usibor® 1500AS

Usibor® 1500AS is the most widespread UHSS used for HFDQ, due to its versatility, enhanced formability, and high strength upon quenching. The base steel, 22MnB5, is a hypoeutectoid steel, with approximately 0.23 wt%-C [10], including trace elements of boron, titanium, and manganese which improve strength characteristics [1]. Naderi [4] explains that the segregation of boron throughout the austenite grain boundaries delays the nucleation of ferrite during quenching, enabling formation of martensite easily, whereas titanium slows grain growth, thus enabling finer grain structures to form and improve toughness [4]. The average chemical composition of the steel, as experimentally determined by Di Ciano et al. [10], is summarized in **Table 1**.

Table 1: Composition (wt. %) of constituents composing 22MnB5

C	Mn	Si	Cr	Al	Ti	Ni	P	Cu	B	Mo	Fe
0.23	1.17	0.25	0.20	0.04	0.034	0.02	0.015	0.01	0.002	< 0.01	Bal.

The microstructure of the as-received steel, shown in **Figure 3**, consists of approximately 80%-ferrite / 20%-pearlite. Austenite nucleation initiates within the ferrite/pearlite grain structure upon reaching the onset critical temperature, $T_{Ac1} \cong 730°C$, and completes at $T_{Ac3} \cong 880°C$ [9, 10, 20]. The transformation process, however, is not instantaneous and requires time to achieve the desired austenite phase fraction. Consequently, blanks quickly heated to T_{Ac3} (*e.g.* through direct contact heating [11]) require longer soaking periods in order to convert the ferrite entirely into austenite [21]. In industrial roller hearth furnaces, the heating rate is sufficiently low ($\leq 13°C/s$) so that blanks are mostly austenitized upon reaching T_{Ac3} without requiring additional thermal soaking, as observed by Verma et al. [22] and Jhajj et al. [23].

Figure 4 shows the continuous cooling curve (CCT) diagram for 22MnB5. The minimum cooling rate required to transform austenite to martensite can be approximated using the CCT diagram. The transformation from austenite to martensite begins and completes at 410°C and 280°C, respectively, with a required minimum cooling rate of 25°C/s [1, 24, 25], summarized in

Table 2. Literature reports that the approximate hardness of 22MnB5 steel after quenching is 480-500 HV [18, 26].

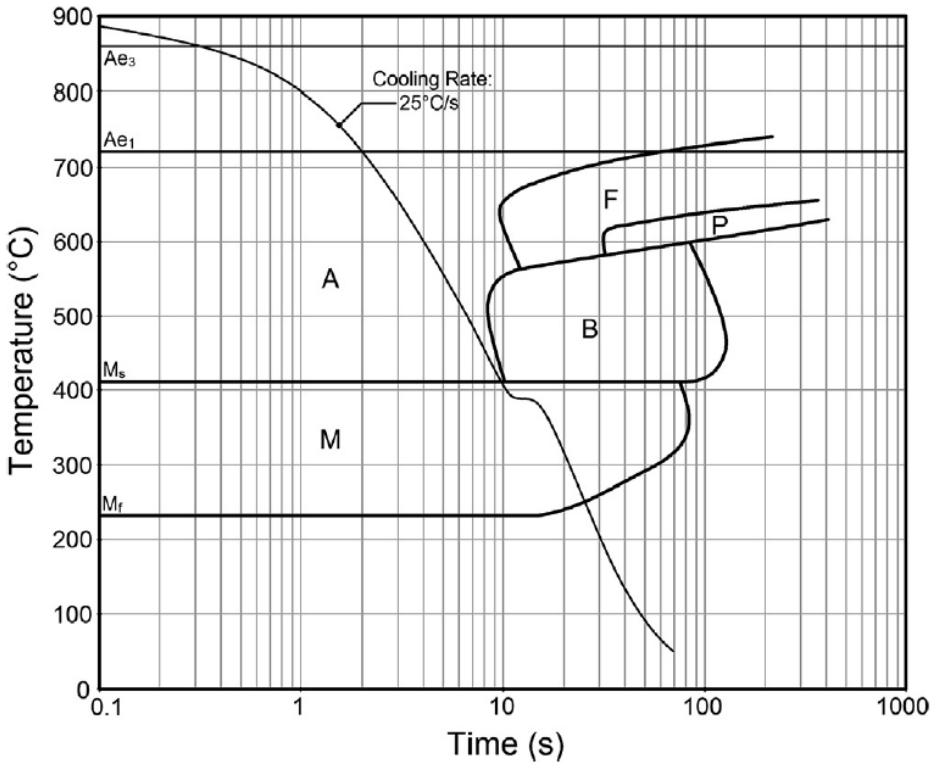

Figure 4: Continuous cooling curve diagram of 22MnB5 steel [4].

Table 2: Critical transformation temperatures and mechanical properties of 22MnB5 [1]

T_{Ac1}	T_{Ac3}	M_s	M_f	$T_{critical\ cool,\ min}$	Yield Strength [MPa]		Tensile Strength [MPa]	
[°C]	[°C]	[°C]	[°C]	[°C/s]	As-received	Hot Stamped	As-received	Hot Stamped
730	880	410	280	25	457	1010	608	1478

1.1.2 Heat Treatment

The heating stage of HFDQ is crucial in order to obtain fully austenitic parts, the precursor for fully martensitic components, and desired transformation of the intermetallic coating. In order to effectively model steel heating, understanding of the heating technology, metallurgical kinetics, and diffusional kinetics is vital.

Indirect-fired continuous roller hearth furnaces have been the mainstay heating technology utilized in HFDQ to heat treat blanks [8], as shown in **Figure 5**. While alternative heating methods such as batch furnaces [27], direct contact heating [28], and induction heating [1], have been proposed, industrial implementation of these techniques is limited [28].

Roller hearth furnaces are on average 30-40 m long [1] and heated by natural-gas fired radiant tubes, separating the blanks from the products of combustion, which are corrosive and can cause hydrogen embrittlement. In general, the length of the furnace is a function of the mill productivity, part geometry, heating time, and downstream buffer times [1, 29]; longer furnaces permit a shorter cycle time. Roller hearth furnaces are constructed with several independent heating zones, each with an individually controlled set-point temperature, ranging from 800-950°C [23]. Ceramic rollers convey the batches, each comprised of at most four work pieces, through different zones heated via radiation from the surroundings, convection from the enclosed atmo sphere, and conduction from the rollers. Variations in the part geometry and thermal mass influence the heat treatment, thus specific heating rates must be defined for each blank to achieve complete austenitization and avoid excess coating growth [22, 23, 30]. Blank heating curves are used as guidelines in industry to define necessary heating conditions [1].

Figure 5: Continuous roller hearth furnace, located at Formet Industries, St. Thomas, ON. The furnace is used for austenitizing blanks and transforming the as-received eutectic coating to an intermetallic Al-Si-Fe layer during heating.

There are two distinct heat treatments that may be performed in HFDQ: isothermal and non-isothermal annealing, which are shown schematically in **Figure 6**. Isothermal annealing, also known as intercritical annealing, refers to thermally-soaking blanks at a temperature between T_{Ae1} and T_{Ae3} [24, 25, 31, 32]. The onset temperature of the eutectoid reaction, T_{Ae1}, (*i.e.* ferrite/pearlite $\rightarrow$ ferrite/austenite or $(\alpha+\theta) \rightarrow (\alpha+\gamma)$), is 723°C. Under equilibrium conditions, ferrite (α) is fully transformed into austenite (γ) at the completion temperature, T_{Ae3}. This temperature is defined relative to the completion temperature of pure iron, 910°C [25], which decreases with increasing carbon content, causing the transition from $\alpha \rightarrow \gamma$ to occur at lower temperatures [33, 34]. Soaking blanks at an intermediate temperature between T_{Ac1} and T_{Ac3} results in partial austenitization, with a final microstructure that is an equilibrium mixture of austenite and ferrite ($\alpha+\gamma$) [24, 25]. Non-isothermal annealing, which is also called continuous heating, involves heating blanks above T_{Ac3} to obtain an entirely austenitic (γ) in the microstructure [10, 20, 24, 25]. In practice, blank heating

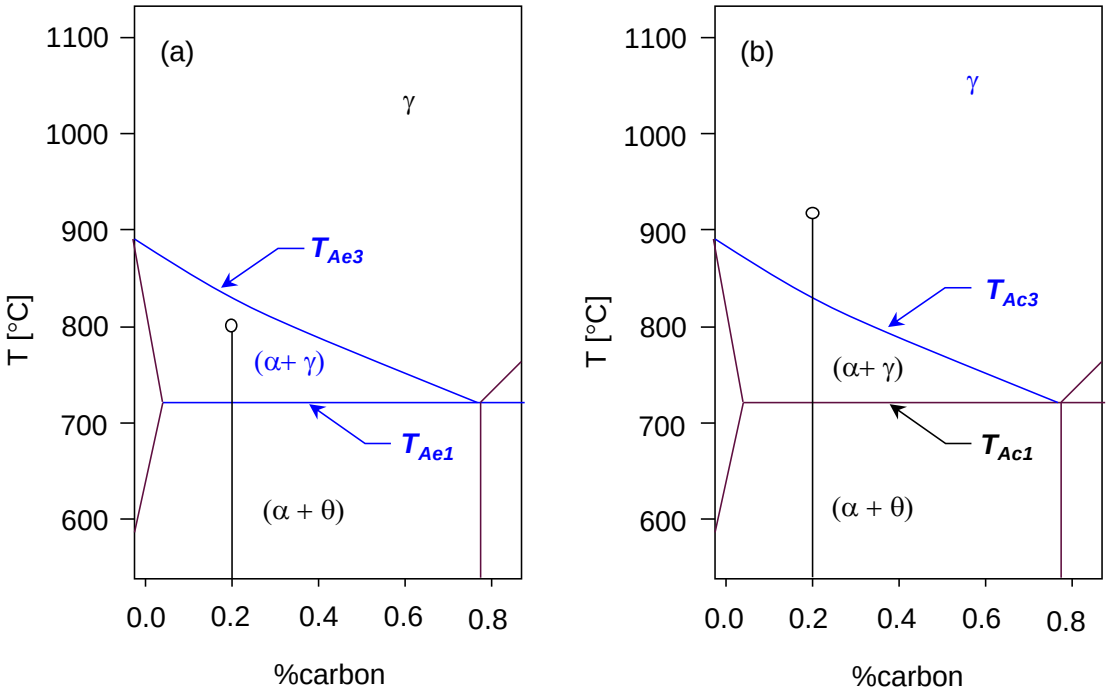

Figure 6: The Fe-C phase diagram for eutectoid steels. (a) Isothermal annealing; the initial ferrite/pearlite structure transforms to an equilibrium mixture of ferrite/austenite. (b) Non-isothermal annealing; the initial microstructure completely transforms to austenite as the temperature exceeds T_{Ac3}. The heating regime for each annealing method and associated equilibrium phase has been highlighted in blue.

in the roller hearth furnace is a continuous heating process followed by isothermal soaking [1, 24, 25].

The phase transformation of 22MnB5 from ferrite/pearlite (α+θ) to austenite (γ) can be identified using the hypoeutectoid portion of the Fe-C equilibrium phase diagram, shown in **Figure 7**. Austenite kinetics is a nucleation and growth process [35, 36], which was later confirmed by Roberts and Mehl [37], as cited by Huang et al. [36]. Huang et al. [36] stated that cementite (Fe_3C) precipitates dictate nucleation sites; thus, potential nucleation sites are ferrite/pearlite interfaces and ferrite grain boundaries with cementite particles. Under equilibrium conditions, once the steel has reached $T_{Ae1}\cong723°C$, austenite nucleation occurs both in the proeutectoid ferrite (α) and within pearlite colonies (α′+Fe_3C), composed of eutectoid ferrite (α′) and cementite (Fe_3C) arranged in a lamellae structure. Although austenite nuclei form in both phases, pearlite transforms into austenite more quickly due to its greater carbon content. Roosz et al. [38] and Caballero et al. [39] found that austenite nucleation primarily occurs at the interfaces of the eutectoid ferrite/cementite within the colony. Speich et al. [40] explained that austenite growth within the pearlite colonies is carbon diffusion dependent, however at lower temperatures this switches to manganese diffusion. Since

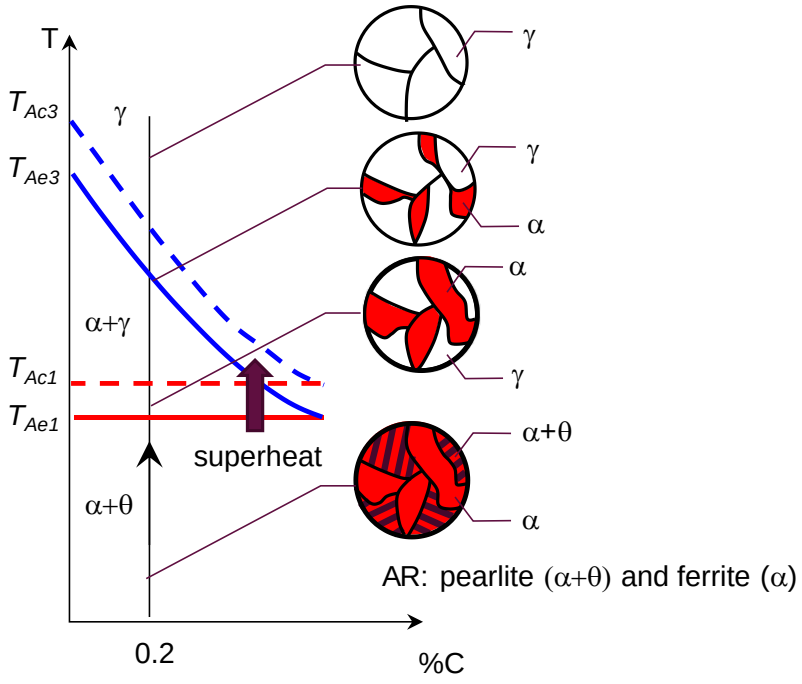

Figure 7: Phase diagram of a hypoeutectoid steel illustrating the microstructural evolution during heating. Adapted from Callister et al. [41].

heat treatments are performed at temperatures greater than T_{Ae1}, austenite kinetics is primarily controlled by carbon diffusion; the diffusivity of carbon (an interstitial atom) is orders-of-magnitude faster compared to manganese (a substitutional atom) [42]. The phase change from pearlite to austenite ($\theta \rightarrow \gamma$) is rapid due to short diffusion distances between adjacent cementite lamellae [31, 43]. Once the pearlite has completely transformed, the microstructure consists of proeutectoid ferrite (α) and austenite (γ).

Upon further heating, Roosz et al. [38] and Speich et al. [40] had observed that the transformation proceeded with the proeutecoid ferrite phase. Datta and Gokhale [44] and Speich et al. [31] determined that during this stage of transformation there was no further nucleation and the process continued only by growth of pre-existing austenite particles. Since the proeutectoid ferrite lacks carbon, additional carbon atoms diffuse from the austenite/cementite boundary within the pre-existing austenite and ferrite/cementite boundary from the ferrite to promote growth of the γ/α interface [25, 38]. Concerning intercritical annealing, the phase transformation of $\alpha \rightarrow \gamma$ continues until the average carbon content of austenite equals that within the steel, thus an equilibrium mixture of ferrite/austenite ($\alpha+\gamma$) is expected. Heating the steel beyond T_{Ae3} completely transforms the ferrite into austenite. Under non-isothermal annealing conditions the austenite onset and completion temperatures are shifted from their equilibrium values (T_{Ae1} and T_{Ae3}) to slightly higher temperatures (T_{Ac1} and T_{Ac3}), which depend on the heating rate [45]. For heating rates between 1-5°C/s, Di Ciano et al. [10] found T_{Ac1} and T_{Ac3} to lie between 723-740°C, and 850-855°C, which is broadly consistent with values obtained from empirical correlations and experimental studies found in literature [43, 46].

The amount of austenite formed during heating is influenced by temperature; soak time; and heating rate. Previous studies on steels with comparable carbon content to 22MnB5 have shown that the phase fraction of austenite increases with temperature and soaking time due to greater carbon diffusion [24, 25, 36, 45, 46]. However, as reported by Li et al. [25] and Asadi Asadabad et al. [46] austenitization proceeds with higher soak times until constrained equilibrium of carbon diffusion. Austenitization studies in which steels are heated to a particular temperature at different heating rates have shown that the fraction of austenite formed at the end of the continuous heating stage, termed incipient austenite, decreases with higher heating rates [24, 25,

36, 47]. This phenomenon is due to the limited time available for carbon diffusion [24, 25]; thus to achieve equilibrium phase fraction of austenite longer soak times are required compared to lower heating rates. In contrast, when parts were heated to different intermediate temperatures with higher heating rates the incipient fraction austenite was always higher. Li et al. [24, 25] explained that higher heating rates promoted greater nuclei formation over a shorter soak period, thus increasing overall growth rate and austenitization within the steel. **Figure 8**, displays the dependence of austenitization on these parameters.

The Al-Si coating also undergoes microstructural and phase changes during blank heating. In the as-received state, the coating consists of an Al-Si matrix and Al_7Fe_2Si and Al_5Fe_2 intermetallic phases at the steel/coating interface [14, 30, 48], as shown in **Figure 9**. The melting temperature of the coating is approximately 575°C, depending on the exact Al-Si composition and heating rate [49]. The molten coating then reacts with iron that diffuses from the substrate steel to form a range of intermetallic compounds (*e.g.* Al_3Fe and Al_5Fe_2). With further heating, the coating becomes progressively thicker. Ideally, the coating should be no more than 40μm thick to preserve weldability [49] and an α-Fe diffusion layer that is at least 20 μm for durability [30]. The diffusion layer forms at the coating/steel interface at 900°C as the aluminum and silicon diffuse into the steel to stabilize the BCC iron lattice [30]. Previous studies [14, 30, 48, 49] performed on the Al-Si coating have observed sensitivity to temperature, soak time, and heating rates.

Liang et al. [48] have shown that heating of the coating below 500°C (*i.e.* below the eutectic temperature) resulted in no change due to significantly limited interdiffusion of Fe from the substrate and Al atoms from the coating. However, heating beyond the eutectic temperature resulted in rapid phase change due to exponential relationship between the diffusion coefficient and absolute temperature (*i.e.* $D = D_o exp(-Q/RT)$) [48]. Upon reaching 930°C, the coating fully transformed into the Al-Si-Fe intermetallic layer. Liang et al. [48] characterized the ternary intermetallic to be composed of varying fractions Al_7Fe_2Si, Al_2Fel and Al_3Fe from the surface of the coating to the steel. Consistently observed phenomena within the coating, at higher temperatures, are the presence of micro-cracks and Kirkendall voids, as shown in **Figure 10**. These features occur due to varying thermal expansion between phases and a disparity between the diffusion coefficient of Fe and Al atoms, respectively [48].

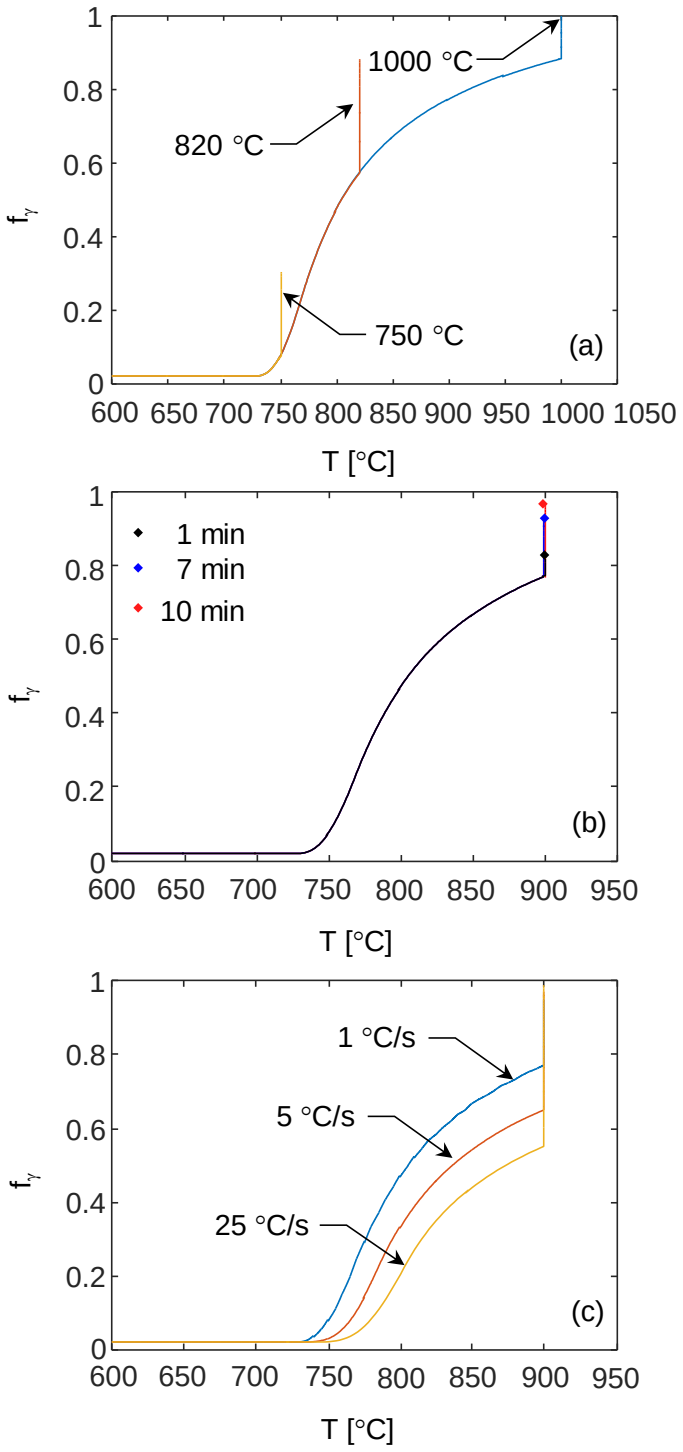

Figure 8: (a) With increasing temperature, the phase fraction of austenite increases. (b) With increasing soaking time, austenite increases until constrained equilibrium of carbon diffusion. Diamonds indicate the equilibrium fraction of austenite formed. (c) Heating to 900°C with various heating rates. With increasing heating rates, incipient austenite decreases. Adopted from Li et al. [25].

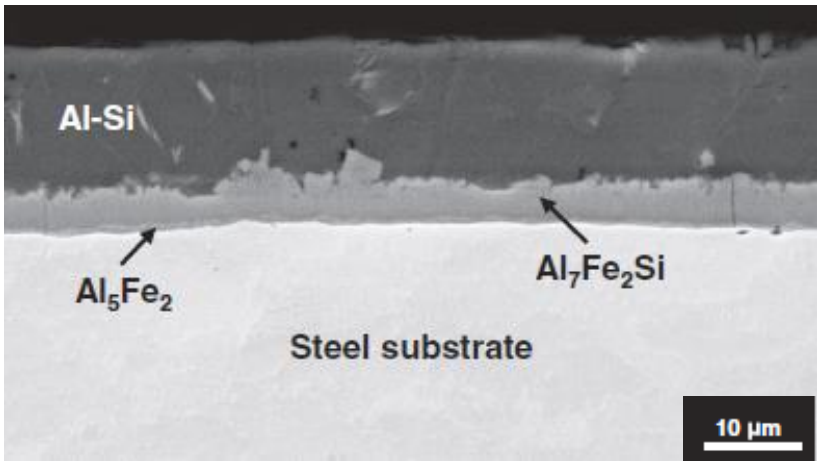

Figure 9: Cross-section of Usibor®1500AS steel with the Al-Si coating. As observed, the as-received coating is mainly made of an Al-Si matrix and thin layer of intermetallic phases at the steel/coating interface [30].

Shi et al. [30] and Liang et al. [48] studied the influence of dwell time on the coating. Shi et al. [30] performed a two-stage study where Al-Si coated samples of 22MnB5 were heated to 610°C for 5 minutes, to yield the Al-Si-Fe layer, followed by immediate heating to 900°C for various soaking periods from 0-30 minutes. They [30] observed that during the initial dwell periods at 610°C, an Al_7Fe_2Si phase forms, which subsequently transforms into Al_5Fe_2, containing precipitates of $(Al, Si)_5Fe_2$. Increasing soak time (2 to 30 minutes at 900°C), results in the formation of an α-Fe layer and transformation of the Al_5Fe_2 and $(Al, Si)_5Fe_3$ into AlFe. In addition to the formation of these phases, an increase in the number of cracks, Kirkendall voids, and coating porosity was reported [30, 48]. Liang et al. [48] recommended that a dwell time of three minutes was ideal to compensate for tradeoff between production efficiency and coating properties.

Heating influences the final coating thickness, which, as mentioned by Grauer et al. [49] should be at most 40 µm thick to maintain weldability and paintability. Kolleck et al. [50, 51], cited by Grauer et al. [49], recommend that heating rates beyond 12°C/s should not be exceeded to avoid melting the coating. This has been shown to be a misinterpretation of the original patent [49]. On the contrary, this specified heating rate is to prevent excessive coating growth as discussed by Grauer et al. [49]. Grauer et al. [49] and Viet et al. [52], as provided by Liang et al. [48], proved melting is inevitable, even with low heating rates (*i.e.* 0.08°C/s). Grauer et al. [49] have shown

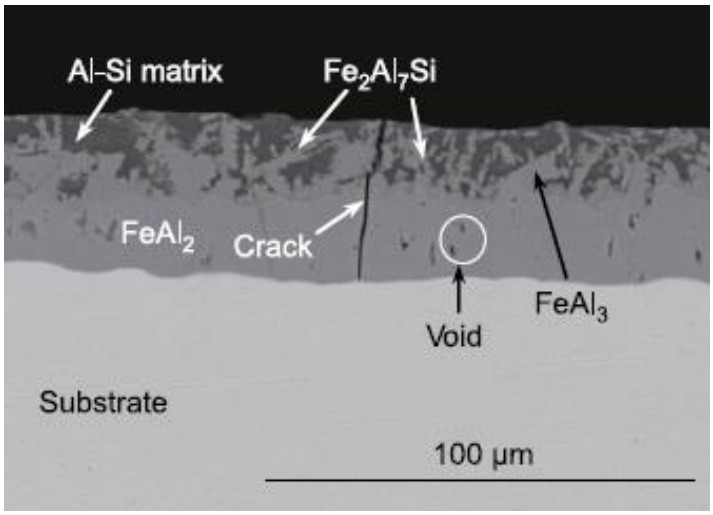

Figure 10: Cross-section of the Al-Si coating heated to 930°C. At high temperatures, micro-cracks and Kirkendall voids develop [48].

that the melting temperature exceeds 575°C with increasing heating rate, thus reducing the final coating thickness due to lack of interdiffusion time between the Fe and Al atoms.

1.2 Research Motivation

Cosma International, a leading Tier-1 automotive parts supplier to OEMs, use roller heath furnaces to heat treat blanks for the production of automotive structural components. Cosma's objective is to optimize their process through judicious selection of the furnace parameters: zone temperatures, blank layout (in terms of spacing between batches on the rollers), and roller speed, so as to minimizing energy consumption and maximize productivity while ensuring batch austenitization and adequate Al-Si-Fe coating growth. This procedure is complicated by the fact that each batch may contain blanks of varying thickness and geometry and each blank may require certain heating rates durations to avoid incomplete austenitization and excessive coating growth. This procedure becomes more complex when additional steel "patches" are spot-welded at critical locations on the blanks to locally reinforce the as-formed component strength, as shown in **Figure 11**. The spatially-varying blank thickness causes inhomogeneous heating that may result in nonuniform and substandard as-formed thus compromising final mechanical and coating properties. This issue may be partially addressed by increasing the heating duration, but at the cost of lower productivity.

Overheating the blanks can also lead to excessive Al-Si-Fe layer growth, and in extreme cases, may cause the coating to ablate [22].

In practice, operators adjust these furnace parameters by trial-and-error with limited guidance from basic heat transfer models. This approach is not only costly and time consuming, but consequently results in suboptimal parameter selection [53], since trial-and-error is halted once

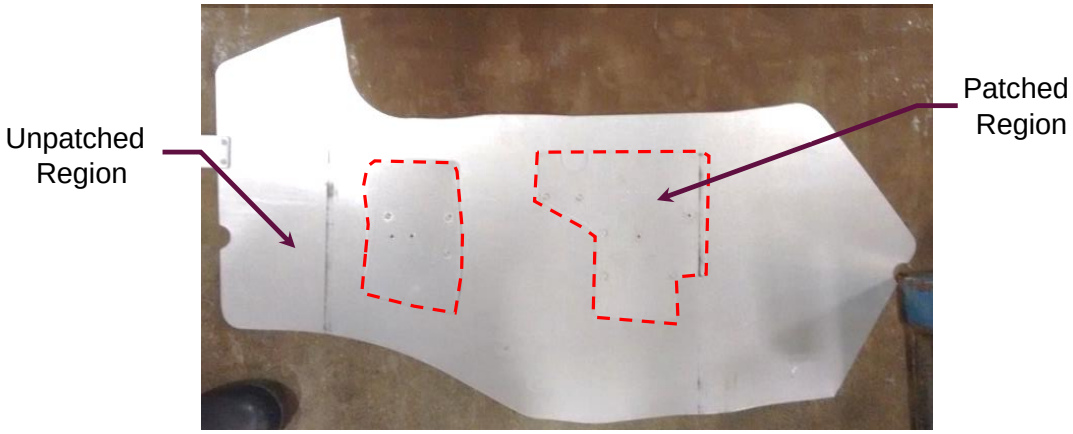

Figure 11: Unprocessed patched blank. The additional steel patch locally reinforces the blank to improve crashworthiness capabilities. Consequently, these areas of localized increase in thermal mass are highly susceptible to incomplete austenitization. The red dashed lines represent the patches.

an adequate, but not optimal, solution is identified. The trial-and-error process is complicated by the complex thermal and metallurgical processes that underlie blank heating and austenitization (all modes of heat transfer, temperature-dependent thermophysical and radiative properties, along with solid-state transport and kinetics), which makes an intuitive connection between the process parameters and the outcomes elusive. Thus, the need for a reliable numerical model to simulate simultaneous blank heating and austenitization is threefold:

1) Forecasting production costs, which Tier-1 suppliers could use to prepare competitive quotes for their OEM customers.
2) Troubleshooting to identify if the furnace parameters are sufficient to achieve complete austenitization, in case there are issues found with as-formed parts

3) Improve current industrial practices, and optimize production efficiency, by providing physical foundation for the relationship between blank heating, austenitization, and furnace parameters.

1.3 Models for Steel Reheating Furnaces

Various thermal models have been developed to simulate heating of steel slabs, billets, or blanks within industrial furnaces. The majority of the models [54-61] proposed in the literature are limited in their application to strictly predicting load heating curves. Heng et al. [55] proposed a heat transfer model of a roller hearth furnace used to austenitize steel in which the furnace interior was discretized into finite surfaces, and used to derive a radiosity matrix equation. The transient load was then evaluated using a two-dimensional Crack-Nicolson finite difference method, assuming that all the energy absorbed by the load increased the sensible energy. Their model was then incorporated into an optimization procedure to obtain optimal zone temperatures using a neural network. Other scholars [23, 54, 55] developed transient 1D and 3D heat diffusion models to estimate the temperature distribution and dropout temperatures of steels, which were subsequently used to identify the zone temperatures that minimized fuel consumption. In many studies [22, 23], however, the surfaces within each zone are modeled as isothermal at the zone set-point temperature, and the influence of the moving load on the local radiation field is neglected. The models reviewed in literature thus far do not relate load heating to phase transformation during heating. Accounting for the latent heat of austenitization during heating is crucial, as recently highlighted by Ganesh et al. [62], who modified Heng et al.'s [55] work by relating the latent heat of austenitization and obtained different optimal results.

In the context of HFDQ, Twynstra et al. [27] adopted the approach of [63, 64, 65], in which an effective specific heat, $c_{\mathrm{p,eff}}$, is defined by augmenting the specific heat, c_{p}, by dividing the latent heat of austenitization, (assumed to be 85000 J/kg [66]) with the difference between the austenite start and completion temperatures, T_{Ac1} and T_{Ac3}, assumed to be 730°C and 880°C [9, 10, 20] respectively. This treatment is equivalent to assuming that austenitization occurs uniformly between T_{Ac1} and T_{Ac3}. Jhajj et al. [23] improved upon this treatment by defining a temperature-dependent $c_{p,eff}$ based on inverse analysis of calorimetric data measured from furnace-heated

22MnB5 coupons. Their work showed that the latent heat of austenitization is not uniformly distributed between T_{Ac1} and T_{Ac3}; instead, the majority of the transformation occurs near T_{Ac1}. Tonne et al. [61] attempted to simultaneously infer $c_{p,eff}$ and the total emissivity of the blank (assumed to be grey) by regressing modeled temperatures of blanks heated within a roller hearth furnace to experimental data, although the recovered $c_{p,eff}$ differed significantly from the one found by Jhajj et al. [23] through inverse analysis.

The heat transfer models described above represent an improvement over the ones used by industrial operators to adjust furnace process parameters, but a more accurate prediction demands a coupled thermometallurgical model that explicitly includes phase transformation kinetics. This, in turn, requires a theoretical understanding of how the rate of austenitization is related to temperature. Roosz et al. [38] demonstrated how the initial microstructure influences nucleation and growth of austenite. They further modeled nucleation and growth separately by model regression of metallographic data [10]. In the case of isothermal processes, the austenite phase fraction, f_γ, grows according to the square root of the heating time [44], but this result does not apply directly to industrial processes, which are non-isothermal. Huang et al. [36] have shown that increased heating rates led to increased phase fraction of austenite during isothermal treatments. Caballero et al. [20] developed a two-stage kinetics model for austenitization by considering pearlite dissolution and ferrite to austenite transformation independently for non-isothermal heating.

More recently, Di Ciano et al. [10] derived an empirical first-order ("F1") model for 22MnB5 alloy, corresponding to an Avrami model with $n = 1$, based on dilatometry measurements carried out at constant heating rates, from 1°C/s-20 °C/s, within a Gleeble. In this model, austenite nucleation and grain growth, which are distinct processes in reality, were collectively represented by a single activation energy and rate constant, which are the only model parameters. Despite its simplicity, the model was shown to accurately predict instantaneous austenite phase fractions in coupons heated at constant rates as well as those that follow a furnace-like temperature profile.

Li et al. [25] recently reported an alternative phenomenological kinetics model for isothermal and non-isothermal annealing of 22MnB5. Their model relates heating rate effects on the austenite transformation via a power law. In contrast to Di Ciano et al.'s [10] F1 model, Li et

al.'s model explicitly accounts for the intermediate stages involved in the transformation procedure: nucleation, growth, and impingement. The corresponding model parameters were found by regressing predicted austenite phase fractions to those inferred from Gleeble-based dilatometry measurements carried out on coupons heated to temperatures between T_{Ac1} and T_{Ac3} and at different heating rates (1, 2, 5, and 25°C/s) and then held for a soaking period of 15 minutes.

1.4 Thesis Objectives

The aim of this research is:

(i) *Develop a thermometallurgical model for furnace-based austenitization of Al-Si coated 22MnB5 steel blanks heated within a roller hearth furnace*

(ii) *Identify the optimal parameters of a twelve-zone roller hearth furnace to identify optimal furnace parameters, which will minimize the cycle time*.

Uncertainties in the blank temperature and austenite phase fraction arising from uncertain furnace temperatures and austenitization model parameters are estimated using a Monte Carlo technique and summarized through 95% confidence intervals. The models are validated comparing predicted temperatures to thermocouple measurements and predicted austenite phase fractions to values inferred from Vickers microhardness measurements carried out on coupons extracted at intermediate times during heat treatment. Model validation was performed using an industrial roller hearth furnace and a laboratory scale muffle furnace. Initial validation was performed using the muffle furnace to verify model assumptions, ease of specific experimental validation, and replicative ability of heating conditions. Following the lab scale testing, industrial scale testing was performed on patched blanks.

This model then forms the basis for a multivariate optimization, with the objective of minimizing the cycle time for a twelve-zone roller hearth furnace, by optimizing the zone temperatures, length of cycle, and roller speed. The problem domain was initially analyzed using the interior point method (a gradient-based method), where nonlinear constraints were superimposed to the objective function by defining logarithmic barrier functions. The minimization problem was then assessed by using a hybrid algorithm, which coupled a genetic algorithm and the interior point method.

1.5 Overview of the Thesis

This work reports the development and application of the thermometallurgical model in five sections.

Chapter 2 focuses on characterizing the furnaces used in the study to validate the model. Initially, physical attributes of the furnace are discussed, including geometrical dimensions, control strategies, and temperature set-points.

Chapter 3 presents the derivation of the thermometallurgical submodel. The chapter outlines the assumptions and methodology used to develop the heat transfer submodel, from an energy balance. Subsequently, two candidate kinetics submodels will be considered for austenitization during heating. Finally, the independent models will be coupled in order to relate blank heating to phase transformation taking place, at any instant in time.

Chapter 4 shows how the thermometallurgical model can be used to predict incomplete austenitization for single- and double-gauge samples heated within a laboratory muffle furnace and industrial scale patch blanks in a fourteen-zone roller hearth furnace. The chapter begins by discussing the experimental setup for the muffle furnace followed by the roller hearth furnace. This section concludes by comparing experimentally inferred fraction austenite and thermal history to the model predictions.

Chapter 5 focuses on design optimization for minimizing the cycle time for a twelve-zone roller hearth furnace. Linear and nonlinear functional constraints will be identified and described in terms of industrial context. Two alternative austenite constraints are analyzed. The chapter concludes by examining how the optimal parameters vary based on the choice of the austenite constraint and choice of kinetics model.

Finally, *Chapter 6* summarizes the experimental and theoretical contributions of this research with recommendations for future work.

Chapter Two
Furnace Characterization

The surrounding temperature of a furnace wall constantly fluctuates about the set-point, a consequence of the hysteresis controllers (or any controller in general). Therefore, characterization of the furnace surroundings is necessary to incorporate appropriate boundary conditions in order to model blank heating and austenitization.

Two types of furnaces were used in this study: an industrial roller hearth furnace and a lab scale muffle furnace. The roller hearth furnace, manufactured by Schwartz GBMH, is located at Formet Industries in St. Thomas, Ontario. The smaller muffle furnace, manufactured by Thermolyne^{TM}, is located at the University of Waterloo. The muffle furnace provided the capability to recreate heating conditions similar to those observed in the roller hearth furnace, while permitting ease-of-access for instrumentation and, in principle, boundary conditions that are better characterized. The laboratory furnace served as a preliminary means to validate the thermometallurgical model and assess its predictive capabilities. Subsequent tests were carried out using the roller hearth furnace, in order to characterize the industrial process, and validate the finalized thermometallurgical model. These measurements were carried out with the aid of Formet personnel.

2.1 Roller Hearth Furnace

2.1.1 Furnace Geometry

The roller hearth furnace involved in the study was approximately 33 m in length and 2 m wide, and consisted of 14 zones, some of which are thermally isolated from each other by baffles as shown in **Figure 12**. Batches, consisting of at most four blanks, are placed onto ceramic rollers with a minimum spacing between successive loads to facilitate ease of loading and unloading

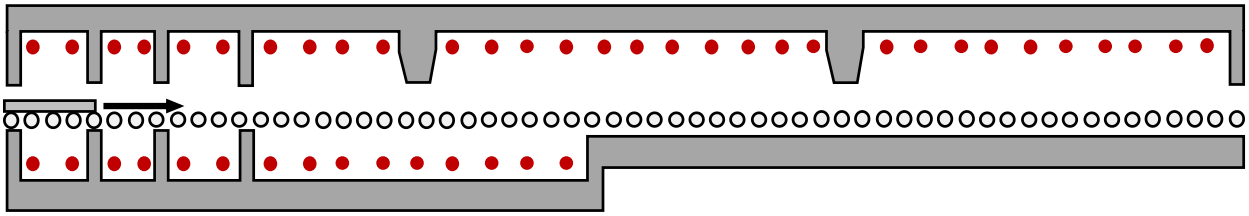

Figure 13: Cross-sectional view of a roller hearth furnace used in HFDQ. The furnace consists of several independently controlled heating zones. Radiant tube burners (red circles) are located above and below the ceramic rollers (white circles).

performed using robotic arms, as shown in **Figure 13**. Ceramic rollers, uniformly spaced along the furnace length, are used to convey blanks through the furnace, which are irradiated from the top and bottom by natural gas-fired radiant tube heaters. Radiant tube burners are positioned above and below of the ceramic rollers within the first 15 m, while they are only located over the top for the remaining 15 m, and they are positioned closely together in the first half of the furnace. This is because greater heating capacity is needed to bring the blanks to the austenitization temperature over the first half of the furnace, while the radiant tube heaters in the latter half of the furnace are used to maintain the temperature of the blanks, which requires less heating capacity.

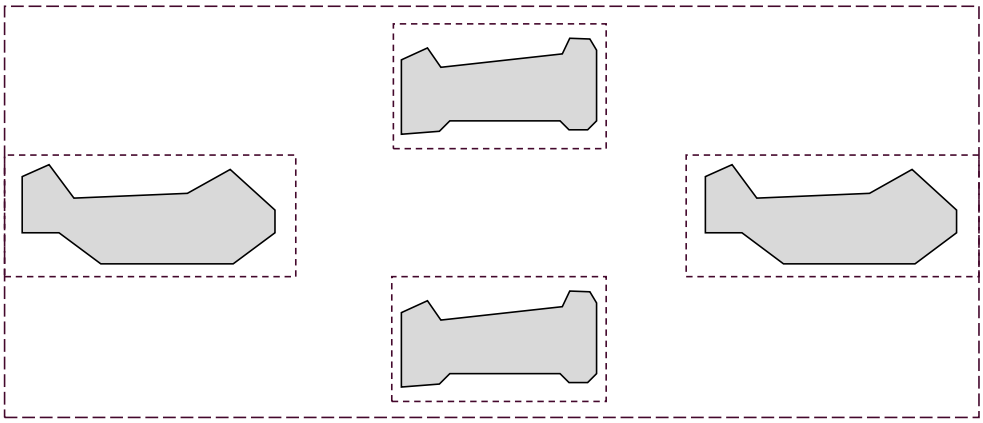

Figure 12: Batch layout. Batches consist of at most four blanks. Each successive batch is loaded with a minimum gap spacing to ensure ease of loading and unloading performing using automated robotic arms.

2.1.2 Control Strategy

Patched and unpatched blanks of varying geometry and thickness are heat treated within the roller hearth furnace. The blank thickness varies from 1 mm (unpatched) to 4 mm (patched), and the required heating time to anneal the blanks ranges from 3 to 8 minutes. The zone temperature set-points needed to fulfill the functional requirements of the heating phase (*i.e.* austenitization and Al-Si layer transformation) are largely chosen through trial-and-error by the furnace operators. The zone temperatures are maintained using a hysteresis controller with feedback provided from grounded K-type thermocouples suspended in each zone of the furnace. The K-type thermocouples measure when the set-point temperature of each zone exceed an upper and lower bound (typically ±20°C), thus controlling when to turn the fuel supply on or off.

During daily operations, the surrounding set-point temperature is seldom modified between different production cycles. Rather, different blank thicknesses are accommodated by modifying the roller speed, with thicker blanks requiring more time in the furnace. This adjustment is performed in a heuristic way and due to the complex and non-intuitive relationship between blank heating, austenitization, and furnace parameters the current method is far from optimal.

2.1.3 Roller Hearth Furnace Characterization

As mentioned in §2.1.2, the temperature of each zone is regulated using a K-type thermocouple that is installed on a sidewall, halfway between the ceramic rollers and the ceiling of the furnace. Jhajj et al. [67] previously characterized a similar 12-zone roller hearth furnace. In their characterization study, 15 additional K-type thermocouples were installed, five each in zones 2, 5, and 11 (*i.e.* near the entry, middle, and exit, respectively) in order to monitor variations within a zone and gain detailed understanding of the furnace temperature profile. Within each zone, two thermocouples were installed on the surface of the radiant tube; one on each end of the tube. One thermocouple was attached to the surface of the sidewall insulation, whilst one grounded and one ungrounded thermocouple were used to measure the ambient air temperature. **Figure 14** shows the thermocouple locations within the furnace.

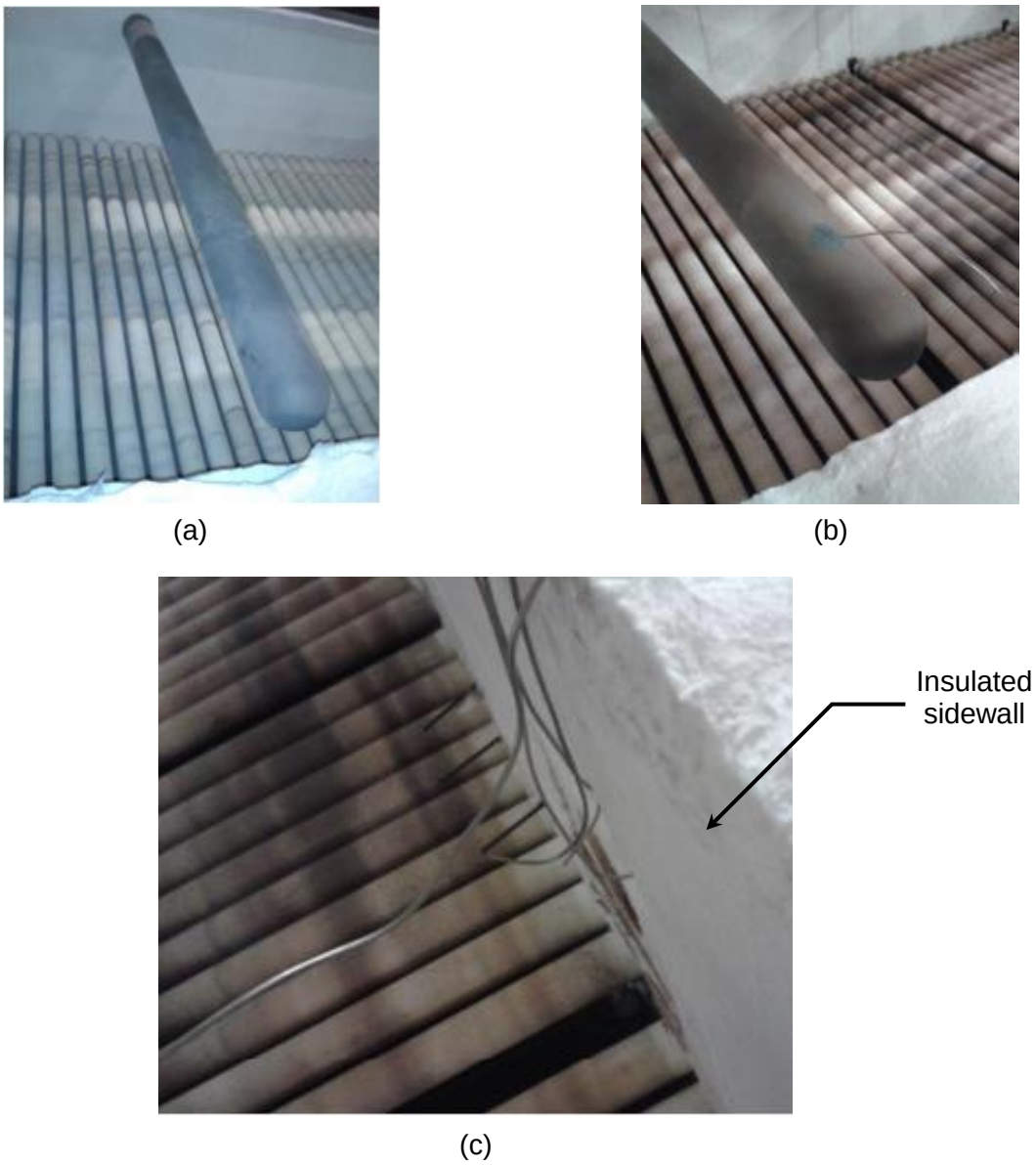

Figure 14: Location of the additionally installed thermocouples from Jhajj et al.'s [67] study. (a) Full length of a radiant tube, (b) Thermocouple positioned near the circular end of the tube using ceramic paste, (c) Installation of thermocouple on the insulating sidewall.

The temperature distribution of zone 2 is shown in **Figure 15**. The measured temperature profile reflects a cyclic trend, which is symbolic of the hysteresis control strategy. The temperature profile shows that the radiant tube burner is at the highest temperature. The radiated energy from the tubes heat the surrounding atmosphere and the walls. The local atmosphere temperature is higher than that of the walls, due to loss of energy from the furnace walls to the external cooler

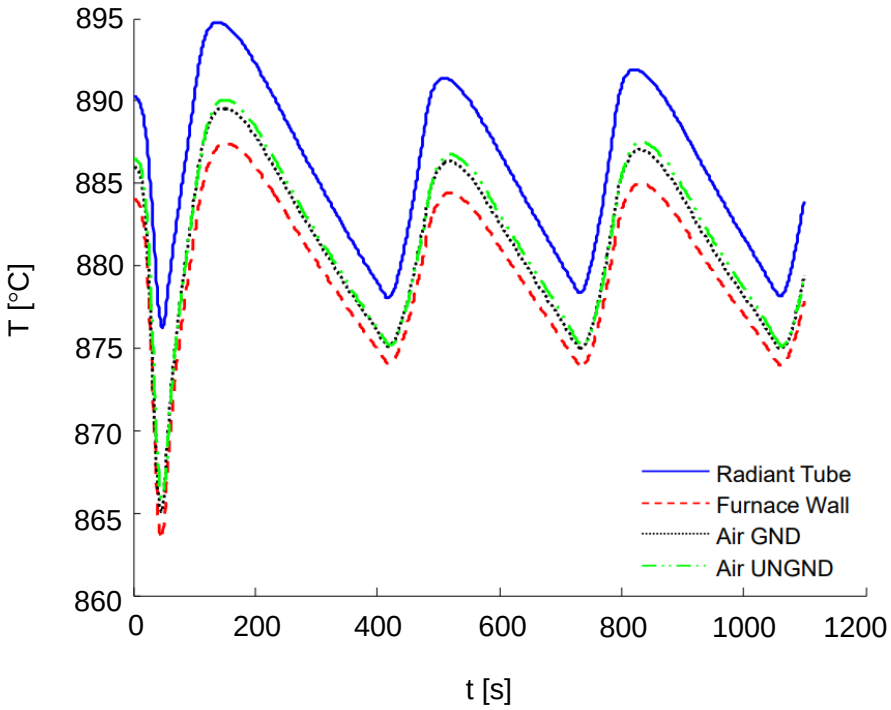

Figure 15: Temperature measurements made by Jhajj et al. [67] for zone 2 of a twelve-zone roller hearth furnace.

surroundings and furnace opening, as indicated in **Figure 15**. The difference between the surface of the radiant tube and the furnace walls is approximately 10°C, and the grounded and ungrounded thermocouple measurements were nearly identical throughout the process. The amplitude of the fluctuations within zone 2 is between 5-7°C over a period of approximately 400 seconds. The zone located in the middle of the furnace would experience reduced variation due to lower heat loss compared to the zones at the beginning and end, due to greater losses through the furnace openings. The cyclic trend becomes more frequent when heating blanks with larger thermal mass due to greater energy absorption from the surroundings, causing frequent cycling of the radiant tube burners. When developing a reliable model for furnace-based austenitization, it may be necessary to incorporate the temperature fluctuations. Model development and experimental analysis, discussed in chapters 3 and 4, make the assumption that all zones exhibit the same cyclic behavior in the temperature distribution.

2.2 Laboratory Muffle Furnace

2.2.1 Furnace Geometry

The Thermolyne^{TM} muffle furnace used in this thesis, shown in **Figure 16,** is identical to the one described by Jhajj et al. [23]. It is significantly smaller in size compared to the roller hearth furnace, having internal dimensions of 230 x 230 x 460 mm. The muffle furnace is heated using a pair of electrical resistance elements, with a serpentine configuration, embedded within the upper and lower ceramic walls. The heaters are controlled using a single unshielded K-type thermocouple, located at the rear of the furnace, which measures the local ambient temperature. The measured reading is transmitted to a PID controller, which further regulates the surrounding temperature. Similar to the roller hearth furnace, a hysteresis control strategy is implemented; the heating elements are activated or deactivated when the temperature exceeds an upper and lower bound (typically ±20°C), relative to the set-point temperature. Within the furnace two coupons, patched and unpatched, are simultaneously heated in a side-by-side configuration, while being positioned on a ceramic platform. The patched coupon is located on the rear of the platform, whereas the

Figure 16: Thermolyne^{TM} lab scale muffle furnace utilized for in-house heat treatment. This furnace was further used to validate the thermometallurgical model, discussed in Chapter 4.

unpatched coupon is near the front. In order to thoroughly model coupon heating, characterization of the furnace surroundings may be necessary as the heating conditions near the patch may vary compared to the unpatched coupon due to potential thermal gradient within the furnace.

2.2.2 Muffle Furnace Characterization

Since the coupon is heated primarily by radiation from the surrounding surfaces, it is important to characterize how the temperature of these surfaces may depart from the set-point temperature measured by the control thermocouple. The reason for the variation in the temperature is that when the furnace door is opened and closed, to load the patched and unpatched samples, each surface is cooled by radiative exchange with the surroundings, and some volume of the cooler air also enters the furnace. Generally, since the door is always cooler compared to the remaining surfaces it absorbs energy throughout the heating process.

In order to characterize the temperatures of the surrounding surfaces, four additional thermocouples were installed within the muffle furnace: one on the inside of the door, one to measure the ambient temperature directly near the test samples, and two along the length of the left furnace wall. Mounting the thermocouples directly to the walls resulted in unrealistic data due to some current leakage from the embedded electrical heaters into the thermocouple wires. To overcome this issue, a pseudo wall was made, from Pyrotek Pyrite N-17 refractory ceramic, a calcium silicate board, to which the thermocouples were attached using a Pyro putty, a metallic and ceramic paste. The pseudo wall was 1 mm thick and located as close to the left furnace wall as possible to reduce thermal and measurement lags. It was assumed that all heaters operate symmetrically, and thus the temperature measurements should exhibit bilateral symmetry.

The temperature distribution within the furnace is shown in **Figure 17**. When the part is loaded, the door and front wall experience the greatest drop in temperature compared to the back furnace wall and ambient temperature. The door temperature is the lowest throughout the heating duration, which may be due to lack of proper insulation and higher energy loss to the surroundings. A noticeable temperature gradient is evident along the depth of the furnace, which may be attributed to poor insulation along the front and rear. This information will form the basis of an

uncertainty measurement quantification that will be incorporated into the thermometallurgical model.

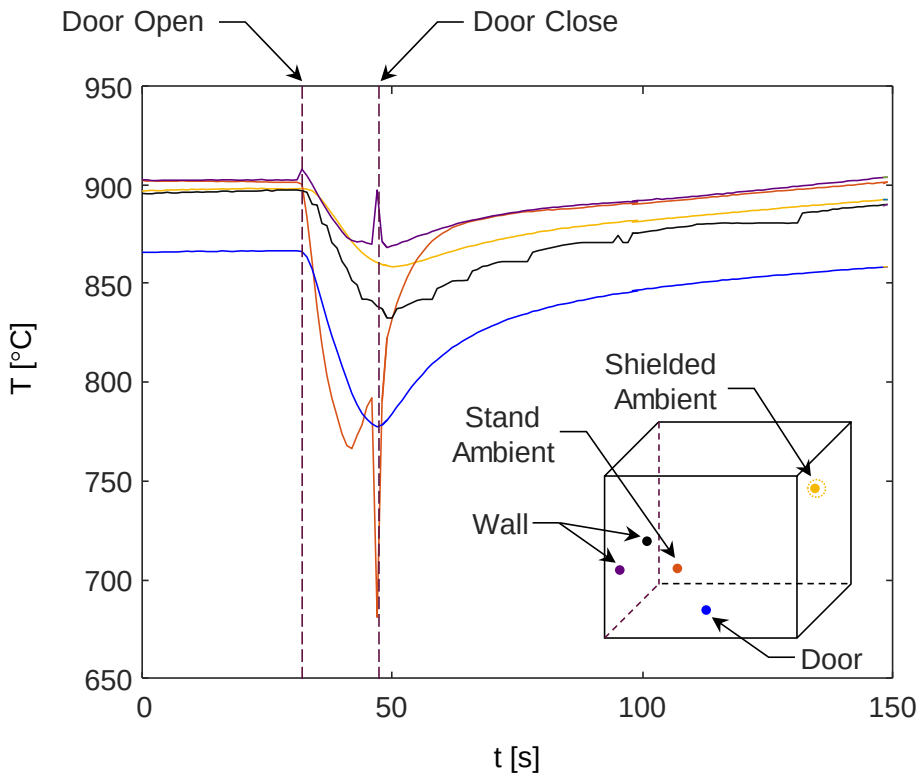

Figure 17: Measured temperature variation of the laboratory scale muffle furnace during blank heating.

Chapter Three
Thermometallurgical Model

In order to relate the heating and austenitization kinetics of the 22MnB5, within the muffle furnace and roller hearth furnace, a thermometallurgical model is necessary. Previously published furnace-based austenitization heat transfer models for HFDQ [23, 27] implicitly accounted for austenitization by defining an effective specific heat [63-65]. In practice, the predicted heating curves are compared against the functional requirements of the furnace (*e.g.* enforcing a minimum 30 second soak time above 900°C) to ensure that the blanks have been completely (or near completely) austenitized. Since past literature does not explicitly connect the blank heating and the transformation kinetics, the proposed thermal models are limited in their utility and predictive capability. It is thus necessary to derive a model that explicitly couples the two parameters.

3.1 Heat Transfer Submodel

Prior to developing a thermal model, it is essential to understand the modes of heat transfer involved in this process. Since the furnace operates at approximately 950°C, the dominate heat transfer mode is radiation, followed by convection, and conduction, as explained below.

Many thermal models for furnace-based austenitization evaluate the load's 3D temperature profile [23, 55]; this is not only computationally intensive but also difficult to implement in industrial settings. Since the blanks are very thin relative to their planar dimensions, it is reasonable to neglect the temperature distribution along the thickness. This assumption is justified by evaluating the radiative Biot number, which compares the ratio of thermal resistance between radiation to the surface (define in the linearized form) and conduction within the steel.

$$Bi = \frac{\mathrm{R}_{\mathrm{internal}}}{\mathrm{R}_{\mathrm{external}}} = \frac{t_{blank} \big/ \left(k_{22MnB5} \cdot A\right)}{1 \big/ \left(h_{rad} \cdot A\right)} = \frac{h_{rad} \cdot t_{blank}}{k_{22MnB5}} \tag{3.1}$$

where the linearized radiative heat transfer coefficient is,

$$h_{rad} = \varepsilon\sigma(T_{blank} + T_{surr})(T_{blank}^2 + T_{surr}^2) \tag{3.2}$$

Considering the case when the blank first enters the furnace, assuming that $\varepsilon = 0.3$, $T_{blank} = 300$ K, $T_{surr} = 1000$ K, $t_{blank} = 3$ mm (worst case for the patched region), and $k_{22MnB5} = 39$ W/(m·K) [68], then $Bi = 1.9\times10^{-3}$. Since Bi << 0.1 [69], this analysis supports the aforementioned assumption that there is negligible thermal gradient along the blank thickness. In the case of single-gauge blanks, it is reasonable to assume that the blank temperature is spatially uniform since the surrounding surfaces are locally isothermal (*i.e.* the blank "sees" isothermal surroundings), justifying a thermally-lumped model.

Problem complexity increases with the introduction of patches, shown in **Figure 18**, as differences in thermal masses between the unpatched and patched areas results in nonuniform temperature distribution, and in principle net heat conduction between the unpatched and patched region. A detailed finite volume model published by Jhajj et al. [23] have shown that lateral conduction was insignificant, due to the thin cross-section of the blank. Patched blanks are thus modeled using three thermally lumped regions, defined in **Table 3**, and as shown in **Figure 18**. Regions "A" and "B" are decoupled due to the negligible conduction heat transfer between them, as per the findings of Jhajj et al.'s [23] model. However, the net heat conduction via an air gap between regions "B" and "C" was considered by defining an overall heat transfer coefficient.

Table 3: Summary of the control volumes used to derive the thermal model for patched blanks

Region "A"	Unpatched blank
Region "B"	Substrate beneath the patch
Region "C"	Patch

The upper and lower surfaces of the blank are assumed to experience equivalent radiative boundary conditions. It is assumed that the walls below the rollers in the second half of the furnace is at thermal equilibrium with the surroundings and radiates the blanks from the bottom. Models proposed by Heng et al. [55] and Ganesh et al. [62] evaluate the load heating profile by considering a view factor analysis and treating the surroundings as non-isothermal. The present model assumes

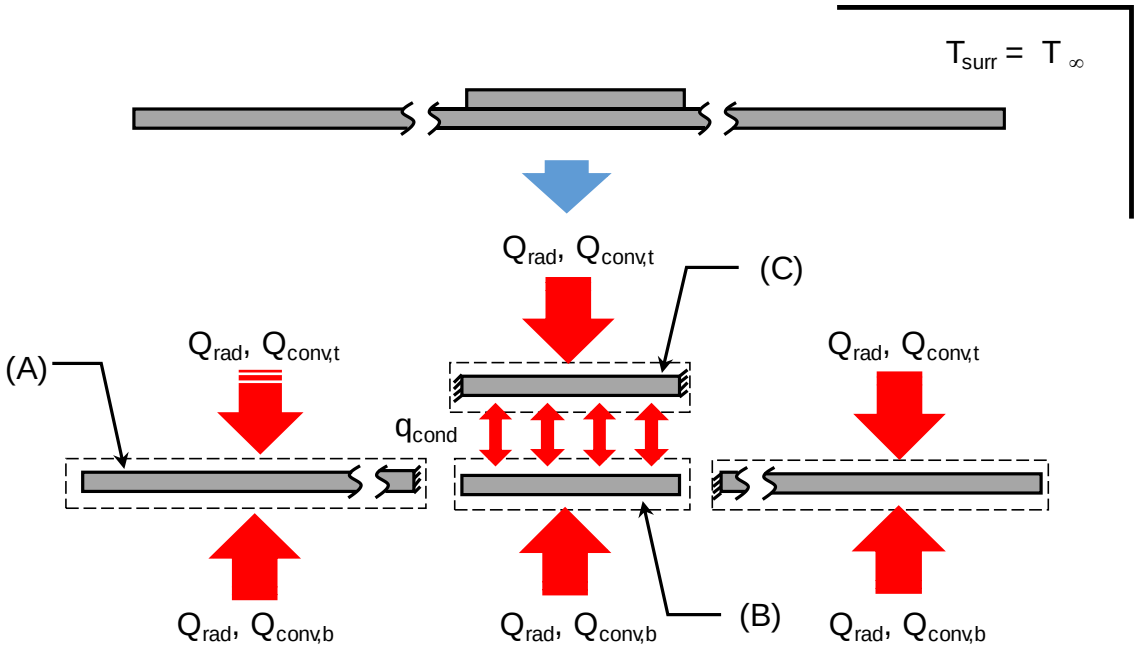

Figure 18: Control volumes used to formulate the heat transfer submodel: "A", unpatched blank; "B", blank beneath the patch; and "C", the patch. Heat conduction between "A" and "B" is neglected based on the finite difference study by *[20]*, but heat conduction across the air gap separating "B" and "C" is considered.

that the furnace surroundings are locally isothermal and the local irradiation experiences negligible influence with the presence of the blank (*i.e.* the small object/large isothermal enclosure assumption [69, 70]. The assumption is further supported by the fact that the surface area of each zone, in the roller hearth furnace, is significantly greater than that of the blank. Moreover, the furnace atmosphere is quiescent and at thermal equilibrium with the surroundings.

With these assumptions and boundary conditions, the temperature of each region of the blank may be determined at any instant of time by solving three coupled differential equations.

$$\rho_{22MnB5} c_{p,eff} V_j \frac{dT_j}{d\tau} = Q_{rad,j} + Q_{conv,j} + Q_{cond,j} \tag{3.3}$$

where subscript "*j*" denotes regions "A", "B", or "C", ρ and $c_{p,eff}$ are the temperature dependent density [68] and effective specific heat [23] of 22MnB5, V_j is the unpatched or patched volume, $dT_j/d\tau$ is the rate of change in region *j*'s temperature, $Q_{rad,j}$ and $Q_{conv,j}$ are the radiative and

convective heat transfer rates, $Q_{cond,j}$ accounts for heat conduction only between the patch covered blank and the patch ("B" and "C"), τ is the instantaneous time. The different modes of heat transfer involved in the model development and analysis are schematically depicted in **Figure 18**.

The radiative heat transfer between region *j* and the surrounding surfaces, at any instant, is defined by

$$Q_{rad,j} = \sigma A_j \left[\alpha\left(T_{s,j}, T_{surr}\right) T^4_{surr} - \varepsilon\left(T_{s,j}\right) T^4_{s,j} \right] \tag{3.4}$$

where A_j is the exposed surface area (defined for both sides of "A", single side for "B" and "C"), $\sigma = 5.67\times10^{-8}$ W/(m^2·K^4) is the Stefan-Boltzmann constant, and α and ε are the total absorptivity and emissivity. The radiative properties are a function of T_{surr} and T_s respectively via the spectral distribution of the irradiation, $G_\lambda \propto E_{b,\lambda}(T_{surr})$ and blank emissive power, $E_{b,\lambda}(T_s)$ and also through the spectral emissivity of the blank, which changes as the Al-Si coating melts (~575°C) and then transforms into the Al-Si-Fe intermetallic layer [30].

Newton's Law of Cooling governs the rate of convective heat transfer between the blanks and the furnace atmosphere

$$Q_{conv,j} = \bar{h} A_j \left(T_\infty - T_{s,j}\right) \tag{3.5}$$

where $\bar{h}$ is the average convection coefficient over the upper or lower surface of the blank, and T_∞ represents the air temperature. The convection coefficients are determined from the Nusselt number

$$\overline{Nu} = \frac{\bar{h} L_c}{k_{air}(T_{film})} \tag{3.6}$$

where $L_c = A_s/P$ represents the characteristic length (A_s is the wetted surface area of the blank and P is the perimeter), and k_{air} is the thermal conductivity of the air defined as a function of the film temperature with units of [K],

$$T_{film} = \frac{1}{2}(T_{surr} + T_{s,j}) \tag{3.7}$$

Since the blanks are conveyed through the furnace zones at a slow rate (*i.e.* at max 100 mm/s), so buoyant forces dominate inertial forces and convection can be modelled as natural convection. The Nusslet numbers over the top and bottom of the blank, respectively, are found from [69, 71]

$$\overline{Nu}_{upper} = 0.52 Ra_{L_c}^{1/5} \tag{3.8}$$

$$\overline{Nu}_{lower} = 0.54 Ra_{L_c}^{1/4} \tag{3.9}$$

where *Ra*, the Rayleigh number, is defined by

$$Ra_{L_c} = \frac{g\beta\left(T_\infty - T_{s,j}\right)L_c^{\,3}}{\alpha_{air}\nu_{air}} \tag{3.10}$$

$\beta = 1/T_{\text{film}}$ is the volumetric thermal expansion coefficient of air, α_{air} and ν_{air} are the thermal diffusivity and kinematic viscosity of air, both of which are dependent on the $T_{film.}$ The ambient air is assumed to be in local thermal equilibrium with the respective zone.

Due to different convection heating rates on the upper and lower surfaces of the blank, heat conduction via the air gap, separating regions "B" and "C", can be considered, although it is smaller in magnitude compared to the other heating modes. Conduction into region "B" from "C" is determined by

$$Q_{cond,C\to B} = UA_j\left(T_{s,C} - T_{s,B}\right) \tag{3.11}$$

where A_j is the interfacial area and U is a conservative, lower bound, overall heat transfer coefficient estimated by assuming heat is exclusively conducted across the air gap (*i.e.* no radiative transfer),

$$U = \frac{k_{air}}{t_{gap}} \tag{3.12}$$

Following the treatment of [23] an air gap thickness of approximately 0.1 mm was assumed.

Heat transfer also occurs between the rollers and the blank through some small but finite contact area. The rollers reach a state of thermal equilibrium with the local zone temperature, in

the absence of blanks. However, due to periodic contact with the blanks it is expected that the temperature will be between the blank and surroundings. As the rollers heat the blank, they also interfere with radiation and convection on the blank underside. Due to the complexity and uncertainties associated with the roller/blank interaction, heating from the rollers was not considered in Eq.(3.3), with the assumption that this omission will be compensated by the increased convection and radiation on the blank's bottom surface.

3.2 Thermophysical Properties of Usibor® 1500AS

Characterization of the material's thermophysical properties is crucial to reliably model the heating stage. Temperature-dependent density, specific heat, and thermal conductivity of Usibor® 1500AS are provided by Arcelor Mittal [68], summarized in **Table 4**.

The manufacturer-supplied specific heat only considers the sensible energy, that is the energy required to simply raise the temperature of the steel per unit mass, stored by the ferrite, pearlite, and austenite grains during heating. This ignores the latent component, the energy absorbed by the blank for solid phase transformation. Excluding this contribution would result in an over-prediction of the heating rate and final part temperature [23]. A severe consequence of utilizing only the sensible energy in the optimization of the furnace parameters could be the potential risk of incomplete blank austenitization [23].

The specific heat of a material is often characterized through differential scanning calorimetry (DSC), as was done by Krielaart et al. [60] to determine the latent energy required to transform a pure pearlitic structure to austenite. Jhajj et al. [23] argue that measurements from the DSC are appropriate for HFDQ since the heating rates achieved by the device (~1°C/s) are lower compared to what is observed in the roller hearth furnace (~3-5°C/s) during austenitization. To overcome this hurdle an effective specific heat, $c_{\mathrm{p,eff}}$, is defined and utilized as a surrogate to account for both the sensible and latent components. As mentioned in §1.3, Twynstra et al. [27] assumed the effective specific heat to be uniformly distributed throughout the austenitization regime (T_{Ac1} and T_{Ac3}). The isothermal annealing study conducted by Garcia and Deardo [72] contradicts this approach of defining a uniform $c_{\mathrm{p,eff}}$, as their work shows a strong correlation between temperature and phase transformation. Jhajj et al. [23] also show that $c_{p,eff}$ is not uniformly

Table 4: Temperature dependent thermophysical properties of Usibor® 1500AS [68]

Temperature [°C]	Conductivity [W/(m·K)]	Density [kg/m³]	Specific Heat [J/(kg·K)]
0	38.6	7880.8	433
50	38.9	7864.5	444
100	39.5	7848.0	465
150	39.9	7831.5	485
200	40.4	7814.8	505
250	41.0	7797.7	525
300	40.7	7781.0	547
350	40.9	7763.9	571
400	40.6	7746.6	598
450	40.1	7729.2	628
500	39.5	7711.7	628
550	38.5	7694.0	701
600	37.4	7676.2	748
650	35.9	7658.3	804
700	34.4	7640.2	876
725	37.4	7631.1	924
750	40.3	7622.0	971
800	39.7	7603.7	942
850	25.1	7585.2	825
880	26.0	7574.0	793
900	26.6	7566.6	771
950	27.3	7567.0	741
1000	27.9	7567.0	723
1050	28.3	7567.0	711
1100	28.6	7567.0	706
1150	29.2	7567.0	706
1200	29.7	7567.0	706

distributed; it is biased towards T_{Ac1} suggesting majority of the austenitization takes place near the T_{Ac1}. The experimental studies of Li et al. [24, 25] on the isothermal and non-isothermal

austenitization of 22MnB5 support the findings of [23]. **Figure 19** compares the specific heat provided by Arcelor Mittal [68] with the effective specific heats proposed by [23] and [27].

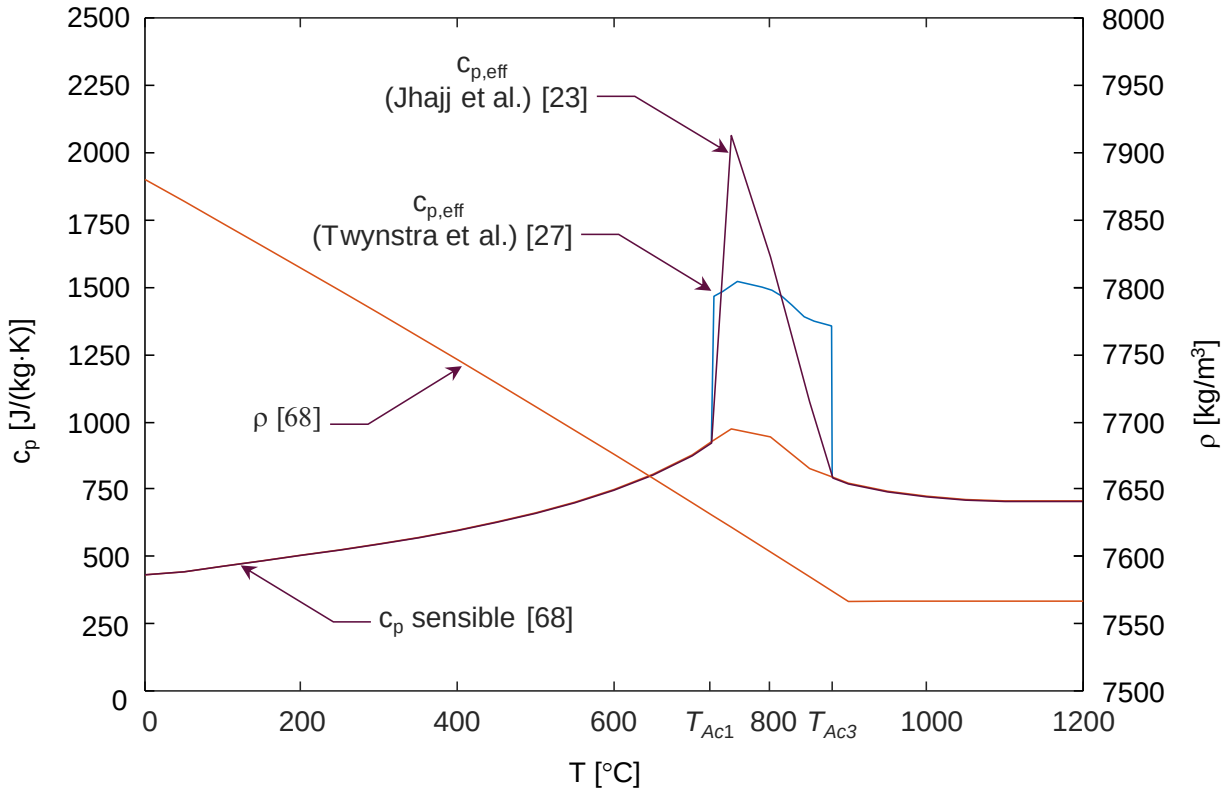

Figure 19: Thermophysical properties of Usibor® 1500AS as function of temperature. The manufacturer [68] supplied specific heat and density are plotted. Effective specific heats modeled by Twynstra et al. [27], assumed latent heat to be uniformly distributed, and Jhajj et al. [23], showed latent heat is non-uniformly distributed over the austenitization regime. Both model latent heat as 85000 J/kg [66].

3.3 Radiative Properties of Usibor® 1500AS

The dominant mode of heating in this work comes from radiation, so characterization of the steel's radiative properties is of utmost importance in order to accurately model blank heating. According to the work of Jhajj et al. [23] and Shi et al. [30] the radiative properties below the Al-Si coating eutectic temperature (~575°C) are consistent with the manufacturer supplied values; however,

these properties exhibit dramatic changes beyond 575°C, due to morphological and chemical changes in the coating, thereby influencing blank heating.

Jhajj et al. [23] carried out a detailed experimental study in order to quantify the total emissivity and absorptivity of the blanks. They had conducted *in-situ* and *ex-situ* measurements of the spectral emissivity (ε_λ), collected using an OceanOptics NIRQuest near-infrared spectrometer and a SOC 400 FTIR reflectometer, respectively. The OceanOptics NIRQuest is capable of directly measuring the spectral emissivity, whereas the FTIR reflectometer measures the near-normal spectral reflectivity (ρ_λ). In their method Al-Si coated samples of 22MnB5 were heated from 575-950°C, using a Gleeble® thermomechanical simulator based on a temperature profile obtained from instrumented blanks heated within a roller-hearth furnace. The spectrometer, mounted within the Gleeble®, is effective from 0.9-2.5 μm and the FTIR reflectometer provides characterization over 2-25 μm; thus, the combination of these two devices provided a broader wavlength over which characterization could be performed. *Ex-situ* measurements were solely conducted using the FTIR because the experimental setup would not allow the sample surface to sit flush against the device opening and the data collection rate is significantly slower compared to the spectrometer. Thus, *ex-situ* measurements involved heating the samples to the designated temperatures and then immediately air quenching them to preserve the microstructure and chemical composition of the coating.

Jhajj et al. [23] found that the FTIR was not suitable for inferring ε_λ between 575-700°C as the airflow, from the quenching process, distorted the surface morphology of the liquefied coating. As a result, the radiative properties were determined using the NIR spectrometer. The ε_λ can be determined from the ρ_λ, via the FTIR, from the 1st law of thermodynamics

$$\rho(\lambda,\theta,\phi)+\alpha(T,\lambda,\theta,\phi)=1 \tag{3.13}$$

The ρ_λ is related to ε_λ by Kirchoff's Law stating that for any surface $\varepsilon(T, \lambda, \theta, \phi) = \alpha(T, \lambda, \theta, \phi)$. Since the sample surface is diffuse (*i.e.* irradiation is isotropic) the directional dependence is neglected, thus Eq. (3.13) can be restated as

$$\varepsilon_\lambda = 1-\rho_\lambda \tag{3.14}$$

Spectral emissivity obtained using the NIR spectrometer and determined from the FTIR reflectometer are shown in **Figure 20a**.

The total (or spectrally averaged) hemispherical emissivity, $\varepsilon(T_b)$, is computed by [70]

$$\varepsilon(T_b) = \frac{\int_{\lambda=0}^{\lambda=\infty} \varepsilon_\lambda(T_b) \bullet E_{\lambda b}(T_b)\, d\lambda}{\sigma T_b^4} \tag{3.15}$$

where T_b is the temperature of the sample surface, $E_{\lambda b}(T_b)$ is the spectral black body radiation at the temperature the sample was heated. Since the sample is irradiated from black surroundings, the total hemispherical absorptivity, $\alpha(T_b)$, is determined by integrating over all wavelengths [70]

$$\alpha(T_b) = \frac{\int_{\lambda=0}^{\lambda=\infty} \varepsilon_\lambda(T_b) \bullet E_{\lambda b}(T_b)\, d\lambda}{\sigma T_b^4} \tag{3.16}$$

In both Eq. (3.15) and (3.16), T_b was assumed to be the temperature at which the blank was quenched, although measurements made using the FTIR were performed at room temperature. **Figure 20b** displays the total emissivity and absorptivity of the Al-Si coated blanks inferred from the spectral measurements. Both ε and α decrease upon reaching the coating melting temperature (~575°C) due to the liquid surface of the coating. As the coating solidifies, the radiative properties show an increase as a result of the various new phases being formed within the Al-Si coating [30].

3.4 Non-isothermal Transformation Kinetics Models

Industrial heating processes are mainly non-isothermal, followed by a period of nearly isothermal soaking, with the objective of reaching a fully austenitic (γ) structure. In order to ensure sufficient austenitization, it is critical to understand the coupling between the blank temperature history and the metallurgical transformations occurring within the blank. This thesis focuses on two distinct non-isothermal austenite kinetic models specifically designed for heating of 22nB5. The first model analyzed is an empirical first-order (F1) kinetics model developed by Di Ciano et al. [10] derived from dilatometry data, which encompasses growth and nucleation within two

model parameters, the pre-exponential factor and activation energy. The second model is a more physical-based model derived by Li et al. [25], which explicitly accounts for growth, nucleation, and impingement processes.

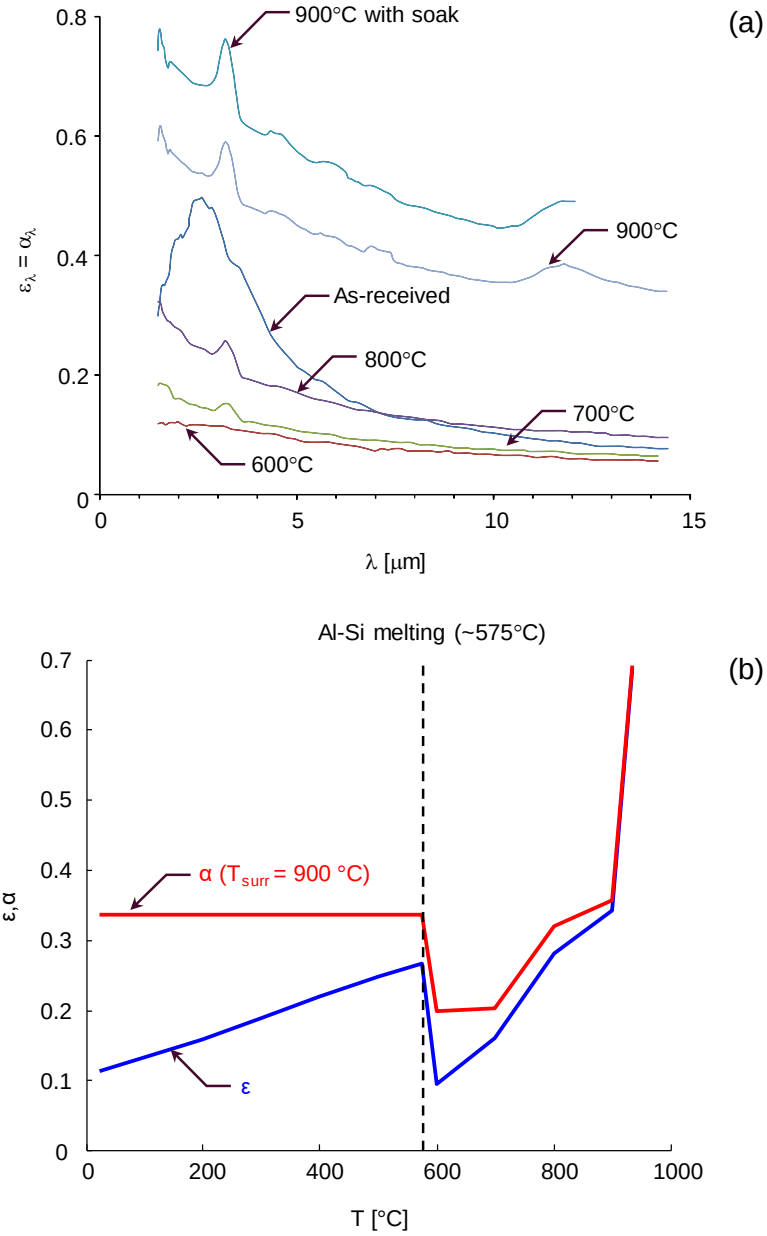

Figure 20: (a) Spectral emissivity of the Al-Si coated blanks, experimentally determined by Jhajj et al. [23], at various sample temperatures from Gleeble heated coupons. (b) Total emissivity and absorptivity of the Al-Si coated blanks determined from the experimentally obtained ε_λ measurements [23].

3.4.1 First-order (F1) Kinetics Model

Di Ciano et al. [10] derived an empirical austenitization model for non-isothermal heating of 22MnB5 beyond T_{Ac3}. The F1 model is mathematically similar to an Avrami-type model with n = 1. The model calculates the amount of fraction austenite formed by solving

$$\frac{dw}{d\tau} = A\exp\left(\frac{-E_A}{RT(\tau)}\right) \tag{3.17}$$

where A is the pre-exponential factor [s^{-1}], E_A is the activation energy [J/mol] required for the phase transformation to proceed, R = 8.314 J/(mol·K) is the ideal gas law constant, and w is the intermediate variable that relates the temperature to the fraction austenite formed, f_γ, expressed as

$$f_\gamma(\tau) = 1 - \exp\left[-w(\tau)\right] \tag{3.18}$$

The key aspect of this model is that the nucleation, growth, and impingement mechanisms are expressed within the activation energy (defining the energy input required to overcome the activation barrier to enable solid-state transformation). The E_A and A parameters were derived from dilatometry measurements carried out on uncoated 22MnB5 coupons heated at constant ramp rates ranging from 1-20°C/s using a Gleeble® thermomechanical simulator. The instantaneous austenite phase fraction was then inferred by applying an empirical lever-type rule [36] to yield $df_\gamma/d\tau$ for a given heating rate, as shown in **Figure 21**.

Each set of dilatometry measurements was used to derive a pair of [E_A, $\log_{10}(A)$] parameters. The parameters derived for heating rates between 1-5°C/s, representative of furnace-based heating, were binned and found to obey a multivariate normal (MVN) distribution, $[E_a, \log_{10}(\mathbf{A})]^T \sim \mathcal{N}(\boldsymbol{\mu}, \boldsymbol{\Gamma})$, with

$$\boldsymbol{\mu} = \begin{bmatrix} 402 \\ 18.5 \end{bmatrix},\ \boldsymbol{\Gamma} = \begin{bmatrix} 617 & 31.5 \\ 31.5 & 1.68 \end{bmatrix} \tag{3.19}$$

These distribution parameters were then used to derive a 90% confidence interval to account for model uncertainty associated with the parameters, E_A and A. Although Eqs. (3.17) and (3.18) do

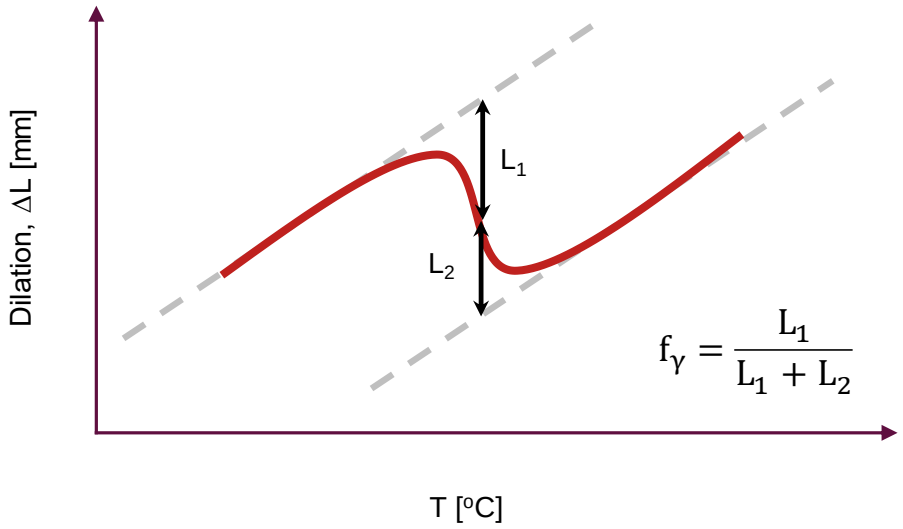

Figure 21: Sample dilatometry data for heating rate of 1°C/s. The instantaneous phase fraction of austenite was inferred from the dilatometry data using a lever-type rule.

not explicitly reflect the stages of the transformation kinetics, it reliably replicates experimental trends. Di Ciano et al. [10] stated that although the model precludes stages associated with the detailed kinetics, included in the work of Roosz et al. [38] and Li et al. [24, 25], it is still preferred over a high-fidelity model due to a lower number of variables, reduced parameter uncertainty, and minimized potential of parameter "over-tuning". One area of weakness associated with the model, however, is its inability to capture saturated austenite formation, in which the steel is heated to and held at soaked temperature between T_{Ac1} and T_{Ac3}. As noted above, this would result in an equilibrium phase distribution containing both austenite and ferrite, but this condition cannot be captured by the model. Since intercritical annealing of 22MnB5 is rarely done in an industrial setting, this limitation does not unreasonably limit the applicability of this model.

The F1 model was validated by comparing the predicted austenite phase fraction with values inferred from Vickers micro-hardness measurements using a 1 kg load, on coupons heated and then rapidly quenched at intermediate temperatures within the Gleeble®. Di Ciano et al. [10] inferred f_γ, using an empirical linear interpolative formula, adopted from Huang et al. [36]

$$f_\gamma(T) = \frac{H_T - H_0}{H_{T_{Ac3}} - H_0} \tag{3.20}$$

where H_0 = 180 HV, H_{TAc3} = 505 HV, and H_T is the Vickers micro-hardness of the quenched sample upon reaching the desired temperature, T. This calculation assumes that all the austenite transformed into martensite upon quenching, and the parameters in Eq. (3.20) are representative of hardness values measured from as-received ferrite/pearlite and fully martensitic microstructures. To verify the efficacy of Eq. (3.20), Di Ciano et al. [10] determined the phase fraction of austenite formed via quantitative metallography and found both results were consistent.

3.4.2 Phenomenological Austenitization Model

Li et al. [25] recently developed a semi-empirical model, intended to estimate the volume fraction of austenite formed within 22MnB5 for intercritical and non-isothermal annealing. In their model, the intermediate stages of austenitization, consisting of nucleation, growth, and impingement, are described by a set of coupled ordinary differential equations.

The model was developed by initially assuming austenite nucleates within an idealized volume, termed the extended volume where hard impingement between growing nuclei is considered negligible [25, 44, 73]. The nucleation rate, $\dot{N}$, is described as the rate at which nuclei, of supercritical size, is formed per unit extended volume [24, 25], and follows an Arrhenius rate law as prescribed by Liu et al. [74]. Li et al.'s [24, 25] dilatometry measurements revealed that austenitization increases with temperature, but decreases with time as the heating rate increases. To account for the relationship between heating rate and nucleation, as initially incorporated by Caballero et al. [70], they propose the use of a power law

$$\dot{N} = \begin{cases} A_1\left(A + \dot{T}^{\varphi_A}\right)\exp\left(\dfrac{-Q_N}{RT(\tau)}\right), & \text{if } f_\gamma \le f_P \\ 0, & \text{if } f_\gamma > f_P \end{cases} \tag{3.21}$$

where N defines the number of nuclei formed, A_1, A, φ_A, are defined as the internal and external influencing factors, $\dot{T}$ is the applied heating rate [°C/s], Q_N defines the activation energy required for nucleation of the critical sized nuclei [J/mol], $T(\tau)$ is the instantaneous temperature [K], f_γ represents the fraction of transformed austenite, and f_p is fraction of pearlite present in the initial microstructure. Internal factors are associated with initial microstructure whereas the external

factors are related to the temperature and heating rate. Eq. (17) describes the two-step process of ferrite/pearlite transformation to austenite, identified by Roosz et al. [38] and as explained in §1.1.2. The first term expresses nucleation of austenite until complete pearlite dissolution; the second term illustrates that no further nucleation occurs, instead, existing austenite grains simply experience volumetric growth, within the remaining ferrite matrix. The volumetric growth rate, assumed to be equivalent for all nuclei at the same heating conditions, is expressed similarly as

$$\dot{v} = B_1\left(B + \dot{T}^{\varphi_B}\right)\exp\left(\frac{-Q_v}{RT(\tau)}\right) \tag{3.22}$$

where Q_v refers to the activation energy for growth [J/mol)], which is independent of temperature and time; B_1, B, and φ_B are material constant determined from dilatometry data [25]. The growth rate of the extended volume austenite, expressed as a function of the nuclei formed and their growth, is

$$\dot{f}_\gamma^{'} = N\dot{v} \tag{3.22}$$

Li et al. [25] accounted for the constrained equilibrium of carbon diffusion during intercritical annealing by defining the saturated volume fraction of austenite, $f_{\gamma s}$, as

$$f_{\gamma s} = \min\begin{cases}\dfrac{C_2}{\pi}\arctan\left(C_1\left(\dfrac{T}{T_{AS}}-1\right)\right)+C_3\\ 1\end{cases} \tag{3.24}$$

In the actual transformation process, as the austenite nuclei grow their boundaries begin to overlap, and thus the extended volume relates to the real volume via an impingement factor

$$\dot{f}_\gamma = \left(f^{m}_{\gamma s} - f^{m}_{\gamma}\right)\frac{\dot{f}_\gamma^{'}}{\left(1+\dot{f}_\gamma^{'}\right)^{n}} \tag{3.25}$$

$$m = \begin{cases}1, & f_\gamma \le f_P\\ 1-m_0, & f_\gamma > f_P\end{cases} \tag{3.26}$$

$$n = n_0\,\dot{f}_\gamma^{\varphi N} \tag{3.27}$$

where m and n are related to the initial volume fraction of pearlite and transformation related parameters, while m_o, n_o, and φ_N are constants.

All defined model parameters were calibrated using dilatometry data, summarized in **Table 5** and **Table 6**. Dilatometry data were obtained by performing three distinct heating trials on rectangular samples of 22MnB5, using a Gleeble® thermomechanical simulator. The first set of trials involved continuously heating samples to 900°C using different heating rates, ranging from 1-25°C/s; in the second trial, samples were subject to intercritical annealing with a constant heating rate of 5°C/s. In both cases, samples were soaked for 15 minutes to achieve equilibrium phase fraction austenite. Finally, a sample was continuously-heated to 1000°C and soaked for 2 minutes. The inferred fraction austenite revealed that, as the heating rate increased, the incipient fraction decreased due to lack of time available for carbon diffusion. Li et al. [25] found that the fraction austenite increased with higher temperatures and dwell times, which is consistent with work of Speich et al. [31] and Liang et al. [48].

Table 5: Calibrated constants for Eq. (3.24) [25]

C_1	C_2	C_3	T_{AS} [K]
36.0	1.2	0.475	1037

Table 6: Calibrated constants for Li et al.'s model [25]

Q_N [J/mol]	Q_v [J/mol]	$A_1 \times B_1$	A	B
1.486e5	4.05e5	2.394e6	0.8	1.0
φ_A	φ_B	m_o	n_o	φ_N
1.41	0.12	1.05	2.1	0.155

Although Li et al.'s [25] model captures the intermediate stages of austenitization, there may be certain drawbacks limiting its applicability in industrial settings. One such limitation is that their model consists of numerous adjustable parameters found by least squares fitting to dilatometry data. The large number of degrees-of-freedom makes the model susceptible to over-tuning, meaning the model fits both the physics as well as any experimental error and model error.

An over-tuned model is valid over the experimental conditions used to define the parameters, but has reduced extrapolative abilities. Further doubts casted on this model is the fact that it predicts saturated phase equilibrium obtained after thermal soaking for 15 minutes, which is significantly longer compared to the studies by [40, 72, 76, 77] and based on industrial experience. Since the dwell time does not accurately reflect conditions observed in industrial operations, it might be possible that the impingement effects are overstated compared to the actual physics. Finally, the model may lack the ability to reliably predict phase fraction austenite formed if the same steel with slightly different chemical composition is used.

3.5 Derivation of the Thermometallurgical Model

The thermometallurigcal model is derived by extending Eq. (3.3) to include the austenitization models, by defining the latent heat of austenitization term, Δh_γ. As a result, the $c_{p,eff}$ term can be replaced with the manufacturer supplied specific heat (c_p). The latent heat of austenitization couples the instantaneous fraction austenite to the temperature of the blank, thus defining the themometallurigcal model as

$$\rho_{22MnB5} c_p V_j \frac{dT_j}{d\tau} = Q_{rad,j} + Q_{conv,j} + Q_{cond,j} - \rho_{22MnB5} V_j \Delta h_\gamma \frac{df_{\gamma,j}}{d\tau} \tag{3.28}$$

where, $df_{\gamma,j}/d\tau$ is the instantaneous rate of austenite formation, expressed as a volume fraction, and c_p is the temperature dependent sensible specific heat of 22MnB5 [68]. The left hand side of Eq. (3.28) represents the sensible energy, the first term of the right hand side defines the modes of heat transfer, and the last term corresponds to the energy required for austenitization.

The crucial variable in Eq. (3.28) is the latent heat of austenitization, Δh_γ. As of now, published literature has not reported nor characterized Δh_γ for 22MnB5. Twynstra et al. [27] and Jhajj et al. [23] assumed a value 85000 J/kg [66], corresponding to the energy necessary for transformation of pure pearlitic iron to austenite. This however is an overestimation for 22MnB5 [78], which is 80%-ferrite/20%-pearlite in its as-received state. Di Ciano et al. [10] recently characterized this Δh_γ for 22MnB5 as 30000 J/kg, by applying a rule-of-mixtures.

3.6 Numerical Implementation

The thermometallurgical model was solved using two different methods: the explicit Euler scheme and using the inbuilt MATLAB function, ODE45, which evaluates ordinary differential equations using a fourth order Runge-Kutta scheme. Both methods were initialized with initial conditions of T_j = 298 K and $f_\gamma = 0$.

In the case of the explicit Euler method, a convergence study was performed which showed that a grid independent solution (*i.e.* no further improvement in the solution) was obtained with a time step of 0.15 s. However, for ODE45 a grid independent solution was obtained with a minimum time step of 1.0 s, which may be due to the versatility of the fourth-order Runge-Kutta method. In either case, the solutions were identical and ensured that the 1st law of thermodynamics was conserved (*i.e.* $Q_{cond} = Q_{rad} = Q_{conv} = dT/d\tau = df_\gamma/d\tau = 0$ at steady state). In order to verify both approaches, the numerical solutions were compared against the results published by Jhajj et al. [23] and were in good agreement. Di Ciano et al.'s [10] F1 model was modeled using the ODE45, however, Li et al.'s [25] model was evaluated using an explicit Euler scheme.

3.7 Model Uncertainty Quantification

Without exception, all hot stamping furnace models proposed to date, including those used in industry, are deterministic; they accept a single set of process parameters as input, and provide a single heating curve as output. This treatment does not capture the many uncertainties involved in the calculation, and consequently one would not expect the predicted temperature to exactly match the true thermal history of the blank. Moreover, the fact that production requirements are often probabilistic (*e.g.* obtain a blank that is 95% austenitized with 95% probability) limits the usefulness of a deterministic model since it is not possible to directly quantify how adjusting the cycle time affects the trade-off between increasing the *probability* of sufficient austenitization and productivity in terms of parts per minute.

It is hypothesized that uncertainties in the blank temperature and austenite phase fraction are dominated by uncertainties in the furnace surrounding temperatures and the metallurgical model parameters, with other uncertainty sources (e.g. the impact of the rollers, variation in the

properties and composition of 22MnB5) being secondary. Uncertainty in the furnace temperature mainly arises from the hysteresis control and in the case of lab-scale furnaces, also from non-uniform heating of the surfaces, periodic opening of the furnace door, etc. In Di Ciano et al.'s [10] model the metallurgical model uncertainties are reflected by the MVN distribution of inferred [E_A, $\log_{10}A$] parameters as described above. Unfortunately, uncertainty estimates for Li et al.'s [25] model parameters are not available.

The furnace temperature and model parameter uncertainties are propagated through the model using a Monte Carlo procedure. The thermometallurgical model is evaluated N times: each time the furnace surrounding temperatures and in the case of Di Ciano et al.'s model, a set of model parameters, are sampled from corresponding probability density functions. The resulting set of blank temperatures and austenite phase fractions are summarized by 95% highest probability density intervals derived from histograms, as described in **Appendix A**. These intervals can be interpreted to mean that they contain the "true" solution with 95% probability.

Chapter Four
Experimental and Model Validation

The candidate thermometallurgical models were assessed by comparing the predicted temperatures and austenite phase fractions to measurements carried out using two types of furnaces: a laboratory-scale muffle furnace and an industrial roller hearth furnace. The implementation of each austenitization submodel was numerically verified by comparing predicted austenite phase fractions to values reported in [10] and [25] for specified temperature curves.

4.1 Laboratory Muffle Furnace

4.1.1 Experimental Setup

Two series of annealing trials were performed using the muffle furnace: continuous heating and isothermal heating. In these measurements, some coupons were heated beyond T_{Ac3}, while other coupons were extracted at temperatures between T_{Ac1} and T_{Ac3}, and water-quenched in order to obtain information about the progress of austenitization during heating. **Table 7** outlines the two heating trials performed.

Table 7: Summary of the continuous heating trials performed to validate the thermometallurigcal model.

	Continuous Heating	Isothermal Heating	
Trial	Extraction Temperature [°C]	Extraction Temperature [°C]	Dwell Time [min]
1	760	760	5
2	820	860	1

Experiments were performed using 2 mm thick, 130mm × 30 mm Al-Si coated 22MnB5 coupons made from a sheet of Usibor® 1500AS. This is one of the thickest gauges used for hot stamping

and represents a "worst case scenario". The experiment is schematically shown in **Figure 22,** whereas the equipment used is discussed in **Appendix B**. Measurements were carried out on single-gauged coupons and double-gauge coupon "sandwiches", formed by spot-welding two single-gauge coupons at their corners, to emulate patched blanks. Each trial consisted of a single-gauge and double-gauge coupon heated side-by-side. A platform constructed from a silica-based ceramic (RSLE 57, Zicar Inc.) was used to consistently locate the coupons within the furnace and minimize conduction between the platform and samples. Three K-type thermocouples were spot-welded along the centerline of each coupon: one at the center, while the other two were located 20 mm from each end. Three trials were carried out per test to verify if the assumption that the patch and unpatched region as being thermally-lumped, as defined in in §3.1, was valid. Each thermocouple was insulated using a silica-based sheathing to prevent bare wires from creating intermittent contact and reduce susceptibility to errors caused by wire heating. The lead of each wire was individually welded to form an intrinsic junction, rather than a bead that is subsequently welded onto the samples for greater structural integrity of the weld. An additional unshielded thermocouple was used to monitor the ambient temperature inside the furnace, which varied by ±5°C from the furnace set-point temperature of 900°C during the course of the measurements.

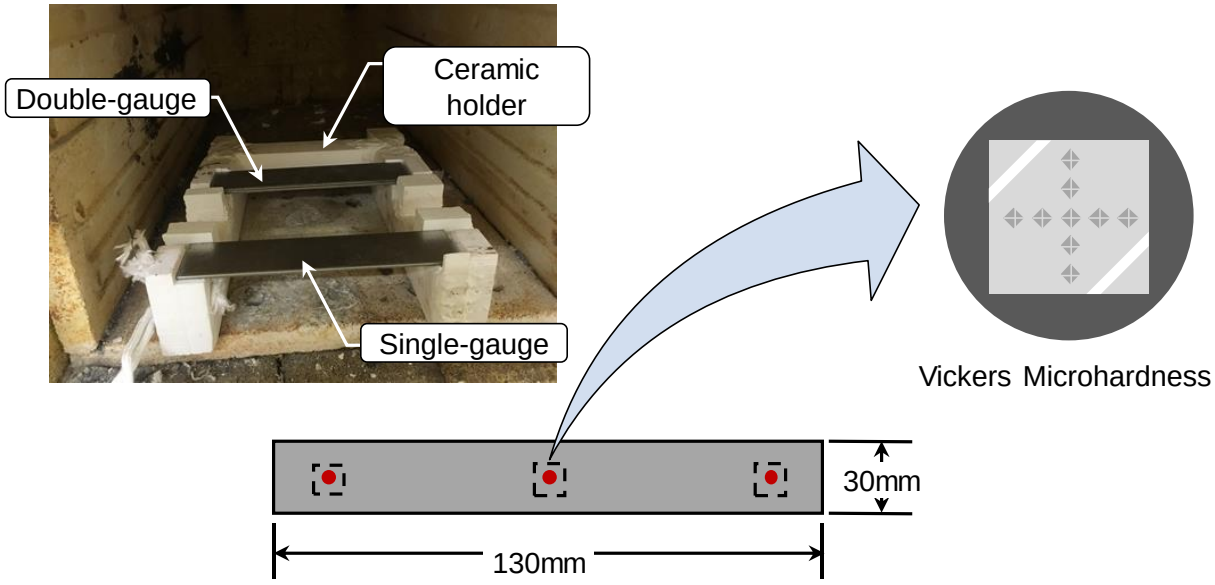

Figure 22: Muffle furnace experimental set up. Red dots indicate thermocouple weld sites, while squared dashed regions are regions used for micro-hardness and metallography.

Prior to performing each experiment, the muffle furnace was thermally-soaked for two hours to achieve steady state (or nearly isothermal conditions). Once the furnace reached equilibrium the furnace door was opened to insert the coupons and then closed, a process that took under 20 seconds. Upon reaching the desired patch temperature the coupons were extracted and quenched in a cold water bath to ensure complete martensitic transformation. The quenched samples were cut into 10 mm x 10 mm sections centered about each thermocouple location, mounted, polished with 1 μm diamond paste, and etched with 2% Nital solution. The 2% Nital etchant dissolves the grain boundaries revealing different microstructures formed during the interrupted heating cycles, which are visualized with micrographs, obtained via optical microscopy. Microhardness measurements were then carried out on each mounted sample using a Vickers indenter (Vickers 402 MVD, Wolpert Wilson Instruments) and a 1 kg load. Microhardness measurements were taken in an 11 × 11 cruciform pattern with a spacing of 1 mm. The volume fraction of austenite formed during heating is inferred using Eq. (3.20), following the procedure described by Di Ciano et al. [10] and ASTM A1033-10 [79].

4.1.2 Results and Discussion

Uncertainty associated with the thermocouples measurements is within ±0.9°C of the actual measured value as discussed in **Appendix A**. The temperature profiles obtained for the single- and double-gauge coupons are shown in **Figure 23**, for the heating trials defined in **Table 7**. The heating curve for both coupons extracted at different temperatures were nearly identical (from the time they are inserted into the furnace until the time they are extracted) and thus only thermocouple measurements for the 820°C trial are shown for clarity. The thermal history of the heated coupons indicates that the single-gauge coupon is heated significantly faster compared to the double-gauge sample, due to the lowered thermal inertia of the thinner sample and thus it is also austenitized earlier than the thicker coupon. All thermocouple measurements are similar which supports the thermally-lumped assumption made in §3.1. A slight variation is observed between the center and edge temperatures of the single-gauge coupon, which may indicate a cold spot within the furnace during heating, since this location was closest to the furnace door. Close examination of the single-gauge temperature profile reveals the expected temperature drop in heating rate at 575°C corresponding to the drop in radiative properties in **Figure 20**. This is

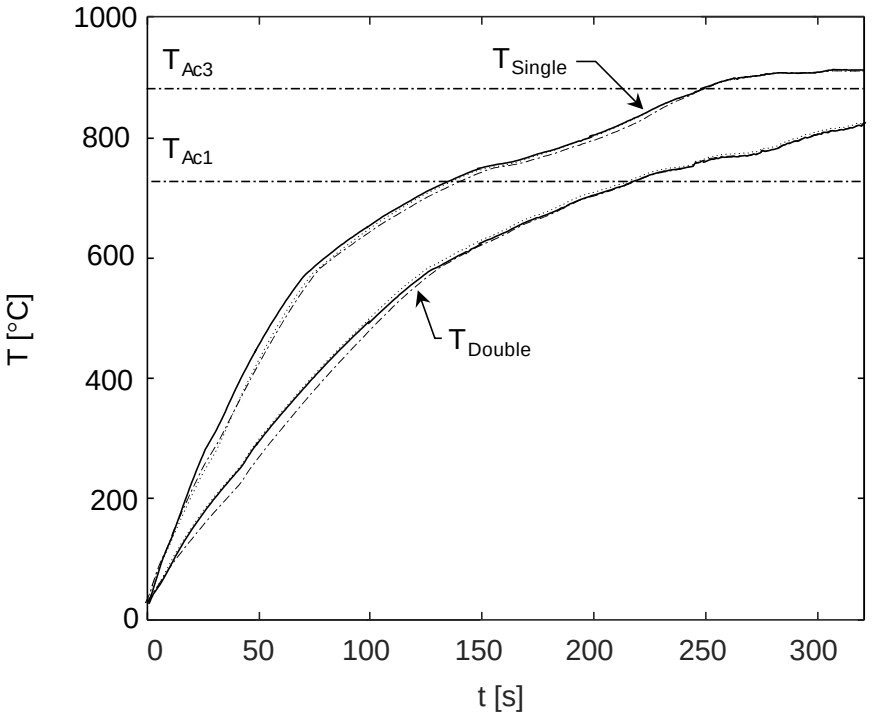

Figure 23: Thermocouple measurements of the single- and double-gauge coupons heated within the muffle furnace, upon extraction at 760°C and 820°C. The solid line represents the centrally located thermocouple, the dashed and dotted lines represent the measuerments from the edges of the samples.

followed by a larger inflection near 730°C corresponding to the onset of austenitization (T_{Ac1}), which was also observed by [10, 23].

In modelling the coupon heating, the muffle furnace surfaces were treated as isothermal, having a probabilistic temperature that obeys a uniform distribution with an interval of ±20°C based on measured fluctuations in furnace wall temperatures at steady state described in Chapter 2. The predicted temperature curves obtained by sampling this distribution, using Di Ciano et al.'s [10] first-order austenitization submodel are shown in **Figure 24**, along with the thermocouple measurements for a single trial. The uncertainty quantification described in §3.7 was used to construct 95% credibility intervals. **Figure 24** shows that the thermocouple measurements for the double-gauge coupon lies within the 95% credibility interval although the measured single-gauge coupon temperatures lie below the predicted value. It is possible that the differences observed may be a result of a model error (*e.g.* radiative boundary conditions) instead of an instrumentation issue

as the simulated and measured temperatures converge to the furnace set point. The fact that the modeled and measured heating rates are slightly different below 575°C (the Al-Si melting temperature), could indicate an error in the radiative properties or the assumed specific heat of 22MnB5.

The thermometallurgical model captures the variation in the temperature associated with austenitization, although the measured temperature deviation is less pronounced for the double-gauge coupon. The model predicts austenitization initiation at $T_{Ac1} \cong 730°C$ and completion upon reaching $T_{Ac3} \cong 880°C$. The modeled results and measurements indicate that most of the austenitization occurs near T_{Ac1}, since the inflection is the greatest and gradually decreases with time, as reported by [10, 23]. **Figure 24** also shows that the latent energy is not uniformly distributed between T_{Ac1} and T_{Ac3}, as assumed by Twynstra et al. [27], as the inflection would have been difficult to resolve (*i.e.* the inflection would be significantly smoother and less pronounced).

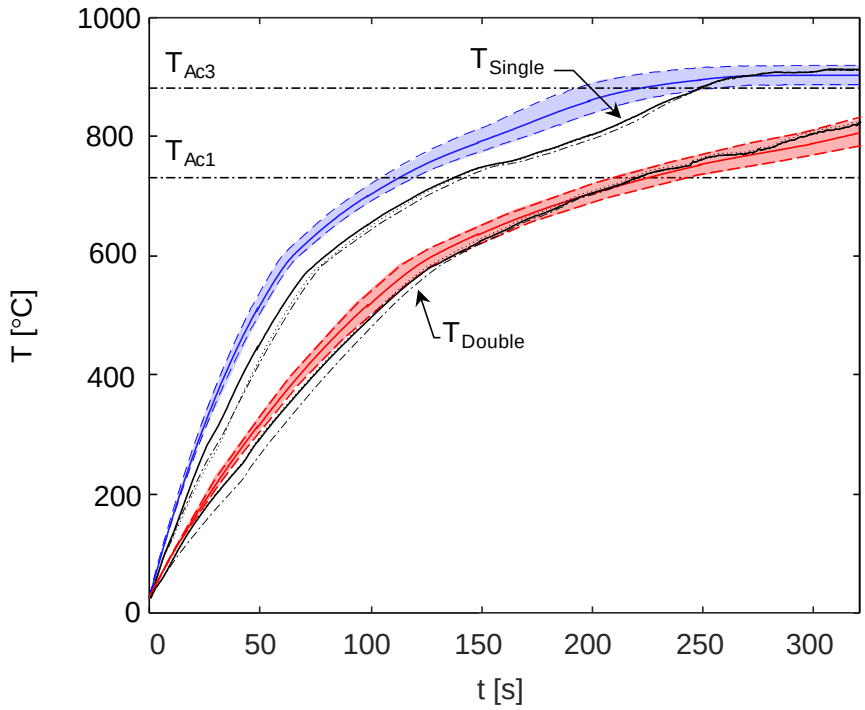

Figure 24: Temperature distribution of muffle furnace heated coupons compared against modeled temperatures. Solid, dashed, and dotted lines represent the three thermocouples shown in Figure 22. Blue and red lines are the most probable temperature distributions and shaded regions represent 95% credibility intervals.

The corresponding modeled austenite phase fractions are plotted in **Figure 25**, along with box plots that summarize the inferred values from the 63 microhardness measurements. The "whiskers" identify the upper and lower bounds of the inferred austenite phase fraction; the horizontal line in the box represents the median value, and the upper and lower surfaces of the box are the 75th and 25th quartiles respectively. The most probable model temperatures for both cases are also shown, with credibility intervals excluded for clarity.

Figure 26 shows the micrographs of the as-received 22MnB5 microstructure, double-gauged coupons extracted at 760°C and 820°C, corresponding to the box plots in **Figure 25**, and a fully-austenitized single-gauge coupon. The as-received microstructure consists of ferrite grains (bright) and pearlite bands (dark due to presence of carbon). By the time the steel reaches 760°C all the pearlite has transformed into ferrite and austenite, the latter phase converting into martensite during quenching. Upon reaching 820°C, most of the ferrite grains have transformed and the entire

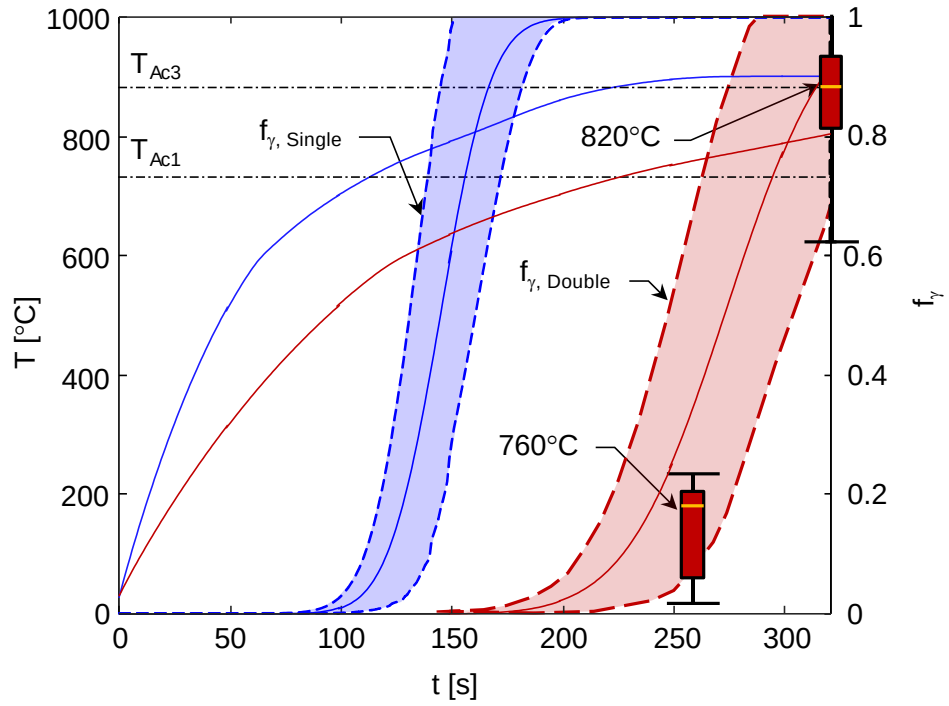

Figure 25: Comparison of simulated austenite phase fraction versus microhardness inferred values. Blue and red lines corresponds to the single- and double-gauge coupons, respectively. Box plots represent the range of the hardness-inferred f_γ, which are contained within the 95% credibility intervals, indicated by the shaded regions.

microstructure consists almost entirely of martensite. The similarity between the microstructures shown in **Figure 26 (c)** and **(d)** suggests that austenitization is largely completed below T_{Ac3}, which is consistent with earlier observations [10, 23].

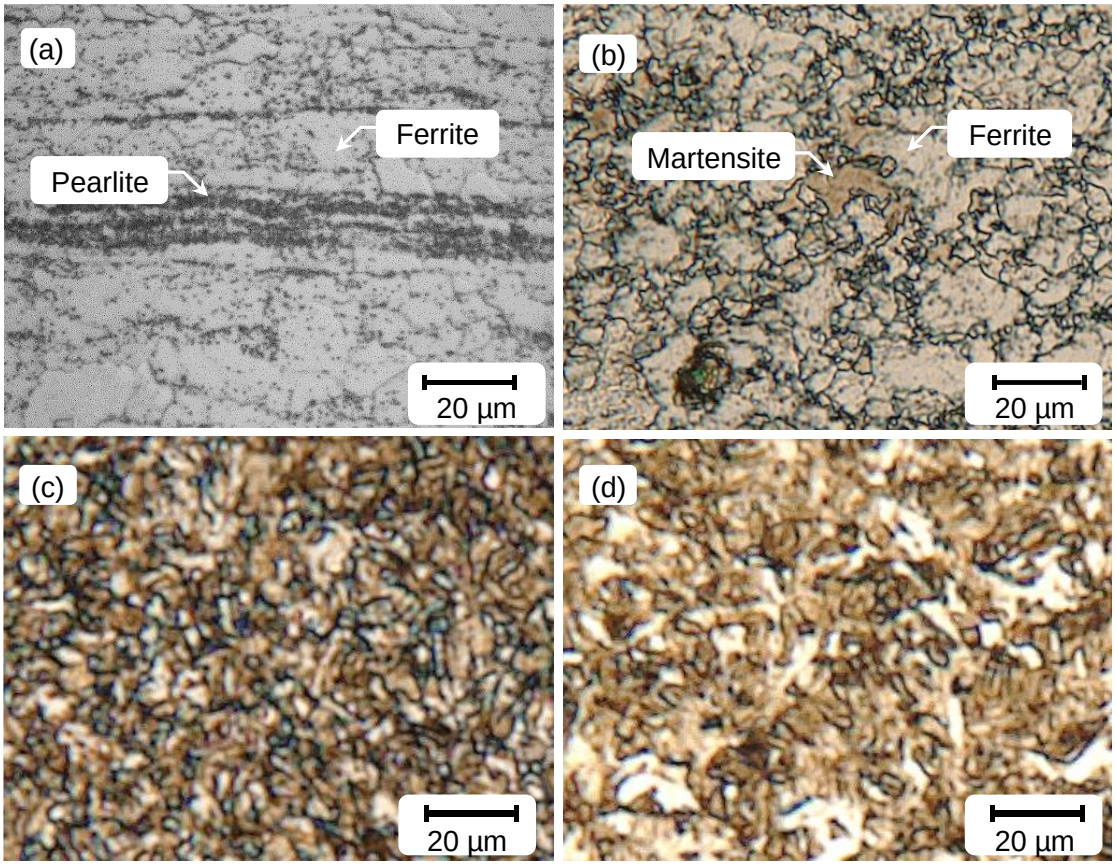

Figure 26: Optical micrographs of the 22MnB5 microstructure, showing (a) as-received ferrite/pearlite microstructure; and coupons heated to (b) 760°C; (c) 820°C; and (d) 900°C, and then quenched in a cold water bath. The microstructure in (b) is a mix of ferrite and martensite, indicating incomplete austenitization, while (d) shows a purely martensitic microstructure, indicating full austenitization. Coupons (b-c) are double-gauged, and correspond to the hardness-inferred austenite fractions shown in Figure 25.

Figure 27 compares the temperature and austenite phase fraction predicted using Li et al.'s [25] phenomenological model with the measured values. As mentioned previously, Li et al. do not report uncertainties for their model parameters, so it is not possible to compute credibility intervals. In contrast to the F1 model [10], Li et al.'s model shows a significant departure between the measured and modeled austenite phase fractions. In particular, their model predicts a much

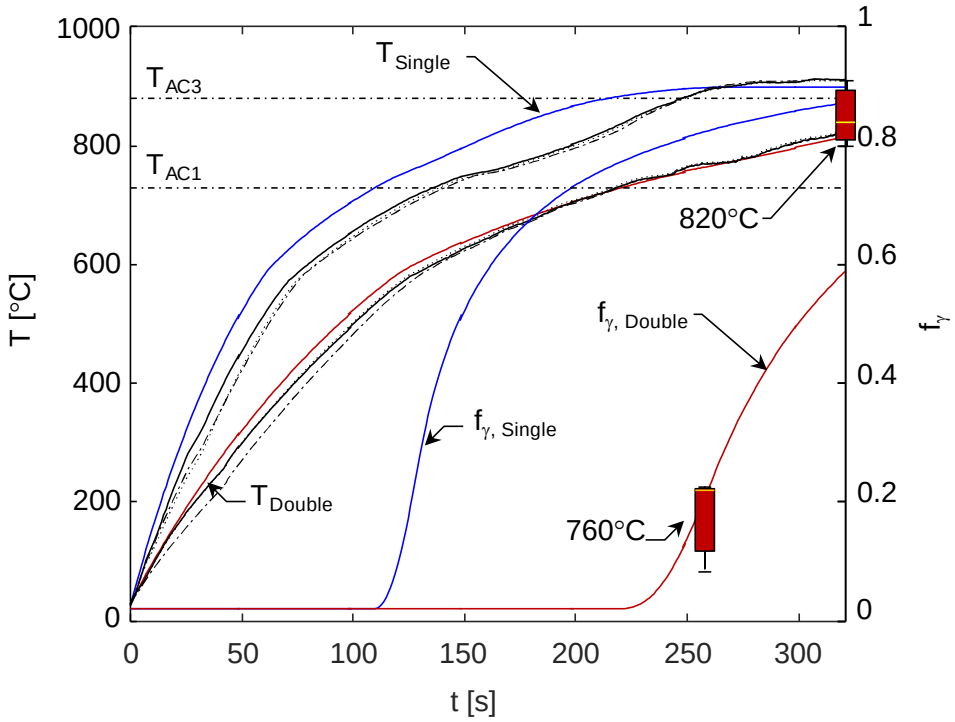

Figure 27: Comparison of simulated austenite phase fraction versus microhardness inferred values using Li et al.'s model [25]. Blue and red lines corresponds to the single- and double-gauge coupons, respectively. Box plots represent the range of the hardness-inferred f_γ.

slower rate of austenitization for both samples and that the single-gauge coupons remains only partially austenitized although it has exceeded T_{Ac3}, for an extended period of time. This result is contrary to other measurements presented in the literature as well as industrial experience, which shows that austenitization should be nearly complete once a blank reaches T_{Ac3} at heating rates typical of furnaces.

The discrepancy may be due to over-tuning in Li et al.'s [25] model, as described in §3.4. Specifically, it seems likely that the impingement effects may overestimate true physical effects. To verify this hypothesis two further muffle furnace experiments were performed with the furnace set to 780°C and 860°C. **Figure 28** shows that, for these isothermal cases, the detailed kinetics model closely estimates the phase fraction formed, although there still is a discrepancy at higher temperatures, which may indicate an issue with the impingement correction.

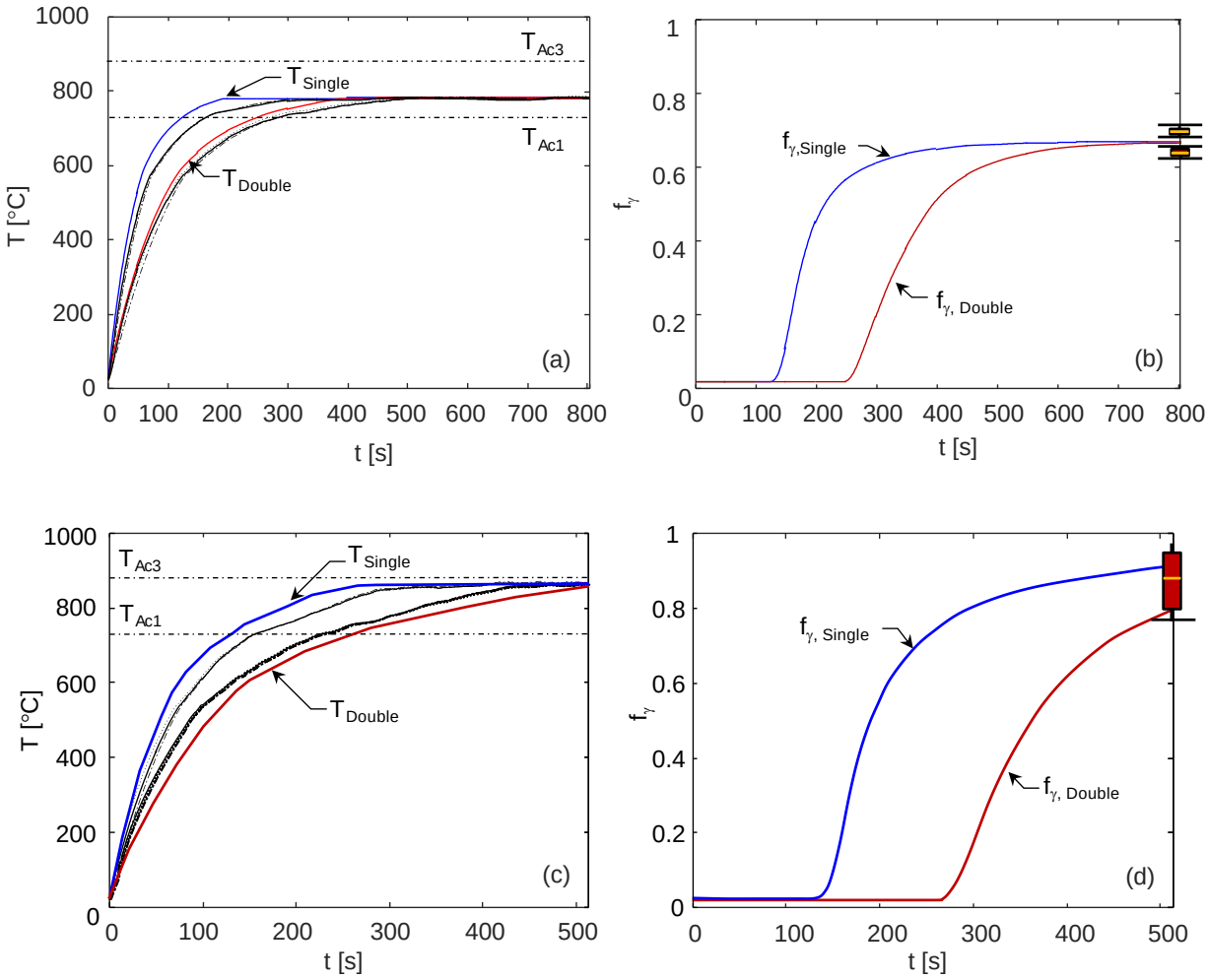

Figure 28: Intercritical annealing experiment performed to validate proposed model with Li et al.'s [25] constitutive model. In (a, b) the furnace temperature is set to 760°C, 5 min soak and (c, d) the furnace temperature is set to 860°C, 1 min soak. (Box plots and dashed lines correspond to experimental data.)

4.2 Roller Hearth Furnace

4.2.1 Experimental Setup

Further measurements were carried out using the roller hearth furnace described in Chapter 2, in order to validate the model in an industrial setting. The furnace used was 33 meters long, and consists of 14 independently controlled heating zones.

The industrial heating trial involved using an instrumented Usibor® 1500AS B-Pillar with a blank and patch thickness of 1.5 mm and 2 mm, respectively, with a roller speed of 70 mm/s. On s ome of the blanks, two K-type thermocouples were spot-welded onto the patched blank: one on the unpatched area far away from the patch (Region "A") and one on the patch (Region "C"). Similar to the muffle furnace trials, the thermocouples leads were insulated using silica-based sheathing and individually welded to form intrinsic junctions on the blank. Other blanks were not instrumented; as these blanks left the furnace, they were transferred to the forming/quenching die, after which micro-hardness measurements were made to infer the fraction austenite formed (instrumented blanks cannot be formed and quenched). All experiments were performed under the supervision of Formet Industry personnel.

4.2.2 Results and Discussion

Since the muffle furnace trials indicated that Li et al.'s [25] model did not yield reliable results, all subsequent analysis is done using the F1 model [10]. The predicted and measured temperature profiles are shown in **Figure 29** along with the 95% confidence intervals, calculated assuming the temperatures are mutually-independent and obey uniform distributions over the hysteresis control limit. The measured temperatures are close to, yet lie slightly outside of the 95% credibility intervals. The differences observed between the simulated and measured temperatures may be attributed to discrepancies in the applied boundary conditions, which requires further analysis. Unlike the batch furnace measurements, it is not possible to extract the blanks at intermediate heating times, nor is it possible to engineer controlled scenarios that will produce incomplete austenitization, but the model accurately predicts the onset and completion of austenitization close to the T_{Ac1} and T_{Ac3} temperatures. The results also show that the majority of the austenitization occurs near T_{Ac1}, which is consistent with the muffle furnace trials.

4.3 Experimental and Validation Summary

The candidate thermometallurgical models were assessed by comparing simulated temperatures and austenite phase fractions with thermocouple and hardness measurements made on instrumented single- and double-gauge coupons within a laboratory muffle furnace, and patched

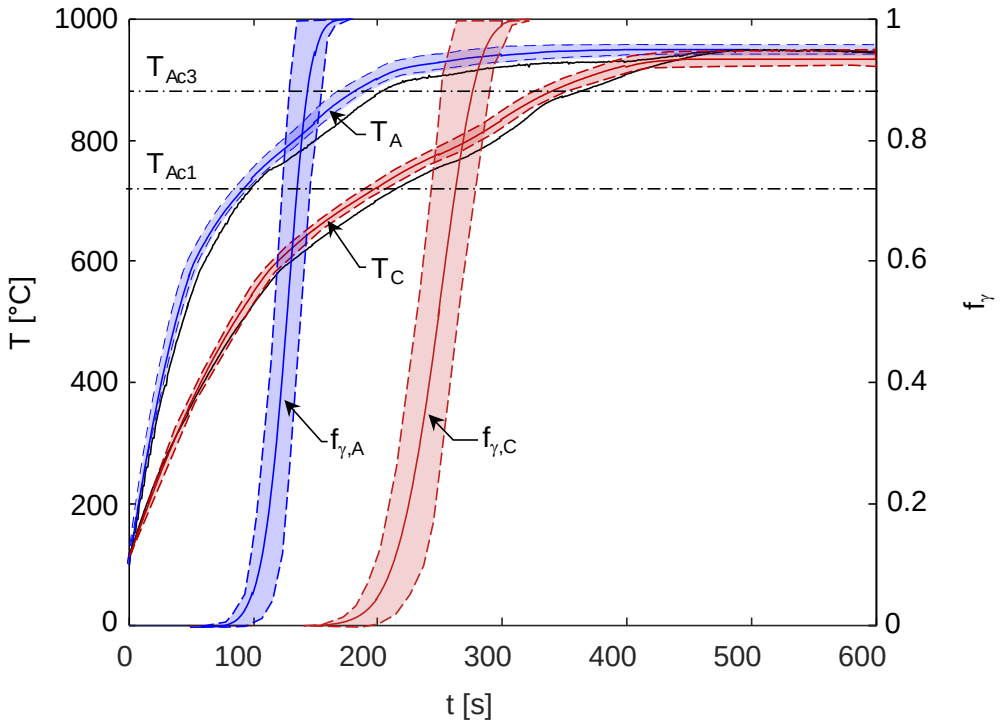

Figure 29: Industrial roller hearth trial conducted on a patched B-pillar blank. Both unpatched and patched regions completely austenitized and is accurately predicted by the proposed model.

blanks heated in an industrial roller hearth furnace. Thermocouple measurements obtained from the lab -scale furnace experiments support the assumption the unpatched and patched regions may be treated as thermally-lumped.

The thermocouple and hardness measurements obtained from the trials are contained within the 95% confidence interval, using the first-order submodel [10]. The first-order submodel indicates that the majority of austenitization completes near T_{Ac1}, supported by the sharp inflection observed in the thermocouple measurements at ~730°C, which gradually decreases and the sample micrographs (consistent with the non-linear distribution of the latent heat reported by Di Ciano et al. [10] and Jhajj et al. [23]). The phenomenological submodel [25], however, consistently under-predicted the austenite phase fraction and failed to show complete austenitization for coupons surpassing T_{Ac3}. Two reasons for the observed differences may be due to parameter over-tuning, thereby causing experimental and model errors to be incorporated within the submodel and an over-estimation of impingement effects.

Since the first-order submodel was generally consistent with the experimental observations, the following analysis will focus on applying this model to optimize process parameters of a roller hearth furnace in order to maximize production efficient while ensuring complete batch austenitization.

Chapter Five
Furnace Design Optimization

The validated thermometallurgical model is now used for design optimization of the roller hearth furnace. The optimization procedure relates blank heating and austenitization to the furnace parameters: zone temperatures, roller speed, and the spacing between sequential batches on the rollers (cycle length). The aim of the design optimization is to minimize the process cycle time, while ensuring that the functional objectives and constraints are satisfied. Two optimization techniques were used: a gradient-based interior point algorithm with a logarithmic barrier function, and a hybrid approach that combines a metaheuristic (genetic algorithm) with the gradient-based interior point method. The design optimization scheme is assessed by using the thermometallurgical model with the F1 model [10], with particular focus on unpatched blanks.

5.1 Design Optimization

Optimization is the process of transforming a design problem into a multivariate minimization problem by defining a vector of design parameters, **x**, that specify the design configuration and an objective function, $F(\mathbf{x})$, that quantifies the "goodness" of the design so that the objective function is minimized by the optimal design outcome. The set of parameters that minimizes the objective function, $\mathbf{x}^* = \text{argmin}_x[F(\mathbf{x})]$, specifies the optimal design. Constraints can be further imposed on **x** to ensure that the design complies with the functional requirements and can be implemented in an industrial setting.

Design optimization has been widely used in furnace-based heating processes for a range of metallurgical applications [54-60]. Specific application of optimization in HFDQ have been more limited. Twynstra et al. [27] identified the power settings for electrical panel heaters that provided the uniform irradiation of Usibor® 1500AS blanks in a batch furnace. Tonne et al. [61] performed a multi-objective optimization on a roller hearth furnace to minimize the energy consumption and process cycle time.

5.2 Definition of the Design Optimization Problem

A 12-zone roller hearth furnace, similar to the one defined in Chapter 2, is the prime focus for design optimization. In this analysis, the optimization is performed to identify process parameters solely for the austenitization of unpatched blanks.

The first step is to identify the objective function, design variables, and functional constraints. The objective function to be minimized is the cycle time, which is defined as the interval between batches leaving the furnace. There are fourteen design parameters to be optimized, summarized in **Figure 30**, x_1-x_{12}, the cycle length, x_{13}, comprised of the batch and gap length, and the roller speed, x_{14}. The cycle time is expressed as a function of the cycle length and roller speed by

$$F(x) = F(x_{13}, x_{14}) = x_{13}/x_{14} \tag{5.1}$$

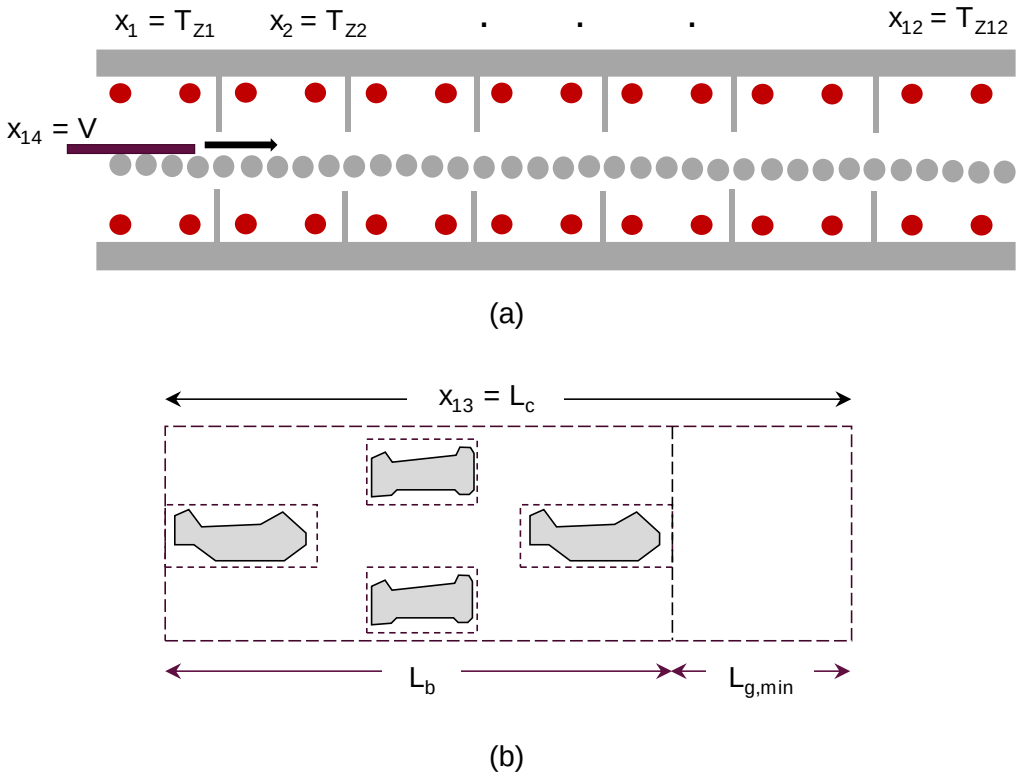

Figure 30: Schematic of the roller hearth furnace optimization problem. (a) zone temperatures and blank velocity; (b) blank load and cycle length

In order to ensure the functional requirements of the heat treatment step, including austenitization of batches, operation within specified burner ratings, and formation of the intermetallic layer, are fulfilled, several process constraints are introduced. The imposed functional constraints are summarized in **Table 8**, and discussed in detail below.

Table 8: Process constraints for furnace optimization

Linear	$c_{L1\text{-}12}$	$T_{z,i,min} \leq x_i \leq T_{z,i,max}$, i=1,…,12	Max/min zone temperatures
	c_{L13}	x_{13}-$L_b \geq L_{g,\,min}$	Min batch spacing
Nonlinear	$c_{N1\text{-}12}$	Eq. (5.2)	Zone burner capacity
	c_{N13}	$t_{T\geq 900°C} \geq 30$ s	Implicit austenitization
	c_{N13a}	$f_{\gamma,exit} \geq 0.95$	Explicit modeled austenitization
	c_{N14}	$T_{t=60s} \leq 700°C$	Layer growth
	c_{N15}	$T_{exit} \leq 950°C$	Burning of Al-Si coating

Two linear constraints have been specified to enforce a minimum gap length between sequential loading of batches and bounds for the zone temperatures. A series of nonlinear constraints have also been defined. The initial nonlinear constraint ensures that the heating requirements for each zone do not exceed the manufacturer specified burner rating

$$\frac{1}{\eta_{th}}\left\{\dot{m}_b\left[c_p\left(T_{b,i+1}-T_{b,i}\right)+\Delta h_\gamma\left(f_{\gamma,i+1}-f_{\gamma,i}\right)\right]+\dot{Q}_{loss,i}\right\} \leq \dot{Q}_{bunrner,\,i} \tag{5.2}$$

where η_{th} is the thermal efficiency of the radiant tubes (approximately ~70%), $\dot{m}_b$ is the mass flow rate of the blanks through the furnace, c_p is the specific heat, T_b is the blank temperature, f_γ is the austenite phase fraction, indices i and i+1 denote the state of the blank at the beginning and end of each zone, $\dot{Q}_{loss,i}$ accounts for the loss of heat through the furnace walls and door, summarized in **Table 9**, and $\dot{Q}_{burner,i}$ defines the burner capacity for each zone, specified in **Table 10**.

Table 9: Heat loss through the walls in each zone of the roller hearth furnace, in units of [kW]

i	1	2	3	4	5	6	7	8	9	10	11	12
$\dot{Q}_{loss,i}$	36	8	8	8	9	18	18	18	18	18	18	36

Table 10: Burner capacity for each zone of the roller hearth furnace, in units of [kW]

i	1	2	3	4	5	6	7	8	9	10	11	12
$\dot{Q}_{burner,i}$	320	240	180	240	180	180	120	180	180	60	60	60

Constraints to ensure complete blank austenitization and growth of the intermetallic layer have been enforced, serving as surrogate constraints since these properties cannot be measured directly during the heating process. The former is an industrial heuristic, which is intended to ensure that the blanks are completely austenitized if they are soaked for 30 s beyond 900°C [1, 9, 80]. The latter constraint was assumed to be prevent melting of the Al-Si layer, if the heating rate is maintained below 12 °C/s (or blank temperature below 700°C within the first 60 s of heating) [50, 49]. However, Grauer et al. [49] and Veit et al. [81], cited by Liang et al. [48], have shown that liquefaction is unavoidable under low heating conditions; rather this constraint corresponds to preventing excessive layer growth as mentioned in the original steel patent [49]. An alternative, explicit, austenite constraint has also been specified ensuring that each batch attains at least 95% austenitization upon exiting. The final constraint enforces that the blank temperature remain below 950°C to prevent burning of the eutectic coating.

5.3 Constrained Multivariate Minimization

At this stage, the design problem has been recasted as a constrained multivariate minimization problem, which can now be solved numerically. Multivariate minimization algorithms can be categorized as either gradient-based and metaheuristic.

5.3.1 Gradient-based Interior Point Method

Commonly used gradient-based algorithms include Newton's method, conjugate gradient (CG) method, and trust-region algorithm [82, 83]. One common characteristic amongst these algorithms is that they use information about the derivatives to determine iterates that improve the objective function.

Gradient-based algorithms are generally defined by the update scheme

$$x_{k+1} = x_k + \alpha_k p_k \tag{5.3}$$

where x_{k+1} is the new iterate, x_k is the current iterate, p_k is the search direction, α_k is a positive scalar step size for the algorithm to take in the direction p_k. The difference between the various algorithms is with regards to how the search direction p_k is computed, such that the new iterate, $x_{k+1} = x_k + \alpha_k p_k$, ensures $f(x_{k+1}) < f(x_k)$ [82, 83]. This procedure continues until a termination criteria is met or the algorithm reaches a boundary of the feasible region, as illustrated in **Figure 31**.

In Newton's method, a second-order technique, p_k is derived by taking a second-order Taylor series such that $f(x_k + p_k)$ is approximated by a quadratic model,

$$f(x_k + p_k) \approx f(x_k) + p^T \nabla f(x_k) + \frac{1}{2} p^T \nabla^2 f(x_k) p_k \tag{5.4}$$

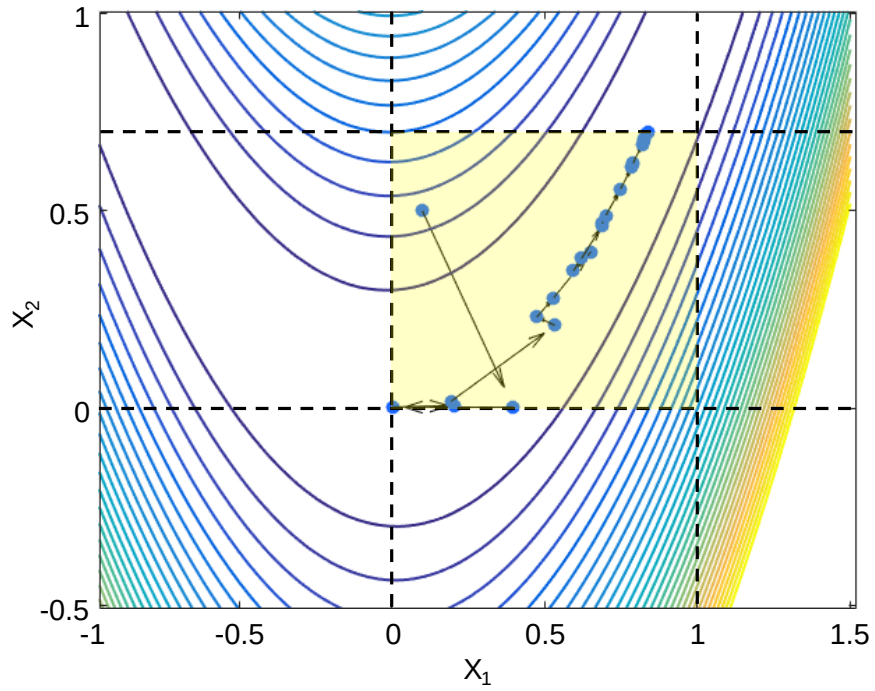

Figure 31: Path followed by a gradient-based method, to identify the bounded local minimum of the Rosenbrock function. Circles represent the "best" iterates identified; arrows define the search direction (p_k); step length (α_k) is defined by the arrow lengths. Iterates are bounded within the feasible regions, represented by the yellow region, defined by the problem constraints, represented by the dashed lines.

Taking the derivative of the quadratic model with respect to p_k and setting it equal to zero yields the search direction

$$p_k = \frac{-\nabla f(x_k)}{\nabla^2 f(x_k)} \tag{5.5}$$

where $\nabla f(x_k)$ and $\nabla^2 f(x_k)$ are the gradient and Hessian respectively. This method requires computation of the Hessian at each iteration, which is computationally expensive to evaluate. Fletcher and Reeves [84] modified the linear CG method, which requires exactly n steps to reach the minimum, for nonlinear cases. In their modification, a series of search directions that are mutually conjugate are defined to avoid "zig-zagging" steps that may occur due to a changing Hessian. Thus, the search direction depends on $\nabla f(x_k)$ and the previous search direction, p_{k-1}, such that

$$p_k = -\nabla f(x_k) + \beta_k p_{k-1} \tag{5.6}$$

where β_k is

$$\beta_k = \frac{\nabla f(x_k)^T \nabla f(x_k)}{\nabla f(x_{k-1})^T \nabla f(x_{k-1})} \tag{5.7}$$

Therefore, the CG method requires information about the last two iterations. Trust-region methods approximate the objective function using the quadratic model defined in Eq. (5.3), similar to Newton's method. Trust-region methods define a spherical region around x_k, with radius Δ_k, where the algorithm "trusts" the quadratic model within a limited neighborhood if and only if [83]

$$\|p\|_2 \leq \Delta_k \tag{5.8}$$

where p is the search direction and Δ_k is the region radius at the k^{th} iteration. At each iteration of the algorithm, the step direction is determined by evaluating a minimization subproblem

$$\begin{aligned} &\min_p \; f(x_k) + \nabla f(x_k) p^T + \frac{1}{2} p^T \nabla^2 f(x_k) p \\ &s.t. \quad \|p\|_2 \leq \Delta_k \end{aligned} \tag{5.9}$$

If the subproblem violates the constraint, Newton's method cannot be applied, thus a scalar $\widehat{\lambda}$ must be determined so that

$$\|p\|_2 = \left\| \left(\nabla^2 f(x_k) + \widehat{\lambda} \mathrm{I} \right)^{-1} \nabla f(x_k) \right\|_2 = \Delta_k \tag{5.10}$$

If the step direction is not acceptable, the radius of the sphere is decreased to find a new minimizer, and in general, the direction and step change with the size of the trust-region [77, 78].

Nonlinear optimization problems are challenging to solve, when inequality constraints are present, due to the inability to identify which constraints are active (*i.e.* $c_{\mathcal{I}}(x) \geq 0 \rightarrow c_{\mathcal{I}}(x) = 0$) at the solution [82, 83]. One method to resolve this challenge involves solving a sequence of subproblems by changing which constraints would be active at the optimum. The issue with this approach is that there are $2^{|\mathcal{I}|}$ combinations, where $|\mathcal{I}|$ is the number of inequality constraints; thus the problem becomes combinatorially difficult [83]. An alternative approach for handling inequalities, which is popular for nonlinear programming is the interior point method [85].

The interior point method, also called the barrier method is an algorithm that ensures strict feasibility by forcing iterates to be far from the boundary of the feasible region [82, 86]. The logarithmic and inverse functions are two types of barrier functions widely used in practice

$$\phi(\mathrm{x}) = -\mu \sum_{j=1}^{m} \log\left(c_{Nj}(\mathrm{x}) \right) \tag{5.11}$$

$$\phi(\mathrm{x}) = -\mu \sum_{j=1}^{m} \frac{1}{c_{Nj}(x)} \tag{5.12}$$

where μ is the weight applied to the barrier function, a unitless, positive scalar quantity, whereas $c_{Nj}(\mathbf{x}) \geq 0$ are the nonlinear constraints. As the iterate approaches the boundary of any constraint, the barrier term approaches infinity ($\phi \rightarrow \infty$ as $c_{Nj} \rightarrow 0$). The interior point method is coupled with the search direction algorithms mentioned above, such as Newton's method and CG method. The nonlinear constraints are redefined in terms of the weighted logarithmic barrier function and added to the objective function such that the constrained problem can be reformulated as,

$$\min_{x} \ \beta(\mathbf{x}, \mu) = f(x) - \mu \sum_{j=1}^{n} \log\left[c_{\mathcal{I}\, j}(\mathbf{x}) \right]$$
$$s.t. \ \ c_{\mathcal{E}}(x) = 0, \quad \mathcal{E} = 1, \ldots, m \tag{5.13}$$

All the gradient-based algorithms mentioned above must satisfy a set of first-order sufficient optimality conditions, called the Karush-Kuhn-Tucker (KKT) conditions, in order to ensure a local or global minimum has been identified. The KKT conditions for an optimization problem with only inequality constraints are [82, 87]:

$$\nabla_x \mathcal{L}\left(x^*, \xi^*\right) = 0 \Rightarrow \nabla_x f(x^*) - \sum_{j=1}^{n} \xi_j^* c_{Nj}(x^*) = 0$$
$$\xi^* \geq 0 \tag{5.14}$$
$$\xi^* c_{\mathcal{I}}(x^*) = 0$$

where $\nabla_x \mathcal{L}(x^*, \xi^*)$ is the gradient of the Lagrange function at the optimal solution and ξ^* is the vector of Lagrange multipliers, equal to the number of inequality constraints, at the optimal, for the constraints. The first condition ensures that a local minimum has been identified; the second condition ensures that the Lagrange multipliers are non-negative values; and the final condition indicates whether each constraint is active or inactive, if constraint j is inactive $\xi_j^* = 0$. The Lagrange function provides ease of identifying function minima without having to work with constraints parametrically. The Lagrange multipliers, also called the "shadow prices" or "dual variables", provide insight about the sensitivity of the optimal solution, **x***, if the constraints are slightly perturbed [82, 87].

The predominantly used barrier function in practice is the logarithmic function, defined in Eq. (5.11). In the interior point method, the nonlinear constraints are redefined in terms of weighted logarithmic barrier function, added to the objective, which penalizes the objective function if any constraints are violated. Thus, the multivariate constrained minimization problem in §5.2 can thus be expressed as,

$$\min_{\mathbf{x}} \beta(\mathbf{x}, \mu) = \frac{x_{13}}{x_{14}} - \mu \sum_{j=1}^{15} \log\left[c_{\mathrm{N}j}(\mathbf{x}) \right]$$
$$s.t. \quad x_{lb} \le x_i \le x_{ub}, i \in [1,12] \qquad (5.15)$$
$$x_{13} - L_b \ge L_{g,\min}$$

where the variables are the same as described previously. The weighted parameter, μ, is determined by solving a sequence of subproblems with decreasing values of μ until convergence. As $\mu \to 0$, the barrier effect diminishes, thus allowing iterates to move closer to the constraint bounds yielding an infinite penalty (since $c_{Nj} \to 0$), as shown in **Figure 32**. In practice, a sequence of subproblems are solved because defining a small μ makes the problem too difficult to solve, as the barrier function will be close to infinite penalty; however, by gradually decreasing μ and using the current solution as the initial seed for the next evaluation makes the computation easier [82, 87], however, with modern computational efficiency this is not an issue. For this particular problem,

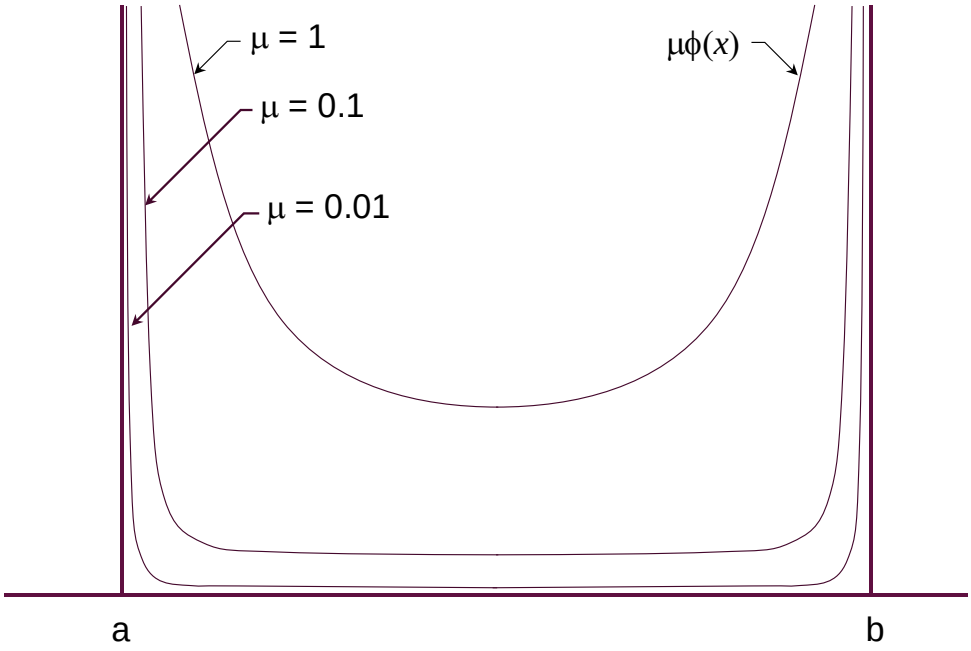

Figure 32: Influence of the barrier term for a one-dimensional bounded problem. As $\mu \to 0$ the effect of the barrier function diminishes, thus allowing the solver to identify optimal iterates closer to the boundary of the feasible region, defined here as, $a \le x \le b$.

$\mu = 10^{-3}$ and the nonlinear programming problem was solved in MATLAB^{TM} using the inbuilt *fmincon* function with the interior point method [88].

5.3.2 Metaheuristics

Metaheuristics refers to going beyond the use of heuristics (*i.e.* trial and error) to efficiently explore the search space, in order to find a solution that is better than what is currently available [89]. These class of solvers randomly sample the search domain in order to identify a good approximation of the global minimum, hence making them stochastic in nature [90, 91, 92]. Two key features of metaheuristic algorithms are diversification and intensification. The former refers to creating a diverse solution set for efficient exploration of the search space, achieved by random sampling of the domain, whereas the latter describes focusing the search within a local region according to solver heuristics knowing the solution lies within a specific area [89]. It is therefore essential to strike a balance between the two in order to efficiently determine high-quality regions within the domain space [89]. Several algorithms belong within this class of optimization methods, including, genetic algorithms (GA), simulated annealing (SA), and particle swarming (PS). The mentioned algorithms vary based on the philosophy of the metaheuristic used. For instance, the GA is based on the concepts of survival of the fittest (Darwinian evolution), simulated annealing is based on the process of metal annealing, and particle swarming is based on trajectory of individual birds flying in flocks [93].

Metaheuristics are classified as either trajectory-based or population-based. Trajectory-based algorithms, such as SA, rely on analyzing the solution space using a single point at each iteration and defining a path during the search process [89]. Population-based methods, such as GA and PS, analyze the problem space using a large, but diverse, population at each iteration that evolve during the search [89], and are highly popular for nonlinear problems. Metaheuristics differ from the gradient-based methods in four ways:

(1) Given the stochastic nature of metaheuristic algorithms [89], random sampling prevents the solver from being trapped within local minimums, thus allowing for an effective sweep of the domain space [85], to identify the optimal solution. In the case of gradient-based methods, once the KKT conditions are satisfied, the solver terminates

without further exploration. This limits the solver's ability to identify the "best" solution if a problem comprises of multiple minima. Gradient-based solvers yield an identical optimal for the same initial start.

(2) Metaheuristic algorithms can handle nonlinear constraints without the added complexity of introducing barrier functions, due to random sampling of the domain.

(3) Although the computational efficiency of metaheuristics heavily depends on the problem and solver parameters, such as number of generations and termination tolerances, they do not explicitly require the gradient vector or Hessian matrix, thus requiring no storage space, unlike gradient-based methods [85].

(4) Metaheuristics are easily implemented with nonconvex and noncontinuous functions.

5.3.2.1 Genetic Algorithm

A GA is a suitable metaheuristic for this particular problem because at each iteration, the population is constantly evolving in order to effectively explore the solution space. Genetic algorithms belong to the class of evolutionary algorithms, which rely on biological concepts such as crossover, mutation, elitism, and selection in order to promote diversity [90, 91, 94].

Genetic algorithms belong to the population based subclass of metaheuristic; they are initialized by defining a population comprised of hundreds to thousands of randomly generated individuals (or chromosomes) depending on the problem complexity. The length of a chromosome is equivalent to the number of design parameters involved, and each element of the individual, called a gene, can be expressed either as a binary or real-valued number, as shown in **Figure 33**. With each iteration, called a generation, the population evolves; the evolution of the population begins by selecting parents, from the previous generation, which will breed and create children with better fitness values, for successive generations [54, 90, 91]. The selection process is related to fitness of each individual within the population [95], where the roulette-wheel and tournament selection [55, 86] are commonly applied techniques to select parents.

In the roulette wheel scheme, each individual within the population is assigned a probability, P_j, based on its fitness value defined by [90, 96]

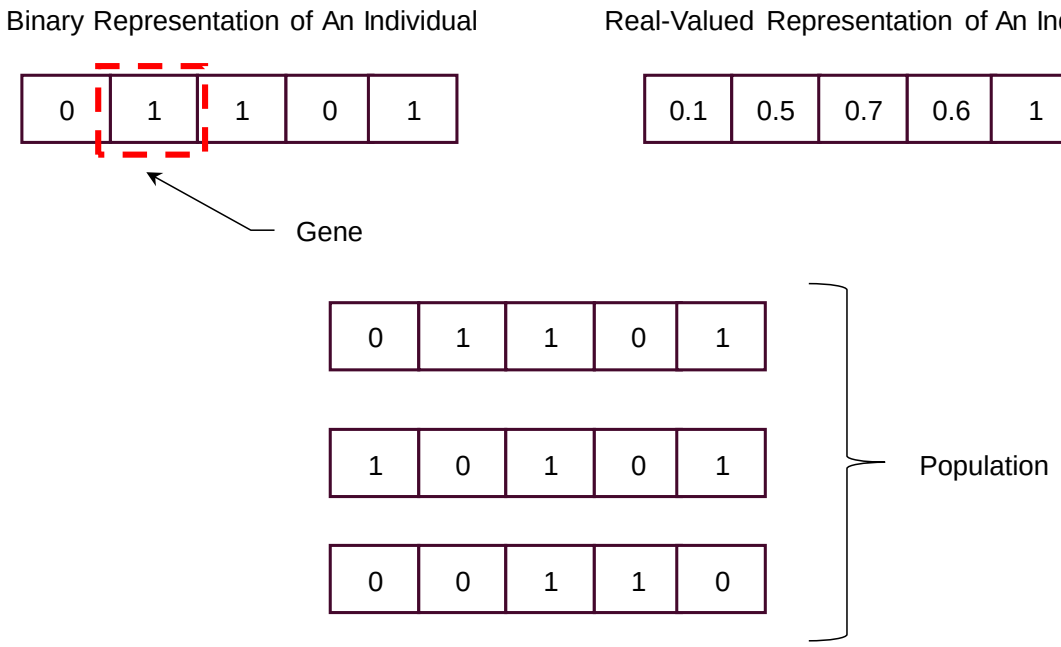

Figure 33: A set of individuals (or chromosomes) defines the population for the GA. The length of each individual is equal to the number of design parameters involved in the optimization study.

$$P\left[\text{Individual } i \text{ is chosen}\right] = \frac{\mathrm{F}_i}{\sum_{j=1}^{Npop} \mathrm{F}_j} \tag{5.16}$$

where F_i is the fitness value of the i^{th} individual and N_{pop} is the population size. A series of random numbers is generated within the interval [0, 1], and compared against the cumulative probability, C_i, of the population [96]

$$C_i = \sum_{j=1}^{i} P_j \tag{5.17}$$

The i^{th} individual is selected as the parent for reproducing children in the successive generation if and only if $C_{i-1} < R[0, 1] \leq C_i$, where R is the randomly generated number [91]. The tournament selection scheme however, randomly selects K individuals from the population and identifies which of the selected has the highest fitness value [90, 94]. The individuals with the best fitness

are selected as parents and this procedure is repeated until N_{pop} for the following generation is satisfied.

Upon selection of the parents, children with better fitness compared to their predecessors are created by applying the biological concepts of crossover, mutation, and elitism. Crossover refers to replacing some genes in one parent by the corresponding genes of the other [90, 91, 95]. Mutations are applied once the new generation has been created. The operator randomly selects a few individuals and changes their respective genes [92]. Alternative to these methods is elitism, which identifies *K* individuals with the highest fitness value, from the current population, and copies the genetic information to the children in the following generation.

This process continues until one of the termination conditions has been reached: surpassing maximum number of generation, no further improvement in the fitness value between successive generations, or exceeding the constraint and function tolerances.

5.3.2.2 Remarks on Metaheuristics

Although metaheuristics are powerful methods and are better suited for complex nonlinear problems compared to gradient-based methods, the solutions identified by these approaches do not satisfy the KKT conditions, and therefore are not locally optimal. To overcome this challenge hybrid techniques have been proposed where metaheuristics are combined with a gradient-based solver to ensure local convergence [85]. In the hybrid approach, a metaheuristic minimization is carried out, and this solution is then treated as the initial start for the gradient-based method to ensure a localized minimum has been found.

5.3.3 Hybrid Method

A hybrid optimization scheme is implemented to assess the design problem. The hybrid algorithm combines the GA with the gradient-based interior point method, which is solved in MATLAB^{TM} using the inbuilt *genetic algorithm function* and *fmincon* interior point method. **Table 11** and **Table 12** summarize the settings for the GA and interior point method, respectively, which

yielded suitable convergence. All other parameters for each algorithm were left as the default values.

Table 11: Settings used for hybridized genetic algorithm

Population Size	Generations	Selection Scheme	Function Tolerance	Constraint Tolerance
2000	300	Roulette Wheel	1e-9	1e-9

Table 12: Settings for the hybridized interior-point method, using MATLAB™ inbuilt function fmincon

Step Tolerance	Function Tolerance	Constraint Tolerance
1e-12	1e-10	1e-10

5.4 Results and Discussion

A deterministic optimization approach is employed, where uncertainties associated with the thermometallurgical model, kinetic model parameters, and zone set-point temperatures are not taken into consideration.

5.4.1 Optimal Solution Using the Interior Point Method

The nominal furnace settings, summarized in **Table 13**, served as the initial seed for the optimization procedure. For the given roller speed and batch spacing, a corresponding cycle time of $F(\mathbf{x}^0) = 29$ seconds is treated as the benchmark. Optimization proceeds from the initial point until the default convergence criteria, which approximately satisfy the KKT conditions, are met. The optimization progress is shown in **Figure 34**. The batch consists of a single component, with a mass of 5 kg, thickness of 1.4 mm, and batch width of 0.5 m.

Table 13: Initial start point, $\mathbf{x}^0$, x_1^0-x_{12}^0 [°C], x_{13}^0 [m], x_{14}^0 [cm/s], and cycle time [s]

x_1^0	x_2^0	x_3^0	x_4^0	x_5^0	x_6^0	x_7^0	x_8^0	x_9^0	x_{10}^0	x_{11}^0	x_{12}^0	x_{13}^0	x_{14}^0	$F(\mathbf{x}^0)$
815	825	850	855	880	920	920	930	930	925	920	915	1.745	6.0	29

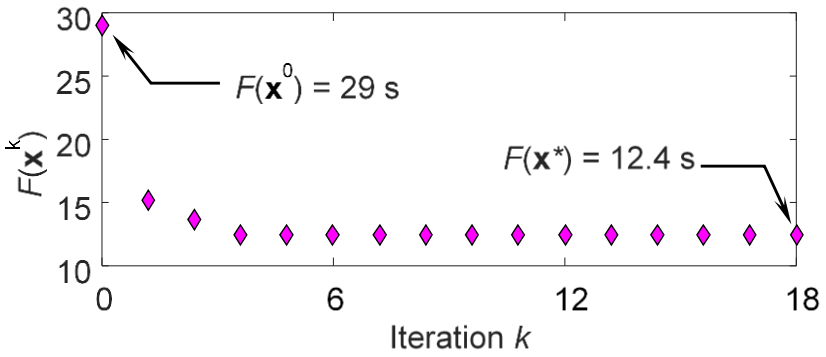

Figure 34: Example optimization progress for the gradient-based interior point method, using the first-order kinetics model [10], with constraint c_{N13a} enforced.

The optimal solutions are summarized in **Table 14**. Two scenarios for the austenitization constraint are considered: the first one is a temperature-based criterion, c_{N13}, which reflects current industrial practice, and the second explicitly enforces a minimum modelled austenite phase fraction at the furnace exit, c_{N13a} based on the first-order austenitization model [10] presented in Chapter 3. The optimal furnace parameters, between these two constraints, differ significantly, although the difference in cycle time is small. The greatest savings in cycle time is realized with c_{N13a}, of 17 seconds faster than the nominal solution, while the improvement using c_{N13} is slightly less. This reflects that the temperature-based constraint is more conservative compared to the explicitly modelled austenite constraint. A comparison between the optimal solutions indicate that the last seven zones of c_{N13}, were on average 20-30°C higher than when c_{N13a} was imposed, in order to satisfy the temperature-based surrogate austenitization condition. In addition, the results indicate that the zones can operate at significantly lower temperature in order to achieve desired austenitization, which is consistent with the validation results in §4.1.2.

Table 14: Optimal solutions and associated cycle time for the optimization problem using the first-order model [10] and nonlinear constraints c_{N13} and c_{N13a}.

	x_1^*	x_2^*	x_3^*	x_4^*	x_5^*	x_6^*	x_7^*	x_8^*	x_9^*	x_{10}^*	x_{11}^*	x_{12}^*	x_{13}^*	x_{14}^*	$F(\mathbf{x}^*)$
c_{N13}	842	843	856	860	879	905	905	908	908	907	905	903	1.765	13.2	13
c_{N13a}	874	864	865	865	878	888	888	882	882	886	888	888	1.768	14.0	12

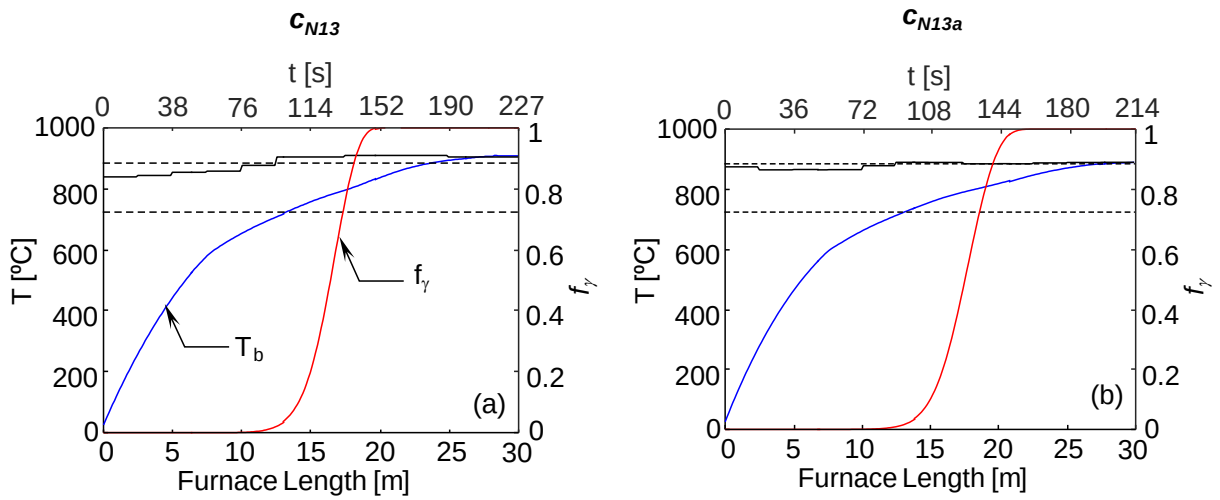

Figure 35: Optimized heating and austenitization profiles for batches with a single blank. Dashed lines correspond to the austenite start and finish temperatures, T_{Ac1} = 730ºC and T_{Ac3} = 880ºC. Black solid lines are zone temperatures.

Further insight can be obtained from the optimized heating and austenitization profiles, shown in **Figure 35**. A detailed comparison of Figures 32 (a) and (b) confirm that constraint c_{N13} is more conservative than c_{N13a}. In both scenarios, the batch is completely austenitized prior to T_{Ac3}, as majority of the transformation occurs near the Ac_1 temperature, as reported by [10, 23].

The optimal zone temperatures are higher than the nominal case for the first five zones to promote austenitization earlier in the heating process, thus allowing for faster part conveyance and an overall reduction in cycle time.

The optimization procedure indicates that the 12 ºC/s constraint, imposed to prevent excessive coating growth, is inactive for both austenitization conditions. However, the temperature-based austenite constraint is active, whereas it is inactive for the explicitly modeled austenite phase fraction. The burner capacities for both constraints are inactive, though the burner capacity for the final zone are near active, as summarized in **Table 15**.

Table 15: Total energy requirements, in [kW], for each zone at the optimal settings

Zone	1	2	3	4	5	6	7	8	9	10	11	12
c_{N13}	122	80	70	51	44	59	60	55	46	38	33	58
c_{N13a}	131	87	74	49	43	57	56	52	45	40	35	60

To verify if this behavior is consistent only for the final zone, the optimization problem was re-evaluated, using the same conditions specified above, with the omission of zone 12. The analysis yielded similar results, where the final zone, operates near the maximum burner rating. This suggests that the final zone is the limiting factor that ensures the selected austenite constraint is satisfied. The optimization problem was also solved using the phenomenological model, as explained in **Appendix C**.

The design problem is also solved for a batch consisting of four blanks, each with a thickness of 1.4 mm, an equivalent mass of 20 kg and batch width of 0.5 m. The initial starting point for this problem is specified within **Table 16**. In this scenario, where the batches are at full capacity, the nominal cycle time is $F(\mathbf{x}^0) = 59$ seconds. The optimal solutions and corresponding profiles are summarized in **Table 17** and **Figure 36**, respectively**.**

Table 16: Initial start point, $\mathbf{x}^0$, $\mathbf{x_1}^0$-$\mathbf{x_{12}}^0$ [°C], $\mathbf{x_{13}}^0$ [m], $\mathbf{x_{14}}^0$ [cm/s], and cycle time [s]

x_1^0	x_2^0	x_3^0	x_4^0	x_5^0	x_6^0	x_7^0	x_8^0	x_9^0	x_{10}^0	x_{11}^0	x_{12}^0	x_{13}^0	x_{14}^0	$F(\mathbf{x}^0)$
815	825	850	855	880	920	920	930	930	925	920	915	3.59	5.0	59

Table 17: Optimal solutions and associated cycle time for the optimization problem using the first-order model [10] and nonlinear constraints c_{N13} and c_{N13a}.

	x_1^*	x_2^*	x_3^*	x_4^*	x_5^*	x_6^*	x_7^*	x_8^*	x_9^*	x_{10}^*	x_{11}^*	x_{12}^*	x_{13}^*	x_{14}^*	$F(\mathbf{x}^*)$
c_{N13}	843	846	857	861	879	903	903	905	905	905	903	901	3.617	13.0	28
c_{N13a}	907	877	905	907	883	908	891	892	851	911	871	872	3.6123	16.6	22

The first five zones for both austenite conditions are higher than the ones from the nominal settings, whereas the remainder are significantly lower. This once again indicates that batches can be austenitized using lower operating temperatures than currently established parameters. The temperature-based constraint yields a savings of 31 seconds compared to the explicit constraint corresponding to savings of 37 seconds. Similar to the single blank case all constraints were inactive, except for c_{N13} and the burner capacity for zone 12. The optimized heating and austenitization profiles shown in **Figure 36** display that the batches achieve adequate

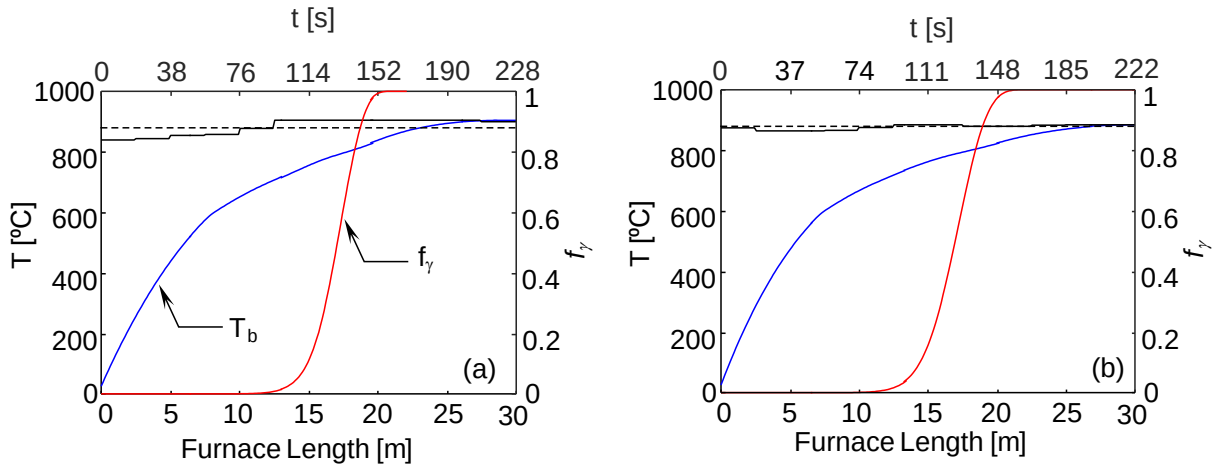

Figure 36: Optimized heating and austenitization profiles for batches composed of four blanks. Dashed lines correspond to the austenite start and finish temperatures, T_{Ac1} = 730ºC and T_{Ac3} = 880ºC. Black solid lines are zone temperatures. (a) Corresponds to the temperature-based austenite constraint; (b) is the optimal for the explicitly modeled constraint.

austenitization well before the furnace exit and that majority of the transformation takes place near Ac_1.

5.4.2 Optimal Solution Using the Hybrid Scheme

The hybrid scheme was used to evaluate the design problem, as constructed in §5.2, 15 times, where each execution had a newly randomly generated initial population. The purpose of the performing multiple executions is to verify that the optimal solutions were consistent amongst different runs, which would be evident if the majority of the solutions were the same (i.e. lie within the same optimal region region), thus yielding a near identical objective value. The hybrid scheme focuses on batches with only a single unpatched blank.

The optimal solutions identified using the hybrid approach are shown in **Figure 37**. When the temperature-based austenite constraint is applied, it is evident that the first ten zones operate near the upper bound, ~950ºC, allowing the batches to heat rapidly, whereas the remaining two zones have optimal set-point temperatures that vary significantly between optimal runs. A possible reason for this variation may be that upon reaching zone 10, the blank is either slightly above or

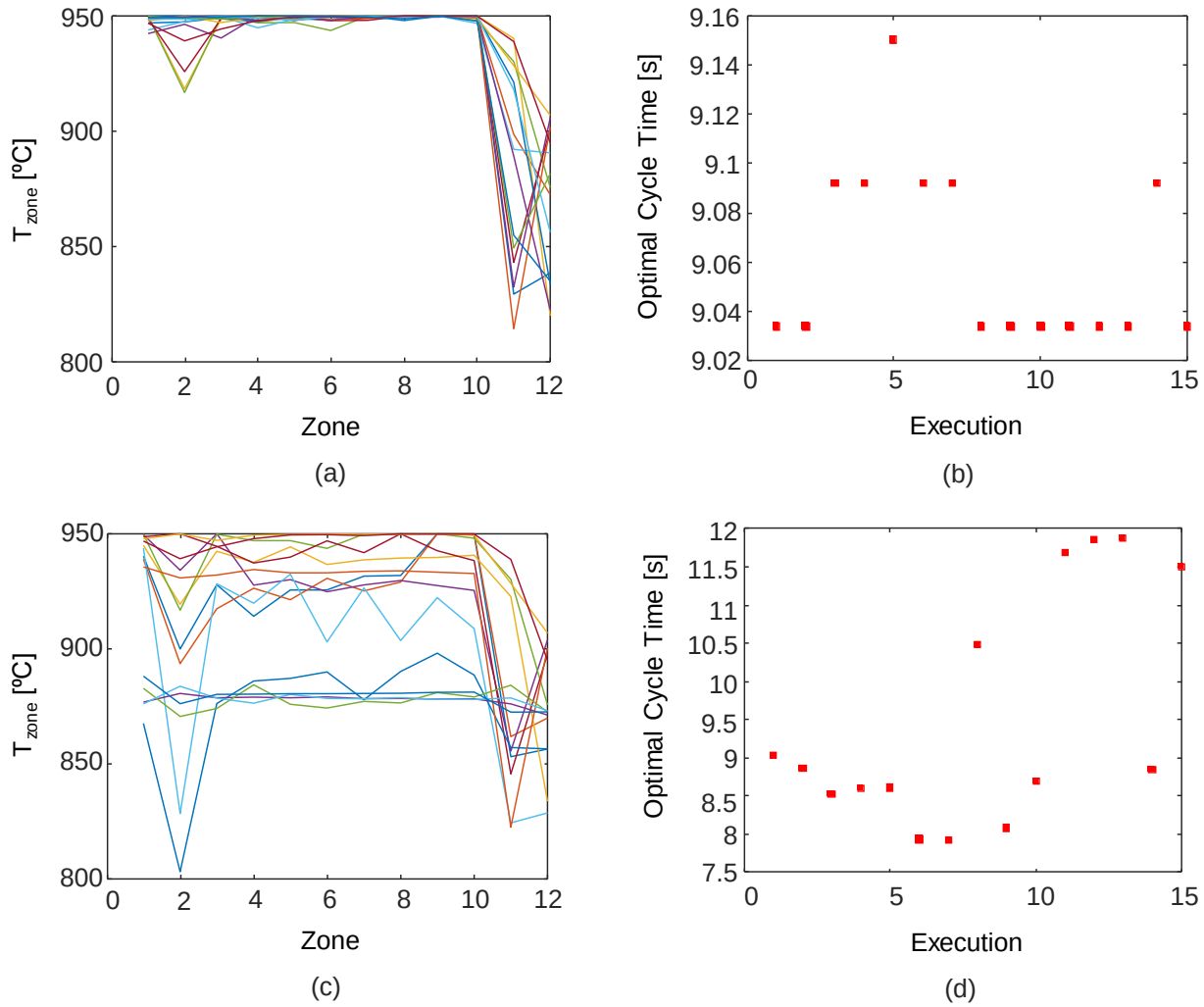

Figure 37: Optimal solutions identified by the hybrid algorithm, using a GA and gradient-based interior point method. (a) and (b) correspond to the temperature-based austenite constraint. (c) and (d) correspond to the explicitly modeled austenite constraint.

greater than 900ºC thus the set-point temperatures for zones 11 and 12 are not as significant to the overall process, so long as the austenite constraint is just satisfied. Thus, zones 11 and 12 act as soaking zones (which contribute to isothermal annealing conditions in the HFDQ process). **Figure 37(b)** shows that the majority of the solutions yield a minimized cycle time of 9.1 seconds, which corresponds to a savings of approximately 20 seconds from the nominal settings. Two interesting differences between the optimums of the methods used are observed. First, the hybrid specified optimal zone temperatures and roller speed are significantly higher than the gradient-based scheme; second, the optimal cycle time identified by the hybrid scheme is on average 3 seconds

faster. Both observations further reinforce how advanced heuristics allow effective exploration of the solution space without being trapped within a local optimum. The cycle length and roller speed were relatively consistent amongst runs with a value of 1.745 meters and 0.192 m/s, respectively.

Figure 37(c) shows the optimal results for the zone temperatures when the explicitly modeled austenite constraint is enforced. As observed there is no clear indication of a concentrated minimum, instead there appears to be a series of solutions that satisfy all the functional requirements. This is further supported by the fact that at each execution of the hybrid algorithm, the optimal cycle time is different. One possible reason for this variation may arise from the first-order model [10] predicting that sufficient austenitization is achieved at temperatures below T_{Ac3}, (*i.e.* 820°C to 950°C), while capable of satisfying the remaining constraints. This was also observed during experimental validations, using the muffle furnace at an extraction temperature of 820°C, as discussed in §4.1.2. Variations in the cycle length and roller speed are also evident, ranging from 1.749 – 1.866 m and 0.15 – 0.22 m/s, respectively. Although significant savings are realized using this constraint against the nominal settings and the soak-based constraint, for the given number of evaluations, the best and worst cycle times are 8 seconds and 12 seconds, respectively. Thus, only the best solution from the multiple runs will be considered.

The optimized solutions obtained using the alternative austenitization constraints are summarized in **Table 18**.

Table 18: Optimal solutions and associated cycle time using the hybrid scheme.

	x_1^*	x_2^*	x_3^*	x_4^*	x_5^*	x_6^*	x_7^*	x_8^*	x_9^*	x_{10}^*	x_{11}^*	x_{12}^*	x_{13}^*	x_{14}^*	$F(\mathbf{x}^*)$
c_{N13}	949	949	949	950	950	950	950	949	950	948	846	835	1.745	19.2	9
c_{N13a}	949	950	944	937	939	947	942	950	943	938	845	898	1.765	22.3	8

The optimal heating and austenitization curves are shown in **Figure 38**. Similar to the gradient-based method, the 12 ºC/s constraint and a maximum batch temperature of 950ºC are not exceeded. However, the austenite constraint for the soak-time based requirement is active. The burner capacities for each of the individual zones were not exceeded, although zone 12's rating was close to the maximum. Compared to the gradient-based methods, it is evident that the batches are able to exit the furnace, fully austenitized, well in advanced, due to the higher operating

conditions and roller speed. Similar to the interior point method, the batches austenitize well in advance of the furnace exit; it is also observed that most of the austenitization occurs near T_{Ac1}.

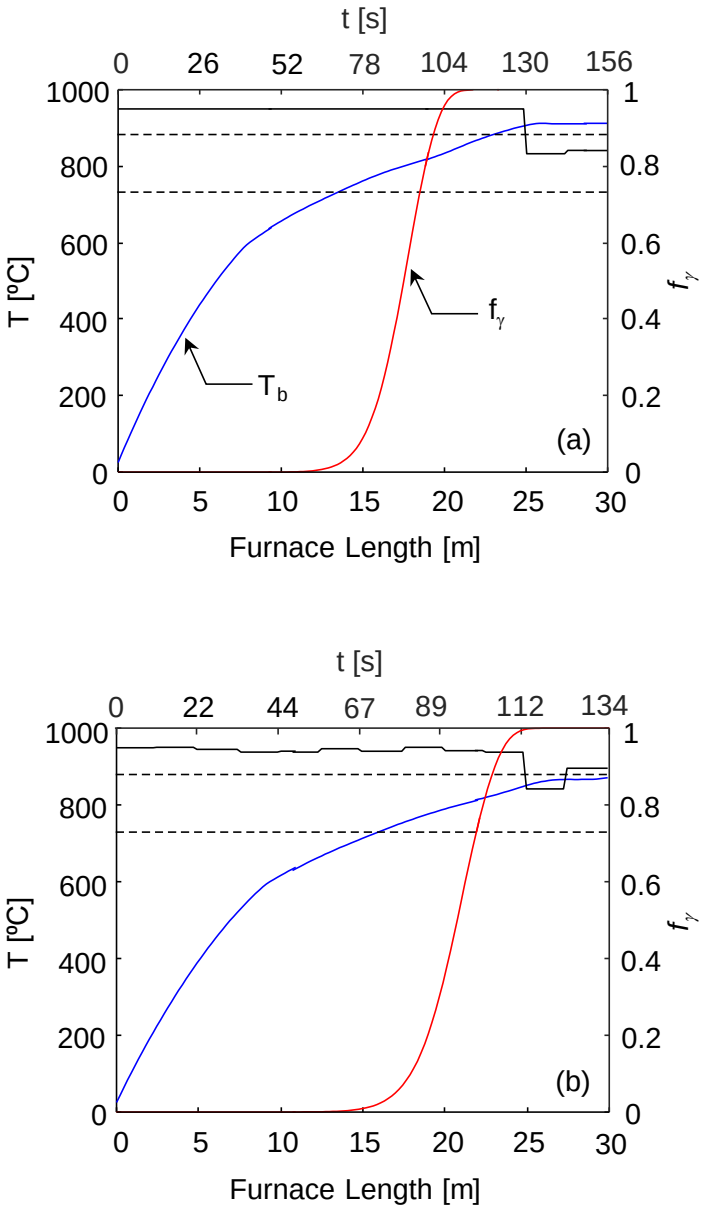

Figure 38: Optimized heating and austenitization profiles for batches composed of a single blank. Dashed lines correspond to the austenite start and finish temperatures, T_{Ac1} = 730ºC and T_{Ac3} = 880ºC. Black solid lines are zone temperatures. (a) Corresponds to the temperature-based austenite constraint; (b) is the optimal for the explicitly modeled constraint.

5.5 Summary of the Design Optimization

A process optimization was carried out on a 12-zone roller hearth furnace, to minimize the cycle time, whilst optimizing fourteen design parameters: zone temperatures, cycle length, and roller speed, subject to a set of functional requirements. In this study, two alternative forms of austenitization constraints were considered; a soak-time based constraint, c_{N13}, and an explicitly modeled constraint, c_{N13a}. A gradient-based interior point method and a hybrid optimization scheme, combining a GA with the interior point method, were implemented to evaluate the problem.

The interior point method showed savings of approximately 17 seconds from the nominal settings and indicated that batches can be adequately austenitized at lower operating temperatures. The gradient-based technique indicated that c_{N13} was conservative compared to c_{N13a}, and that all constraints were inactive.

Next, a hybrid scheme was used to assess the problem by performing 15 executions. The algorithm, with the soak-based constraint enforced, showed that the first ten zones operate near the upper bound whereas the remaining two experience variability, thus behaving as soaking zones. When the explicitly modeled austenite constraint was imposed, on the other hand, there was considerable variability in the optimal solutions between each execution, which is a consequence of the first-order model [10] predicting sufficient batch austenitization at temperatures below T_{Ac3}. In both cases, the minimized cycle time achieved greater improvements compared to the gradient-based method.

These findings indicate that the solution space may contain multiple minimums, hence the weaker performance shown by the gradient-based method; and that the choice of the austenitization constraint is crucial when selecting operation parameters to minimize the cycle time, while ensuring complete austenitization.

Chapter Six
Conclusion and Future Work

6.1 Conclusion

The heating stage of hot stamping is used to austenitize ultra-high strength steels, and in the case of Usibor® 1500AS, transform the Al-Si coating into a ternary Al-Si-Fe intermetallic layer with desired properties and thickness.

In order to optimize production efficiency and improve current industrial practices, a thermometallurgical model that couples heating and austenitization is necessary in order to provide a physical foundation for the relationship between blank heating, austenitization, and selection of furnace parameters. Numerous thermal models for furnace-based heating have been developed to simulate heating of the load, yet to date none explicitly account for austenite formation.

The thermometallurgical model proposed in this study consists of a heat transfer submodel, which simulates the transient temperature of unpatched/patched blanks, and two candidate austenite kinetics submodels: a first-order empirical model and one that explicitly accounts for nucleation, growth, and impingement. Confidence intervals were also constructed to account for uncertainties with the surrounding temperatures and model parameters, using a Monte Carlo technique.

The models were validated by comparing simulation temperature and austenite phase fractions with thermocouple and hardness measurements made on instrumented single- and double-gauge coupons, undergone continuous and intercritical annealing, in a laboratory muffle furnace, and patched blanks heated in an industrial roller hearth furnace. The first-order submodel predictions were consistent with the experimental results, whereas the phenomenological submodel severely under estimated the austenite formation, and failed to show complete austenitization even for coupons exceeding T_{Ac3}. The phenomenological submodel performed

better for the intercritical annealing tests at temperatures closer to T_{Ac1}, a consequence of model over-tuning and over estimation of the impingement.

Next, a deterministic optimization procedure was developed using the validated thermometallurigcal model, exclusively with the first-order kinetics submodel, to minimize the cycle time of a 12-zone roller hearth furnace by identifying the optimal zone temperatures, cycle length, and roller speed, subject to a set of linear and nonlinear constraints. The design problem was evaluated using a gradient-based interior point method, which transforms nonlinear constraints into weighted logarithmic penalty functions and a hybrid approach, combining a GA with the interior point method. Two austenitization constraints were considered: one based on soaking time and one on modelled austenite formation within the blanks leaving the furnace. In general, the explicit austenite phase fraction constraint yielded significant improvements against defined soak time, which is more conservative. The performance of the optimal solution strongly depended on which austenitization constraint was enforced.

6.2 Future Work

The thermometalurigcal model is an effective tool to predict the heating and austenitization curves for unpatched/patched blanks. Its effectiveness is further extended to optimizing furnace parameters to ensure complete austenitization of batches while maximizing throughput. Although, the model and optimization scheme yield feasible solutions, prior to industrial deployment, further improvements are necessary.

The uncertainty estimates attached to the thermometallurgical model can be improved by extending the Monte Carlo analysis to incorporate other model parameters, in particular the radiative properties and specific heat of the blanks, which in practice are not perfectly known. More advanced models should also address the Al-Si layer transformation, in particular the coating kinetics to prevent excessive growth, which influences the thermal model through the change in the radiative properties. The melting of coating reduces the life of ceramic rollers and causes them to dislocate within the furnace. While coating liquefaction cannot be prevented, industry could use such a model to determine process parameters that minimize the impact.

Further focus will be also dedicated to improving upon the optimization model by considering a multi-objective scheme that minimizes the energy consumption and cycle time, while ensuring batches are fully austenitized. Currently, the optimization scheme only focuses on unpatched blanks; however, in industrial settings batches may consists of a combination of unpatched/patched blanks. The optimization model could be used to identify feasible furnace settings that not only allow sufficient batch austenitization, but also ensure adequate transformation of the Al-Si layer. In such cases the thermal mass of the patched and unpatched regions are the limiting factors, respectively. Most importantly, in the view of uncertainty attached to the thermometallurgical model due to model parameters, zone temperatures, and steel composition, further design optimization studies should be conducted in a statistical setting using design optimization under uncertainty tools.

References

[1] H. Karbasian and A. E. Tekkaya, "A Review on Hot Stamping," *Journal of Materials Processing Technology*, vol. 210, no. 15, pp. 2103-2118, 2010.

[2] R. A. Daziano and E. Chiew, "Electric Vehicles Rising From The Dead: Data Needs For Forecasting Consumer Response Toward Sustainable Energy Sources In Personal Transportation," *Energy Policy*, vol. 51, pp. 876-894, 2012.

[3] A. Turetta, S. Bruschi and A. Ghiotti, "Investigation Of 22MnB5 Formability In Hot Stamping Operations," *Journal of Materials Processing Technology*, vol. 177, pp. 396-400, 2006.

[4] M. Naderi, "Hot Stamping of Ultra High Strength Steels," (Master's thesis, RWTH Aachen University), 2007.

[5] R. Wohlecker, M. Johannaber and M. Espig, "Determination of Weight Elasticity of Fuel Economy for ICE, Hybrid and Fuel Cell Vehicles," *SAE Technical Paper*, no. 2007-01-0343, 2007.

[6] X. Bano and J. P. Laurent, "Heat Treated Boron Steels in the Automotive Industry," in *In 39 th Mechanical Working and Steel Processing Conference*, 1997.

[7] T. Nonaka, K. Goto, H. Taniguchi and K. Yamazaki, "Developments of Ultra High-Strength Cold-Rolled Steel Sheets for Automotive Use," *Nippon Steel Technical Report*, vol. 88, pp. 12-14, 2003.

[8] H. Lehmann, "Rollenherdöfen für die Wärmbehandlung beim Presshärten. In:Pfeifer, H., Nacke, B., Beneke, F. (Eds.)," Vulkan-Verlag, Essen, Germany, 2011.

[9] M. Naderi, A. Saeed-Akbari and W. Bleck, "The Effects of Non-isothermal Deformation on Martensitic Transformation In 22MnB5 Steel," *Materials Science and Engineering: A*, no. 487, pp. 445-455, 2008.

[10] M. Di Ciano, N. Field, M. Wells and D. K., "Development of an Austenitization Kinetics Model for 22MnB5 Steel," *Journal of Materials Engineering and Performance*, vol. 27, no. 4, pp. 1792-1802, 2018.

[11] N. Field, " Austenitization of Ultra High Strength Steel by Direct Contact Heating for Hot Forming Die Quenching (Master's thesis, University of Waterloo)," 2017.

[12] M. Merklein and J. Lechler, "Investigation of The Thermo-mechanical Properties of Hot Stamping Steels," *Journal of Materials Processing Technology*, vol. 177, no. 1-3, pp. 452-455, 2006.

[13] C. Allély, L. Dosdat, O. Clauzeau, K. Ogle and P. Volovitch, "Anticorrosion Mechanisms of Aluminized Steel for Hot Stamping," *Surface and Coatings Technology,* vol. 238, pp. 188-196, 2014.

[14] M. Windmann, A. Röttger and W. Theisen, "Phase Formation at The Interface Between a Boron Alloyed Steel Substrate and an Al-rich Coating," *Surface and Coatings Technology*, no. 226, pp. 130-139, 2013.

[15] F. Borsetto, A. Ghiotti and S. Bruschi, "Investigation of The High Strength Steel Al-Si Coating During Hot Stamping Operations," *Key Engineering Materials,* vol. 410, pp. 289-296, 2009.

[16] M. Merklein and J. Lechler, "Determination of Material and Process Characteristics for Hot Stamping Processes of Quenchenable Ultra High Strength Steels With Respect To A FE-based Process Design," *SAE International Journal of Materials and Manufacturing,* vol. 1, no. 1, pp. 411-426, 2009.

[17] L. Garcia Aranda, Y. Chastel, J. Fernández Pascual and T. Dal Negro, "Experiments and Simulation of Hot Stamping of Quenchable Steels," *Advanced Technology of Plasticity 2*, pp. 1135-1140, 2002.

[18] R. George, A. Bardelcik and M. Worswick, "Hot Forming of Boron Steels Using Heated and Cooled Tooling for Tailored Properties," *Journal of Materials Processing Technology,* vol. 212, no. 11, pp. 2386-2399, 2012.

[19] E. J. Caron, K. J. Daun and M. A. Wells, "Experimental Heat Transfer Coefficient Measurements During Hot Forming Die Quenching of Boron Steel at High Temperatures," *International Journal of Heat and Mass Transfer,* vol. 71, pp. 396-404, 2014.

[20] F. G. Caballero, C. Capdevila and C. G. De Andres, "Modelling of Kinetics and Dilatometric Behaviour of Austenite Formation in a Low-carbon Steel With a Ferrite Plus Pearlite Initial Microstructure," *Journal of Materials Science,* vol. 37, no. 16, pp. 3533-3540, 2002.

[21] M. J. Holzweissig, J. Lackmann, S. Konrad, M. Schaper and T. Niendorf, "Influence of Short Austenitization Treatments on The Mechanical Properties of Low-alloy Steels For Hot Forming Applications," *Metallurgical and Materials Transactions A,* vol. 46, no. 7, pp. 3199-3207, 2015.

[22] M. Verma, Y. H, J. Culham, M. Di Ciano and K. Daun, "Development and Validation of a Thermometallurgical Model for Furnace-based Austenitization During Hot Stamping," (Submitted) *Journal of Heat Transfer,* 2018.

[23] K. Jhajj, S. Slezak and K. Daun, "Inferring the Specific Heat of an Ultra High Strength Steel During the Heating Stage of Hot Forming Die Quenching, Through Inverse Analysis," *Applied Thermal Engineering,* vol. 83, pp. 98-107, 2015.

[24] N. Li, J. Lin, D. S. Balint and T. A. Dean, "Experimental Characterisation of the Effects of Thermal Conditions on Austenite Formation for Hot Stamping of Boron Steel," *Journal of Materials Processing Technology,* vol. 231, pp. 254-264, 2016.

[25] N. Li, J. Lin, D. S. Balint and T. A. Dean, "Modelling of Austenite Formation During Heating in Boron Steel Hot Stamping Processes," *Journal of Materials Processing Technology,* vol. 237, pp. 394-401, 2016.

[26] M. J. Holzweissig, J. Lackmann, S. Konrad, M. Schaper and T. Niendorf, "Influence of Short Austenitization Treatments on the Mechanical Properties of Low-alloy Steels For Hot Forming Applications," *Metallurgical and Materials Transactions A,* vol. 46, no. 7, pp. 3199-3207, 2015.

[27] M. Twynstra, K. Daun, E. Caron, N. Adam and D. Womack, "Modelling and Optimization of a Batch Furnace For Hot Stamping," in *ASME 2013 Heat Transfer Summer Conference*, Minneapolis, Minnesota, USA, 2013.

[28] J. N. Rasera, K. J. Daun, C. J. Shi and M. D'Souza, "Direct Contact Heating for Hot Forming Die Quenching," *Applied Thermal Engineering,* vol. 98, pp. 1165-1173, 2016.

[29] J. Rasera, "Development of a Novel Technology for Rapid Austenizing Usibor 1500P," (Master's thesis, University of Waterloo), 2015.

[30] C. Shi, K. J. Daun and M. A. Wells, "Spectral Emissivity Characteristics of the Usibor® 1500P Steel During Austenitization In Argon And Air Atmospheres," *International Journal of Heat and Mass Transfer*, vol. 91, pp. 818-828, 2015.

[31] G. R. Speich, V. A. Demarest and R. L. Miller, "Formation of Austenite During Intercritical Annealing of Dual-phase Steels," *Metallurgical and materials transactions A,* vol. 12, no. 8, pp. 1419-1428, 1981.

[32] L. O. Wolf, F. Nürnberger, D. Rodman and H. J. Maier, "The Effect of Intercritical Annealing on the Microstructure and Mechanical Properties of Ferritic–Martensitic Two-Phase Steels," *Steel Research International,* vol. 88, no. 2, p. 1600107, 2017.

[33] H. Surm, O. Kessler, M. Hunkel, F. Hoffmann and P. Mayr, "Modelling the Ferrite/Carbide→ Austenite Transformation of Hypoeutectoid and Hypereutectoid Steels," in *Journal de Physique IV*, 2004.

[34] C. G. de Andrés, F. G. Caballero, C. Capdevila and L. F. Alvarez, "Application of Dilatometric Analysis to the Study of Solid–solid Phase Transformations In Steels," *Materials Characterization,* vol. 48, no. 1, pp. 101-111, 2002.

[35] A. J. 0. and A. McWilliams, *Journal of the Iron and Steel Institute,* vol. 2, p. 352, 1905.

[36] J. Huang, W. J. Poole and M. Militzer, "Austenite Formation During Intercritical Annealing," *Metallurgical and Materials Transactions A,* vol. 35, no. 11, pp. 3363-3375, 2004.

[37] G. A. Roberts and R. F. Mehl, "The Mechanism and the Rate of Formation of Austenite From Ferrite-cementite Aggregates," *Transactions of the ASM,* vol. 31, pp. 613-650, 1943.

[38] A. Roosz, Z. Gacsi and E. G. Fuchs, "Isothermal Formation of Austenite in Eutectoid Plain Carbon Steel," *Acta Metallurgica,* vol. 31, no. 4, pp. 509-517, 1983.

[39] F. García Caballero, C. Capdevila and C. García de Andrés, "Influence of Scale Parameters of Pearlite on the Kinetics of Anisothermal Pearlite-To-Austenite Transformation in a Eutectoid Steel," *Scripta Materialia,* vol. 42, pp. 1159-1165, 2000.

[40] G. R. Speich, V. A. Demarest and R. L. Miller, "Formation of Austenite During Intercritical Annealing of Dual-Phase Steels," *Metallurgical and Materials Transactions A,* vol. 12, no. 8, pp. 1419-1428, 1981.

[41] W. Callister, Fundamentals of Materials Science and Engineering, London, UK: John Wiley & Sons, Inc..

[42] H. K. Khaira, A. K. Jena and M. C. Chaturvedi, "Effects of Heat Treatment Cycle on Equilibrium Between Ferrite and Austenite During Intercritical Annealing," *Materials Science and Engineering: A,* vol. 161, no. 2, pp. 267-271, 1993.

[43] V. I. Savran, Y. Van Leeuwen, D. N. Hanlon, C. Kwakernaak, W. G. Sloof and J. Sietsma, "Microstructural Features of Austenite Formation in C35 and C45 Alloys," *Metallurgical and Materials Transactions A,* vol. 38, no. 5, pp. 946-955, 2007.

[44] D. P. Datta and A. M. Gokhale, "Austenitization Kinetics of Pearlite and Ferrite Aggregates in a Low Carbon Steel Containing 0.15 wt pct C," *Metallurgical Transactions A,* vol. 12, no. 3, pp. 443-450, 1981.

[45] F. L. G. Oliveira, M. S. Andrade and A. B. Cota, "Kinetics of Austenite Formation During Continuous Heating in a Low Carbon Steel," *Materials Characterization,* vol. 58, no. 3, pp. 256-261, 2007.

[46] M. A. Asadabad, M. Goodarzi and S. Kheirandish, "Kinetics of Austenite Formation in Dual Phase Steels," *ISIJ international,* vol. 48, no. 9, pp. 1251-1255, 2008.

[47] J. Cai, "Modelling of Phase Transformation in Hot Stamping of Boron Steel," (PhD Dissertation Imperial College London), 2011.

[48] W. Liang, W. Tao, B. Zhu and Y. Zhang, "Influence of Heating Parameters on Properties of the Al-Si Coating Applied to Hot Stamping," *Science China Technological Sciences,* vol. 60, no. 7, pp. 1088-1102, 2017.

[49] S. J. Grauer, E. J. F. R. Caron, N. L. Chester, M. A. Wells and K. J. Daun, "Investigation of Melting in the Al–Si Coating of a Boron Steel Sheet by Differential Scanning Calorimetry," *Journal of Materials Processing Technology,* vol. 216, pp. 89-94, 2015.

[50] R. Kolleck, R. Veit, H. Hofmann and F. J. Lenze, "Alternative Heating Concepts for Hot Sheet Metal Forming," in *1st International Conference on Hot Sheet Metal Forming of High-Performance SteeL,* Kassel, Germany, 2008.

[51] R. Kolleck, R. Veit, M. Merklein, J. Lechler and M. Geiger, "Investigation on Induction Heating for Hot Stamping of Boron Alloyed Steels," *CIRP Annals,* vol. 58, no. 1, pp. 275-278, 2009b.

[52] R. Veit, H. Hofmann, R. Kolleck and S. Sikora, "Investigation of the Phase Formation of AlSi-Coatings for Hot Stamping of Boron Alloyed Steel," in *In AIP Conference Proceedings*, 2011.

[53] M. Verma, M. Di Ciano, J. R. Culham, C. Yau and K. J. Daun, "Minimizing the Cycle Time of a Roller Hearth Furnace for Hot-Forming Die-Quenching," in *IOP Conference Series: Materials Science and Engineering*, Waterloo, ON, 2018.

[54] N. Chakraborti, K. Deb and A. Jha, "A Genetic Algorithm Based Heat Transfer Analysis of a Bloom Re-heating Furnace," *Steel Research,* vol. 71, no. 10, pp. 396-402, 2000.

[55] V. R. Heng, H. S. Ganesh, A. R. Dulaney, A. Kurzawski, M. Baldea, O. A. Ezekoye and T. F. Edgar, "Energy-oriented Modeling and Optimization of a Heat Treating Furnace," *Journal of Dynamic Systems, Measurement, and Control,* vol. 139, no. 6, 2017.

[56] S. R. Carvalho, T. H. Ong and G. Guimaraes, "A Mathematical and Computational Model of Furnaces for Continuous Steel Strip Processing," *Journal of Materials Processing Technology,* vol. 178, no. 1-3, pp. 179-387, 2006.

[57] H. E. Pike Jr and S. J. Citron, "Optimization Studies of a Slab Reheating Furnace," *Automatica,* vol. 6, no. 1, pp. 41-50, 1970.

[58] H. Ramamurthy, S. Ramadhyani and R. Viskanta, "A Thermal System Model for a Radiant-tube Continuous Reheating Furnace," *Journal of Materials Engineering and Performance,* vol. 4, no. 5, pp. 519-531, 1995.

[59] A. Steinboeck, D. Wild, T. Kiefer and A. Kugi, "A Mathematical Model of a Slab Reheating Furnace With Radiative Heat Transfer and Non-participating Gaseous Media," *International Journal of Heat and Mass Transfer,* vol. 53, no. 26-26, pp. 5933-5946, 2010.

[60] S. H. Han, S. W. Baek and M. Y. Kim, "Transient Radiative Heating Characteristics of Slabs in a Walking Beam Type Reheating Furnace," *International Journal of Heat and Mass Transfer,* vol. 52, no. 3-4, pp. 1005-1011, 2009.

[61] J. Tonne, J. Clobes, M. Alsmann, A. Ademaj, M. Mischka, W. Morgenroth, H. Becker and O. Stursberg, "Model-based Optimization of Furnace Temperature Profiles with Regard to Economic and Ecological Aspects in Hot Stamping of 22MnB5," in *4th International Conference: Proceedings Hot Sheet Metal Forming of High-Performance Steel,* 2013.

[62] H. S. Ganesh, T. F. Edgar and M. Baldea, "Modeling, Optimization and Control of an Austenitization Furnace for Achieving Target Product Toughness and Minimizing Energy Use," *Journal of Process Control (In Press),* 2017.

[63] D. F. Watt, L. Coon, M. Bibby, J. Goldak and C. Henwood, "An Algorithm for Modelling Microstructural Development in Weld Heat-affected Zones (Part A) Reaction Kinetics," *Acta Metallurgica,* vol. 36, no. 11, pp. 3029-3035, 1988.

[64] K. Morgan, R. W. Lewis and O. C. Zienkiewicz, "An Improved Algrorithm for Heat Conduction Problems with Phase Change," *International Journal for Numerical Methods in Engineering,* vol. 12, no. 7, pp. 1191-1195, 1978.

[65] C. Bonacina, G. Comini, A. Fasano and M. Primicerio, "Numerical Solution of Phase-change Problems," *International Journal of Heat and Mass Transfer,* vol. 16, no. 10, pp. 1825-1832, 1973.

[66] G. P. Krielaart, Brakman, C. M. and S. Van der Zwaag, "Analysis of Phase Transformation in Fe-C Alloys Using Differential Scanning Calorimetry," *Journal of Materials Science,* vol. 31, no. 6, pp. 1501-1508, 1996.

[67] K. Jhajj, "Heat Transfer Modeling Of Roller Hearth And Muffle Furnace," (Master's thesis, University of Waterloo), 2015.

[68] P. o. U. 1. P. Arcelor-Mittal.

[69] T. L. Bergman, F. P. Incropera, D. P. DeWitt and A. S. Lavine, Fundamentals of Heat and Mass Transfer, John Wiley & Sons, Inc., 2011.

[70] J. R. Howell, R. Siegel and P. M. Menguc, Thermal Radiation Heat Transfer, CRC Press, 2016.

[71] E. Radziemska and W. Lewandowski, "Heat Transfer by Natural Convection from an Isothermal Downward-Facing Round Plate in Unlimited Space," *Applied Energy,* vol. 68, pp. 347-366, 2001.

[72] C. I. Garcia and A. J. DeArdo, "Formation Of Austenite In 1.5 Pct Mn Steels," *Metallurgical Transactions A,* vol. 12, no. 3, pp. 521-530, 1981.

[73] H. Chen, Y. C. Liu, D. J. Wang, Z. S. Yan, J. C. Fu and Q. Z. Shi, "A JMAK-Like Approach for Isochronal Austenite–Ferrite Transformation Kinetics in Fe–0·055 wt-% N Alloy," *Materials Science and Technology,* vol. 26, no. 5, pp. 572-578, 2013.

[74] F. Liu, F. Sommer, C. Bos and E. J. Mittemeijer, "Analysis of Solid State Phase Transformation Kinetics: Models and Recipes," *International Materials Reviews,* vol. 52, no. 4, pp. 193-212, 2007.

[75] F. García Caballero, C. Capdevila and C. García de Andrés, "Influence of Scale Parameters of Pearlite on the Kinetics of Anisothermal Pearlite-To-Austenite Transformation in a Eutectoid Steel," *Scripta Materialia,* vol. 42, pp. 1159-1165, 2000.

[76] H. Yan, M. Di Ciano, M. Verma and K. J. Daun, "Intercritical Annealing of 22MnB5 for Hot Forming Die Quenching," in *IOP Conference Series: Materials Science And Engineering*, Waterloo, ON, 2018.

[77] M. Kulakov, W. J. Poole and M. Militzer, "The Effect of the Initial Microstructure on Recrystallization and Austenite Formation in a DP600 Steel," *Metallurgical and Materials Transactions,* vol. 44, no. 8, pp. 3564-3576, 2013.

[78] M. Verma, J. R. Culham, M. Di Ciano and K. J. Daun, "Development of a Thermo-Metallurgical Model to Predict Heating and Austenitization of 22MnB5 for Hot Forming Die Quenching," in *ASME 2017 International Mechanical Engineering Congress and Exposition*, 2017.

[79] "ASTM Standard A1033-10(2015), West Conshohocken PA: ASTM International," 2015.

[80] H. Güler, "Investigation of Usibor 1500 Formability in a Hot Forming Operation," *Materials Science,* vol. 19, no. 2, pp. 1392-1320, 2013.

[81] R. Veit, H. Hofmann, R. Kolleck and S. Sikora, "Investigation of the Phase Formation of AlSi-Coatings for Hot Stamping Of Boron Alloyed Steel," in *AIP Conference Proceedings*, 2011.

[82] S. G. Nash and A. Sofer, Linear and Nonlinear Programming, McGraw Hills, 1996.

[83] J. Nocedal and S. J. Wright, Numerical Optimization, 2nd ed., Springer, 2006.

[84] R. Fletcher and C. M. Reeves, "Function Minimization by Conjugate Gradients," *The Computer Journal*, vol. 7, no. 2, pp. 149-154, 1964.

[85] V. Kelner, F. Capitanescu, O. Léonard and L. Wehenkel, "A Hybrid Optimization Technique Coupling an Evolutionary and a Local Search Algorithm," *Journal of Computational and Applied Mathematics*, vol. 215, no. 2, pp. 448-456, 2008.

[86] P. E. Gill, W. Murray and M. H. Wright, Practical Optimization, 2nd ed., Elsevier Academic Press, 1981.

[87] D. P. Bertsekas, Nonlinear Programming, Blemont, Massachussets: Athena Scientific, 1999.

[88] R. A. Waltz, J. L. Morales, J. Nocedal and D. Orban, "An Interior Algorithm for Nonlinear Optimization that Combines Line Search and Trust Region Steps," *Mathematical Programming*, vol. 107, no. 3, pp. 391-408, 2006.

[89] C. Blum and A. Roli, "Metaheuristics in Combinatorial Optimization: Overview and Conceptual Comparison," *ACM Computing Durveys (CSUR)*, vol. 35, no. 3, pp. 268-308, 2003.

[90] D. S. Weile and E. Michielssen, "Genetic Algorithm Optimization Applied to Electromagnetics: a Review," *IEEE Transactions on Antennas and Propagation*, vol. 45, no. 3, pp. 343-353, 1997.

[91] M. Kumar, M. Husian, N. Upreti and D. Gupta, "Genetic Algorithm: Review and Application," *International Journal of Information Technology and Knowledge Management*, vol. 2, no. 2, pp. 451-454, 2010.

[92] N. Soni and T. Kumar, "Study of Various Mutation Operators in Genetic Algorithms," *International Journal Of Computer Science And Information Technologies*, vol. 5, no. 3, pp. 4519-4521, 2014.

[93] L. Bianchi, M. Dorigo, L. M. Gambardella and W. J. Gutjahr, "A Survey on Metaheuristics for Stochastic Combinatorial Optimization," *Natural Computing*, vol. 8, no. 2, pp. 239-287, 2009.

[94] C. A. Coello Coello and R. L. Becerra, "Evolutionary Multiobjective Optimization In Materials Science And Engineering," *Materials and Manufacturing Processes*, vol. 24, no. 2, pp. 119-129, 2009.

[95] F. Glover and G. A. Kochenberge, Handbook Of Metaheuristics, New York: Kluwer Academic Publishers, 2003.

[96] T. Pencheva, K. Atanassov and A. Shannon, "Modelling of a Roulette Wheel Selection Operator in Genetic Algorithms Using Generalized Nets," *International Journal Bioautomation*, vol. 13, no. 4, pp. 257-264, 2009.

[97] H. Coleman and W. Steele, Experimentation and Uncertainty Analysis for Engineers, New York: John Wiley & Sons, 1989.

[98] OMEGA Engineering, The Temperature Handbook, 2004.

[99] N. Instruments, "SCXITM-1303 32-Channel Isothermal Terminal Block," National Instruments, [Online]. Available: http://www.ni.com/pdf/manuals/321923b.pdf.

Appendix A
Uncertainty Analysis

A.1 Heat Transfer Model

Details about model uncertainty are discussed in §3.7. Uncertainty analysis is performed using a Monte Carlo procedure. Since the muffle furnace and roller hearth furnace are both regulated using a hysteresis control strategy, the temperature profile within are cyclic about the set-point temperature. The temperature variation within the muffle furnace and roller hearth furnace at equilibrium are shown in **Figure A1.1** and **Figure 15**, respectively.

The temperature profile within the muffle furnace and roller hearth furnace have a "saw-tooth" like profile, corresponding to a uniform distribution. **Figure A1.1** represent a uniform distribution because at any instant in time, dτ, the furnaces can be any temperature (*i.e.* all temperatures have an equal likelihood of occurring during operation). This claim can be further

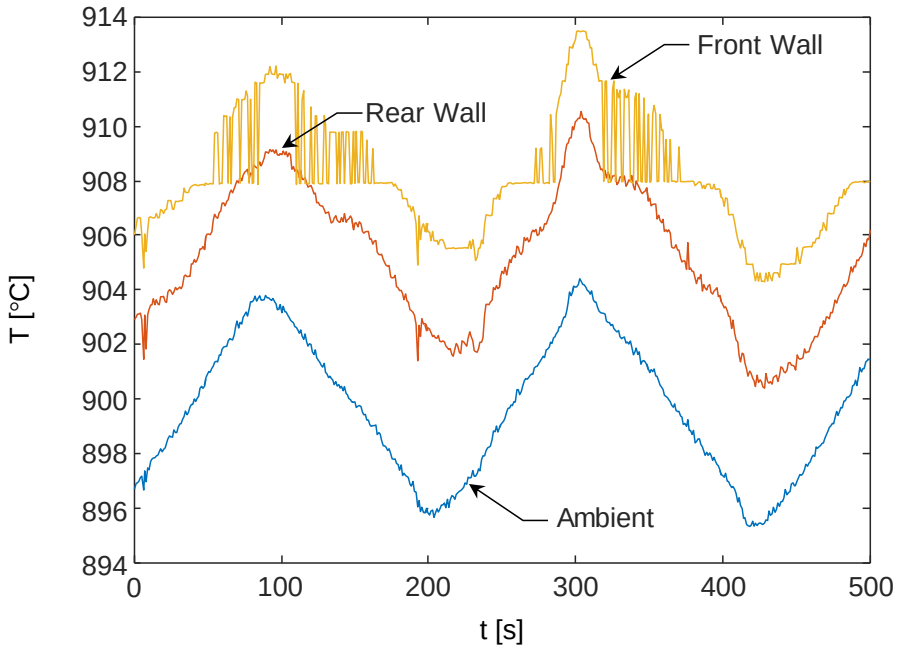

Figure A1.1: Temperature variation within the muffle furnace at equilibrium condition, due to hysteresis control strategy.

supported by plotting a histogram of the probability density function (pdf) for the temperature profiles above, as shown in **Figure A1.2**.

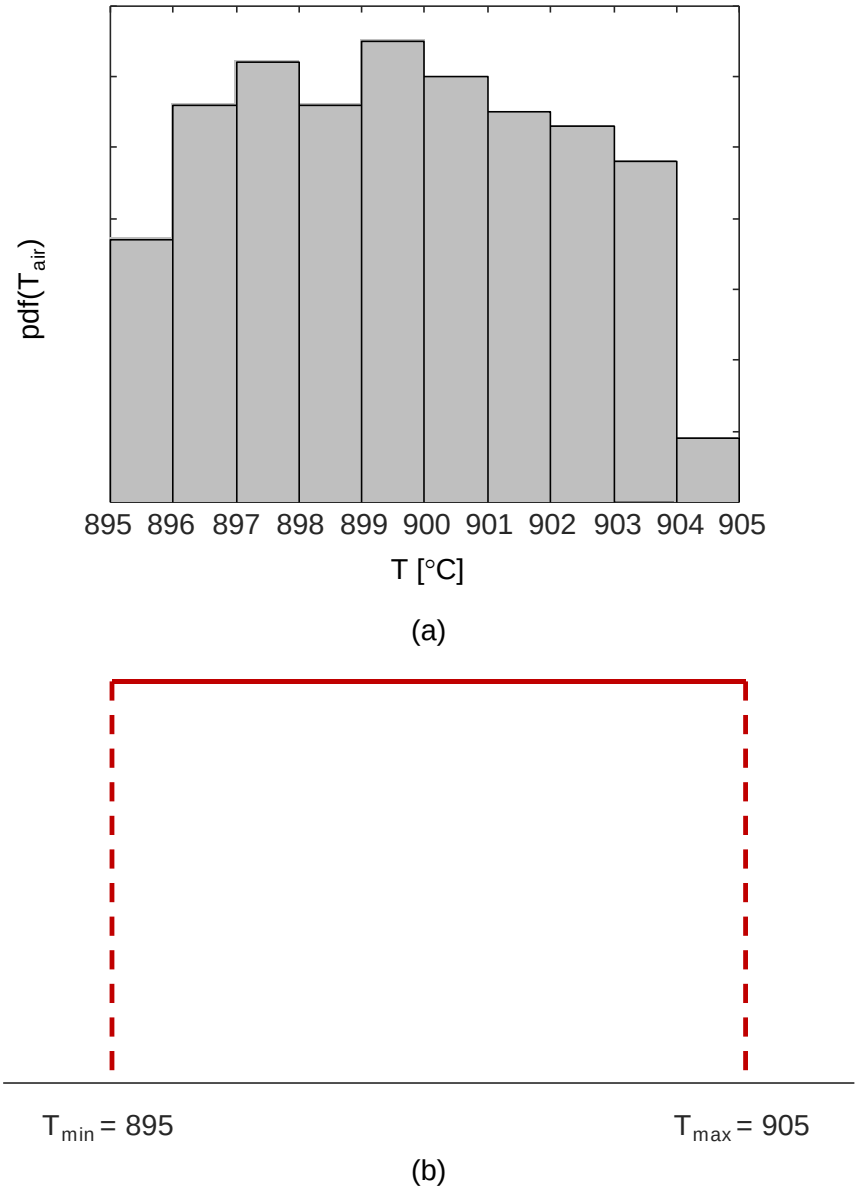

Figure A1.2: (a) Histogram showing the probability density function of the ambient temperature within the muffle furnace. As observed, excluding the very first and last bars, majority of the temperatures have a relatively equal probability of occurring at any instant of time. Thus, a uniform distribution can be used to describe the nature of the temperature variation within the furnaces involved in this study. (b) uniform distribution representing the pdf of the temperature profile.

Figure A1.2 shows that there is relatively an equal probability that all ambient temperature within the furnace can be any of the one depicted by the profile in **Figure A1.1**. It is noted that the temperatures do not have the *exact* same probability due to noise in the measurement data; however, by approximating the profile as being a smooth, continuous, and straight lines each temperature point has an equal chance of occurring.

A.2 First-order Kinetics Model

As mentioned in §3.4.1, each set of dilatometry measurement was used to derive a pair of [E_A, $\log_{10}(A)$] parameters. The parameters representative of the heating rates in roller earth furnaces (1-5°C/s) were binned and found to obey a multivariate normal (MVN) distribution $[E_a, \log_{10}(\mathbf{A})]^T \sim \mathcal{N}(\boldsymbol{\mu}, \boldsymbol{\Gamma})$.

These distribution parameters were then used to derive a 90% confidence interval to account for model uncertainty associated with the parameters, E_A and A, shown in **Figure A2.1**.

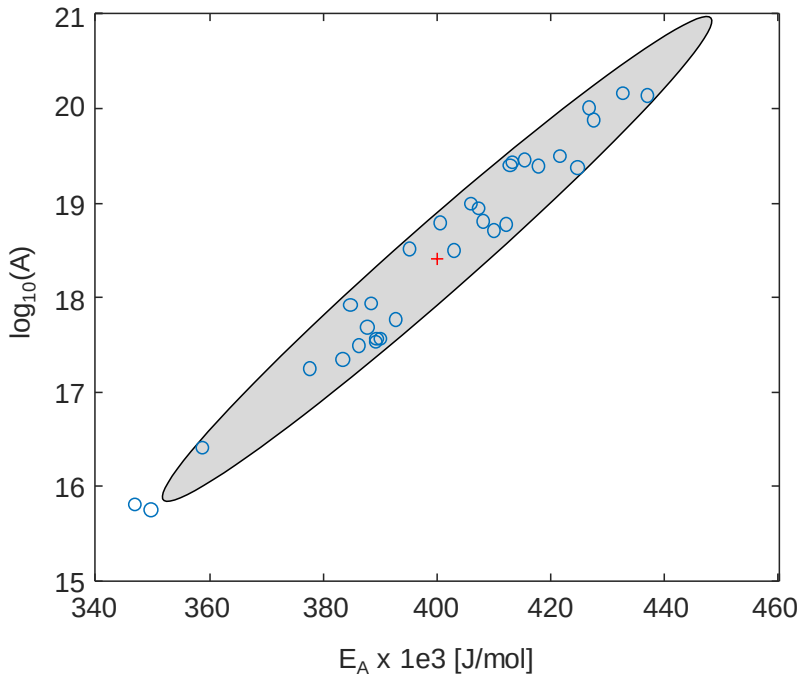

Figure A2.1: Austenitization model parameters derived from Gleeble dilatometry measurements at heating rates between 1 and 5°C/s. Data used to derive 90% confidence ellipse, with mean and covariance shown in Eq. (3.19). Red cross represents mean value of first-order model.

A.3 Monte Carlo Simulation

In order to define the credibility interval a Monte Carlo approach is adopted, where the surrounding and ambient temperatures, and kinetic model parameters are drawn from their respective pdfs. The simulation is run *N* times and the resulting set of blank temperatures and austenite phase fractions are summarized via 95% highest posterior density intervals (HPDI) derived from histograms, as shown in **Figure A3.1**.

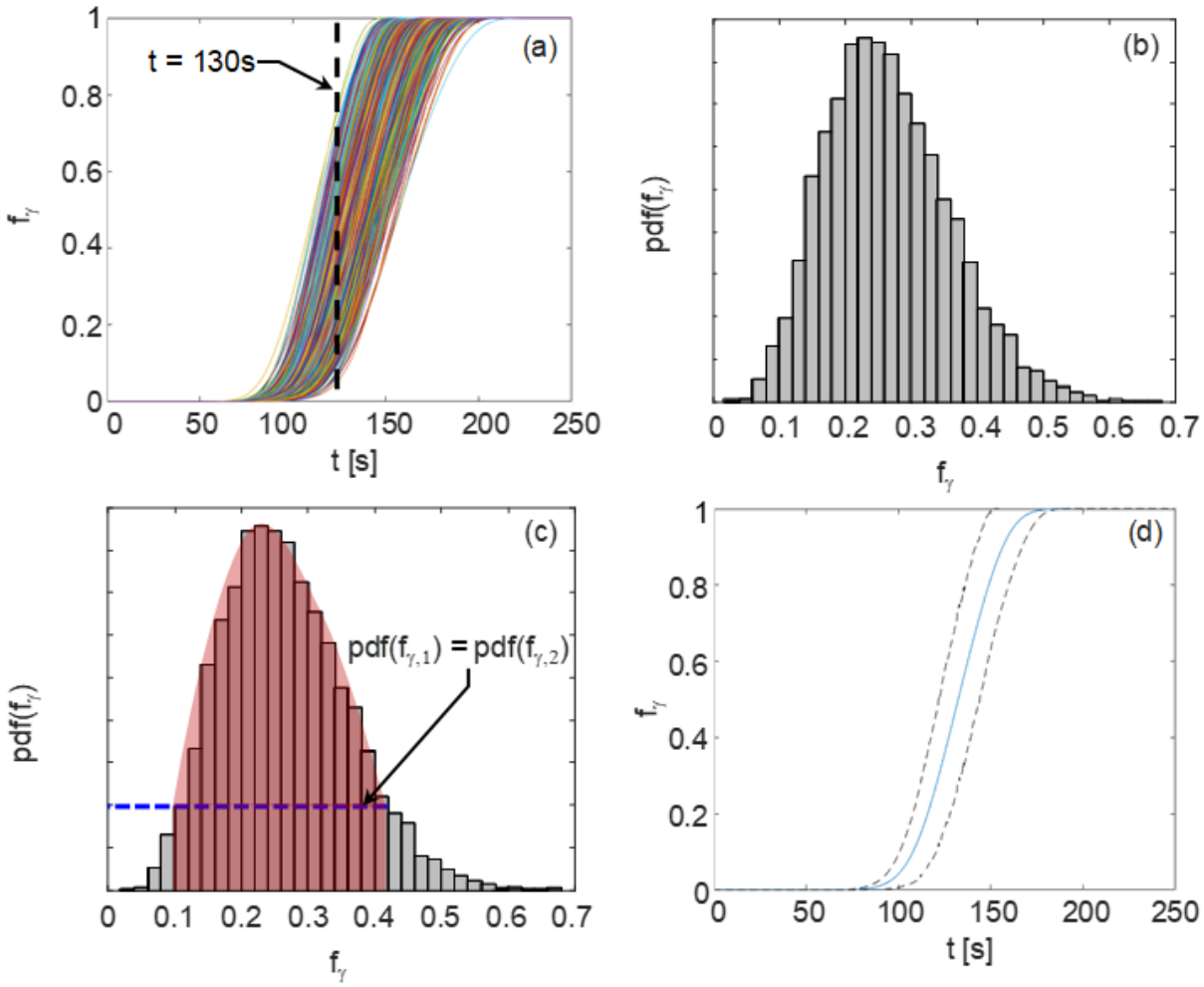

Figure A3.1: (a) Monte Carlo simulation results from *N* number of runs; (b) Histogram for time, t, used for deriving HPDI; (c) Identify points with equal probability, the dark red shaded region should contain the desired credibility level. If the interval contains desired credibility interval, check other regions. Points defining region with desired credibility level with shortest distance are selected to define HPDI; (d) Dashed lines are the credibility interval and solid line is the most probable estimate.

In the case of this study, in order to develop the HPDI from the Monte Carlo simulation a histogram at each time is created as shown in **Figure A3.1(b)**. Next, two points with the same probability density are chosen to define a finite region, shown as dark red in **Figure A3.1(c)**, containing the desired level of credibility (*i.e.* 90%, 99%, or 99.9%). This procedure is repeated until there remain no more points with equal probability densities. The HPDI, shown in **Figure A3.1(d)**, is then defined by identifying which pair of points yields the shortest distance between them.

A.4 Uncertainty in Measured Values

Uncertainty in the sections above focused on the variability associated with model and physical parameters. This section looks at the uncertainty associated with data collected using K-type thermocouples.

A.4.1 Method

The procedure used for the uncertainty analysis is based on the approach defined by Coleman and Steele [97]. The uncertainty in a quantity R is determined by a set of measured values X_j,

$$R = R\left(X_1, X_2, ...X_j\right) \tag{C.1}$$

where each measured value has an uncertainty attached to it denoted by δX_j, and the influence of the uncertainty on R is evaluated by

$$\delta R_{Xj} = \frac{\partial R}{\partial X_j}\delta X_j \tag{C.2}$$

where δR_X represents the uncertainty in R due to the uncertainty in X_j. The uncertainty is thus given by

$$\delta R = \pm\left\{\left(\frac{\partial R}{\partial X_1}\delta X_1\right)^2 + \left(\frac{\partial R}{\partial X_2}\delta X_2\right)^2 + ... + \left(\frac{\partial R}{\partial X_j}\delta X_j\right)^2\right\} \tag{C.3}$$

If R is a function of several measured quantities and the dependence can be expressed as

$$R = X_1^{C1} X_2^{C2} \ldots X_j^{Cj} \tag{C.4}$$

the overall uncertainty is calculated from the uncertainties of each of the individual measurements

$$\frac{\delta R}{R} = \pm \left\{ \left(C_1 \frac{\delta X_1}{X_1} \right)^2 + \left(C_2 \frac{\delta X_2}{X_2} \right)^2 + \ldots + \left(C_j \frac{\delta X_j}{X_j} \right)^2 \right\}^{1/2} \tag{C.5}$$

The overall uncertainty in R is represented as a percentage. The following section describes the uncertainty associated with the temperature measurements.

A.4.2 Temperature Measurements

The out-of-box error tolerance for K-type thermocouples, as per OMEGA™'s Temperature Handbook [98], is the worst case scenario of either ±2.2°C or ±0.75×(Measured temperature). However, this measurement error can be improved if an ice-point cell or cold-junction is utilized. As mentioned in Appendix B, thermocouple measurements using the muffle furnace were done with a National Instruments SCXI-1303 isothermal block, designed with a cold-junction temperature sensor; thus, the measurement error is ±0.9°C [99]. The overall measurement error in the temperature measurements is characterized by

$$\frac{\delta T}{T} = \pm \frac{0.9°C}{T_{meas}\left[°C\right]} \tag{C.6}$$

Figure C5.1 shows the measurement error associated with the actual temperature measurements, using the muffle furnace. Since the standard measurement error is very small, there is high confidence in the thermocouple readings and in the ability of the thermocouples to detect the onset and completion austenitization temperatures. As was observed in Chapter 4, since the simulation results contained the experimental temperature data, the model's predictive capabilities are effective.

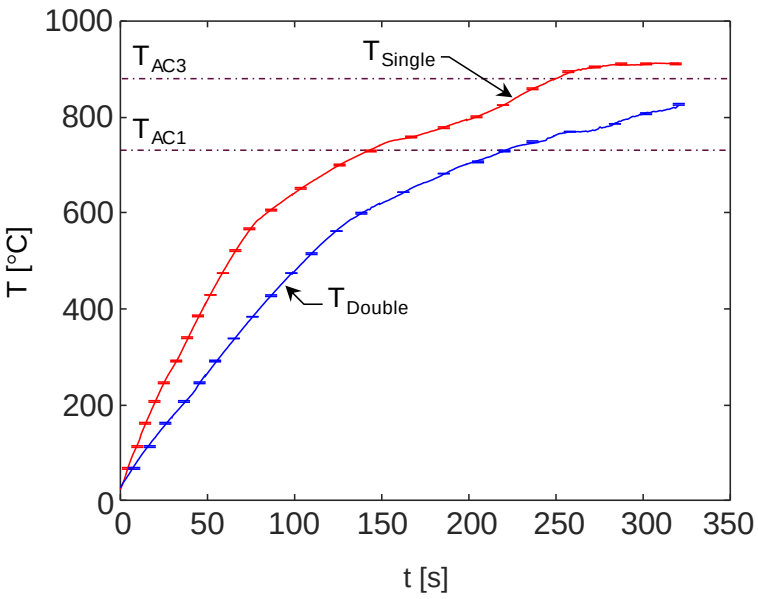

Figure C5.1: Measurement error associated with actual temperature measurements obtained from K-type thermocouples using the National Instruments SCXI-1303 isothermal block, when performing validation studies with muffle furnace.

Appendix B
Experimental Setup

B.1 Muffle Furnace

A laboratory muffle furnace is used for in-house validation studies. Details of the furnace are discussed in Chapter 2. Data logging was performed using a National Instrument SCXI-1000 system with a SCXI-1303 terminal block with 32-channels. The equipment setup is shown in **Figure B1.1**.

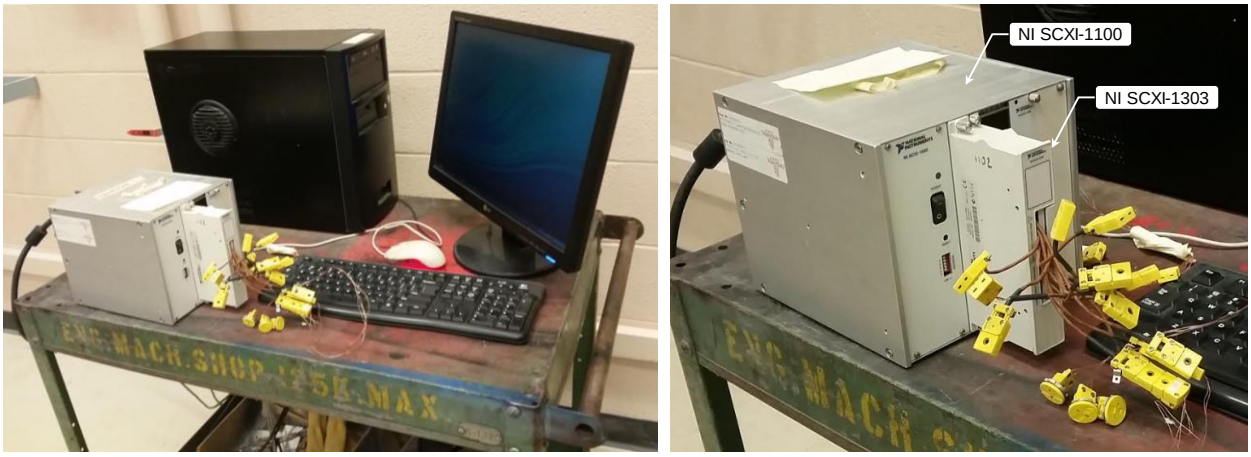

Figure B1.1: Equipment setup used for the laboratory muffle furnace. National Instruments SCXI-1000 chassis used with SCXI-1303 32-channel terminal block for thermocouple connection.

National Instruments LabVIEW software was used to create a program that would record temperature measurements, developed by University of Waterloo personnel. Temperature measurements on instrumented single- and double-gauge coupons were recorded every second.

B.2 Roller Hearth Furnace

Data logging was performed using a hand-held temperature measurement device.

Appendix C
Optimization Using the Phenomenological Kinetics Submodel

The phenomenological kinetics submodel [25], was also used to identify optimal furnace parameters, for a batch consisting of one unpatched blank. The gradient-based interior point method is used to evaluate the constrained multivariate minimization problem. Nominal furnace settings, as defined in **Table 13** (§5.4.1), were used as the initial start point for the algorithm. The algorithm continued to identify new iterates until the KKT conditions were approximately satisfied, as defined in **Table 12**. The optimal solutions and minimized cycle time are summarized in **Table C1**, whereas the optimized heating and austenite curves are shown in **Figure C1**.

Table C1: Optimal solutions and associated cycle time for the optimization problem using Li et al.'s model [25] and nonlinear constraints c_{N13} and c_{N13a}.

	x_1^*	x_2^*	x_3^*	x_4^*	x_5^*	x_6^*	x_7^*	x_8^*	x_9^*	x_{10}^*	x_{11}^*	x_{12}^*	x_{13}^*	x_{14}^*	$F(\mathbf{x}^*)$
c_{N13}	842	843	856	860	879	906	906	908	908	908	906	902	1.767	13.3	13
c_{N13a}	816	826	851	855	880	920	920	929	929	925	920	915	1.749	6.3	28

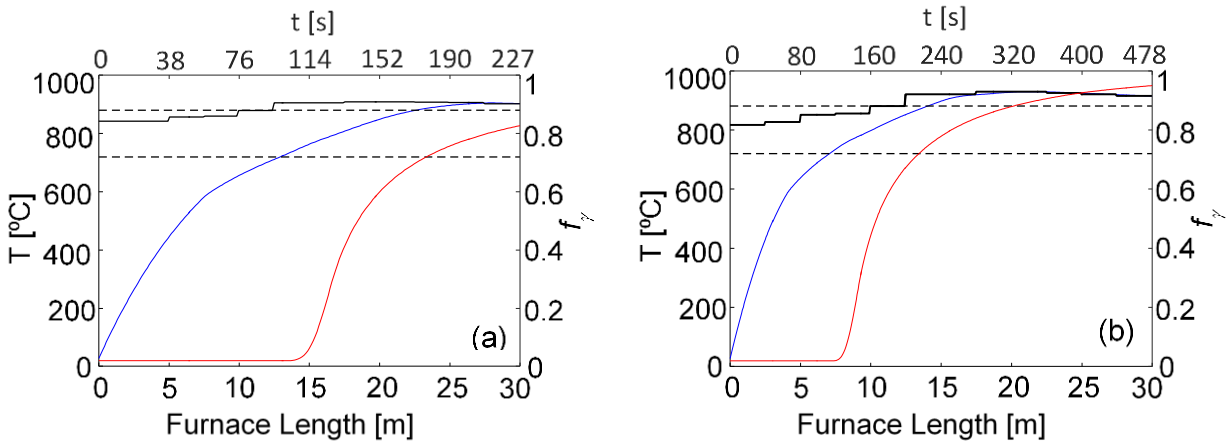

Figure C1: Optimized heating and austenitization profiles. Dashed lines correspond to the austenite start and finish temperatures, T_{Ac1}= 730ºC and T_{Ac3}= 880ºC. Black solid lines are zone temperatures.

The greatest improvement in the cycle time is achieved with the temperature-based constraint, of 16 seconds faster than the nominal solutions. In contrast, only a savings of 1 second is yielded with the explicit austenite constraint imposed. **Figure C1**, shows that although c_{N13} is satisfied, the model predicts incomplete austenitization, approximately 83%, within the batch upon exiting the furnace even though the batch exceeds T_{Ac3}, a consequence of potentially over predicting the influence of impingement. In order to achieve adequate austenitization using the explicit austenite constraint, c_{N13a}, higher zone temperatures, longer residence time, and thus longer cycle times are necessary compared to the former requirement and that predicted using the first-order model [25].

In general, the first five zones have a higher temperature compared to the nominal settings, to allow austenitization earlier within the heating process while avoiding excessive Al-Si layer growth. The soak-based constraint in general shows that all the constraints can be satisfied using lower feasible parameters, similar to the gradient-based method. The alternative constraint, however, suggests zone temperatures identical to the nominal setting are necessary to satisfy the austenitization criteria.

A key difference between the Li et al.'s model [25] and Di Ciano et al.'s model [10] is that the former shows that the growth of austenite is very slow, in particular at higher temperatures. This as mentioned in §4.2.2, may be the consequence of severe model fitting and an over estimation of the impingement effects. The difference in the performance between the two austenitization submodels reflect how influential the choice of austenite constraints and kinetics submodels are when identifying feasible furnace parameters. This observation was also reported by Ganesh et al. [56], who had extended Heng et al.'s [54] optimization model of an austenitizing roller hearth furnace by incorporating a detailed austenite growth model.